Dynamics of the exchanges between the Sermilik fjord and the North Atlantic

Relatore: Presentata da:
Prof. Nadia Pinardi   Elisa Terenghi

Correlatori:
Dott. Francesco Trotta
Prof. Fiamma Straneo

The significance of our lives and our fragile planet
is determined only by our own wisdom and courage.

We are the custodians of life's meaning.

Carl Sagan

Abstract

The Greenland Ice Sheet (GrIS) melting is responsible for one-quarter of the present rate of sea level rise, having the GrIS quadrupled its mass loss from 1992-2001 to 2002-2011 (Chen et al., 2017). This is partly due to the increased surface melt, but also to the retreat, thinning and speed up of the marine-terminating outlet glaciers, a highly non-linear process that is not yet considered in climate prediction models and that is a result of ice-ocean interactions.

The Greenland's marine-terminating glaciers margins are usually located at the head of Greenland's fjords, long, deep and narrow glacial-origin coastal inlets, which constitute the link between the GrIS and the shelf through which Greenland's freshwater reaches the ocean. Therefore, the knowledge of fjord dynamics is essential to understand the processes that have led to the glaciers retreat, to estimate glaciers melt rate and to find out how the discharged freshwater reaches the shelf.

Sermilik fjord, located in south-eastern Greenland, connects the shelf with Helheim glacier, the fifth-largest outlet of the GrIS in terms of total ice discharge. This fjord, as well as the other Greenland's fjords, is characterised by complex dynamics, combining the glacier-driven component with the shelf-driven one.

This thesis aims at describing Sermilik fjord dynamics interactions with shelf dynamics by means of a high resolution nested model, the University of Bologna SURF model, based on the NEMO code and forced by the outputs of a global ocean predictive model developed at CMCC. The adoption of a downscaling technique allows to realistically simulate shelf dynamics and to adequately resolve fjord geometry and bathymetry, since it enables to represent a wide range of scales (from the few hundred meters at the fjord head, to the tens of kms of the Greenland's shelf current system) with a feasible computational cost.

In the first part of the thesis the seasonal fjord circulation is analysed. A seasonally reversing two-layer estuarine and anti-estuarine circulation mode is identified for the first time: it is due to the seasonal changes of the East Greenland Coastal Current strength and variability.

The daily fjord circulation is then investigated, confirming the presence of intense two-layer flows, reversing every few days, associated to pycnocline depth

fluctuations (the so-called intermediary circulation). This circulation mode is proven to be forced by the shelf circulation synoptic temporal variability and at least mesoscale spatial variability.

Analysing advective heat and salt transports from the shelf and correlating them with the properties of the waters adjacent to Helheim glacier, winter intermediary circulation is proven to cause non-negligible fluctuations of these waters temperature and salinity (>1°C and >0.5 PSU), thus probably playing a relevant part in determining glaciers submarine melt rate.

At the end, summer intermediary circulation is compared to winter one and cross-fjord variations of current velocity and water properties are examined.

This thesis opens up to next modelling studies of the downscaling strategies of future climate scenarios to the fjords, with the final aim of forecasting GrIS future contribution to climate change for inclusion in climate models.

Lo sciogliersi della calotta glaciale groenlandese è responsabile di un quarto dell'attuale velocità di aumento del livello del mare, avendo essa quadruplicato la perdita di massa di ghiaccio dal periodo 1992-2001 al periodo 2002-2011 (Chen et al., 2017). Questo è in parte dovuto all'aumento dello scioglimento superficiale, ma anche al ritiro, all'assottigliamento e all'accelerazione dei ghiacciai di sbocco terminanti in mare, un processo altamente non lineare che non è ancora incluso nei modelli di previsione del clima e che è conseguenza delle interazioni fra il ghiaccio e l'acqua marina.

Il termine dei ghiacciai groenlandesi che raggiungono il mare è generalmente collocato alla testa dei fiordi, insenature costiere lunghe, strette e profonde di origine glaciale, che costituiscono il collegamento fra la piattaforma continentale e la calotta groenlandese: attraverso i fiordi l'acqua dolce proveniente dalla calotta raggiunge l'oceano. Di conseguenza, la conoscenza della dinamica dei fiordi è essenziale per comprendere i processi che hanno portato al ritiro dei ghiacciai, per stimare la velocità di scioglimento degli stessi e per capire come l'acqua dolce prodotta raggiunge il mare di piattaforma.

Il fiordo Sermilik, nel sud-est della Groenlandia, collega l'oceano costiero con il ghiacciaio Helheim, il quinto più grande sbocco della calotta groenlandese in termini di quantità totale di ghiaccio rilasciato. Questo fiordo, così come gli altri fiordi groenlandesi, è caratterizzato da una dinamica complessa, principalmente risultante dalla combinazione della componente forzata dai ghiacciai e di quella forzata invece dalla circolazione sulla piattaforma continentale.

Questa tesi ha l'obiettivo di descrivere le interazioni tra la dinamica del fiordo Sermilik e la dinamica della regione di piattaforma, grazie all'utilizzo di un modello nestato ad alta risoluzione: SURF, sviluppato dall'Università di Bologna, basato sul codice NEMO e forzato dai risultati di un modello oceanico globale di previsione sviluppato dal CMCC. L'adozione della tecnica di downscaling permette di simulare realisticamente la dinamica della piattaforma e di risolvere in modo adeguato la batimetria e la geometria del fiordo, dal momento che consente di rappresentare un ampio intervallo di scale spaziali (dalle poche centinaia di metri alla testa del fiordo alle decine di chilometri del sistema di correnti sulla piattaforma continentale groenlandese) mantenendo costi computazionali ridotti.

Nella prima parte della tesi viene analizzata la circolazione nel fiordo a scala stagionale. Viene identificato per la prima volta un modo di circolazione estu-

arino e anti-estuarino a due strati che si riversa stagionalmente: questo pattern è dovuto ai cambiamenti stagionali dell'intensità e della variabilità della corrente costiera della Groenlandia orientale.

Viene poi studiata la circolazione nel fiordo a scala giornaliera, confermando la presenza di intensi flussi a due strati, associati a fluttuazioni della profondità del picnoclino, che cambiano la propria direzione a intervalli di pochi giorni (si parla di circolazione intermediaria). Questo modo di circolazione è provato essere dovuto alla variabilità temporale a scala sinottica e alla variabilità spaziale alla mesoscala (almeno) della circolazione sulla piattaforma.

Esaminando i trasporti avvettivi di calore e sale dalla piattaforma e correlandoli con le proprietà delle acque adiacenti al ghiacciaio Helheim, viene provato che, in inverno, la circolazione intermediaria causa fluttuazioni non trascurabili nella temperatura e salinità di queste acque (>1°C e >0.5 PSU). Questo modo di circolazione interpreta quindi, probabilmente, una parte rilevante nel determinare la velocità di scioglimento sottomarino dei ghiacciai.

Infine, la circolazione intermediaria estiva è confrontata con quella invernale e vengono esaminate le variazioni della velocità delle correnti e delle proprietà dell'acqua in direzione trasversale al fiordo.

Questa tesi apre a successivi studi sulle strategie di downscaling di scenari climatici futuri nei fiordi, con l'obiettivo finale di prevedere il contributo futuro della calotta glaciale groenlandese al cambiamento climatico e di includere tale contributo nei modelli climatici.

Contents

Introduction

Contents

1.1   Definition and formation of fjords

The term Fjord, from the old Norse *Fjorthr*, has been applied to all the geological structures developed by glacial erosion and partly filled with seawater; they can therefore be defined as glacial-origin semi-enclosed coastal inlets (Farmer et al., 1983).

We can identify fjords from the following characteristics:

- they are usually long relative to their width;
- they are steep sided and deep, often deeper than the adjacent continental shelf;
- they typically possess one or more submarine sills which define one or more deep basins of the fjord and which may be remnant moraines;
- there is usually a river or a glacier, which is typical of Greenland's fjords, discharging into the head.

The term head is used to decribe the inland termination of the fjord; the mouth is its seaward opening (Farmer et al., 1983). Fjords with marine-terminating glaciers at their heads are called glacial fjords (Straneo et al., 2015).
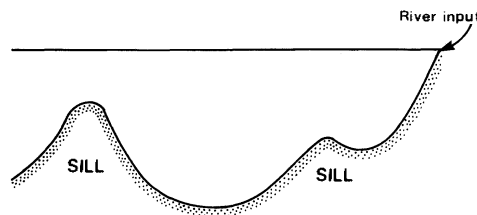
Figure 1.1: Fjord typical structure. Figure modified from Farmer et al. (1983).

A fjord is formed when a glacier cuts a U-shaped valley by ice segregation[1] and abrasion[2] of the surrounding bedrock (Murton et al., 2006). Glaciers developed in pre-glacial valleys with a gently sloping valley floor, that were afterwards overdeepened by the work of the glaciers themselves (see figure 1.2). Such valleys are fjords when flooded by the ocean (Aarseth et al., 2014). Thresholds at the mouths and overdeepening of fjords compared to the ocean are the strongest evidence of glacial origin (Nesje et al., 1994).

---

[1]Ice segregation indicates erosion produced when moisture, diffused within soil or rock, accumulates in a localized zone. The ice initially intrudes in small pores or pre-existing cracks, and, as long as the conditions remain favourable, it continues to accumulate wedging the soil or rock apart.

[2]Abrasion is a process of erosion which occurs when material being transported wears away at a surface over time. Glaciation slowly grinds rocks picked up by ice against rock surfaces.
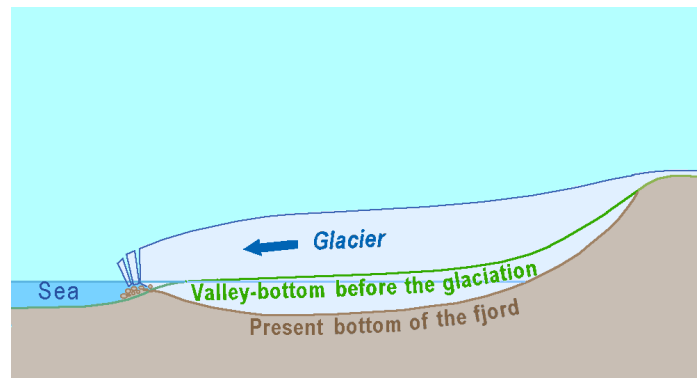
Figure 1.2: Fjord formation scheme. Reproduced from Ulamm.

1.2 Why we study Greenland's fjords

1.2.1 Climate

1.2.1.1 How Greenland's fjords affect climate

Sea level rise   Mass loss from the Greenland Ice Sheet (GrIS, covering three quarters of Greenland in ice up to 3 kilometres thick, ICESat) quadrupled from 1992-2001 (51 ± 65 $Gt\ yr^{-1}$) to 2002-2011 (211 ± 37 $Gt\ yr^{-1}$) (Van den Broeke et al., 2009; Shepherd et al., 2012; Enderlin et al., 2014). This loss contributed to a rise in global mean sea level of 7.5 ± 1.8 mm from 1992 to 2011, making Greenland alone responsible for one-quarter of the present rate of sea level rise (Church et al., 2011; Chen et al., 2017).

This is due not only to increased surface melt in southeast and west Greenland (Hanna et al., 2011; Van den Broeke et al., 2009), but also to the direct link existing between the Greenland Ice Sheet and the ocean: the glaciers margins located at fjords heads. There has been a widespread retreat, thinning and speed up of marine-terminating glaciers in southeast and west Greenland, since the mid-1990s (Rignot et al., 2006; Howat et al., 2007) (figures 1.3 and 1.4), and in northwest Greenland, since the mid-2000s (Khan et al., 2010). This has not happened to glaciers terminating on land (Sole et al., 2008) and, therefore, is directly ascribable to ice-ocean interactions. This process, that could be named *dynamic thinning*, is highly nonlinear and poorly understood. As a consequence, it is absent from climate models.

The actual forecast of eustatic[3] sea level rise until 2100 caused by Greenland's

---

[3]The sea level change is defined eustatic when is given by variations in the masses or volume of the oceans; it's called relative when it is due to changes of the land with respect to the sea surface.

ice melting is 0.01 m to 0.54 m. The huge uncertainty of this prediction must be primarily ascribed to the absence of sufficient knowledge of the ice-sea interaction processes, but also of ice dynamics and physics (Straneo et al., 2013), highlighting the importance of further scientific research to be carried out. Moreover, the variable that has an actual and direct impact on society and coastal communities is not the already highly uncertain value given before, but, instead, is the regional sea level, which can be up to five times greater than the above mentioned global mean (Gelderloos et al., 2011).
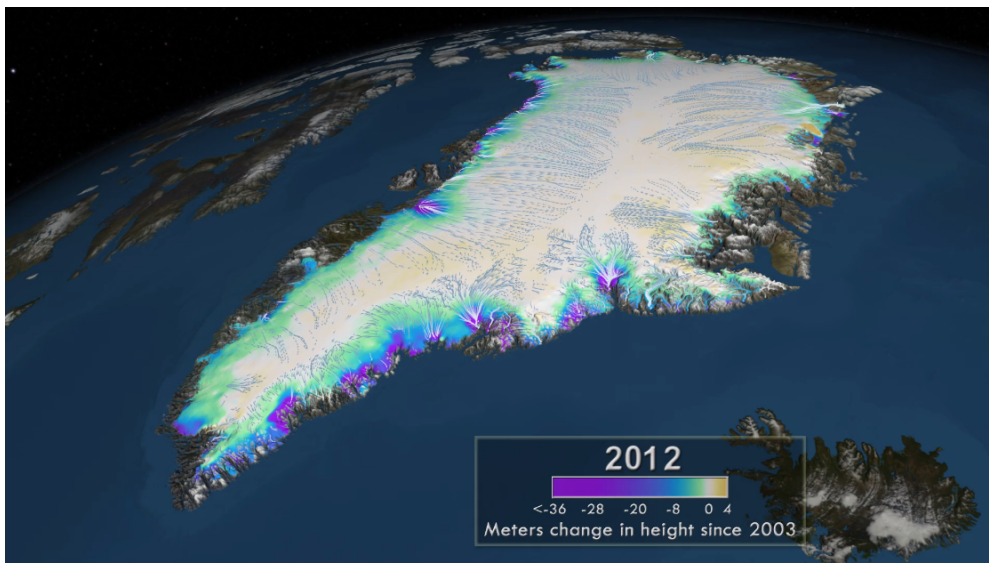
Figure 1.3: Accumulated change in the surface elevation of the Greenland Ice Sheet between 2003 and 2012; the blue/white flows indicate the direction and speed of the ice movement: slower moving ice is shown as shorter blue flow lines, while faster is shown as longer white flow lines. Reproduced from ICESat.

Export of freshwater   Even if Greenland's freshwater discharge has been conventionally considered negligible with respect to the freshwater export from the Arctic Ocean (Straneo et al., 2013), Greenland's cumulative freshwater anomaly released since 1995 amounts to a third of Arctic-origin freshwater anomalies that have disrupted dense water (North Atlantic Deep Water) formation in the Labrador sea in the past (Bamber et al., 2012). North Atlantic Deep Water formation is essential to maintain the Atlantic Meridional Overturning Circulation (AMOC). Thus, the GrIS discharge has a remarkable impact on the freshwater budget of the North Atlantic, and, if it persists, it is likely to have consequences on both the regional ocean (including the marine ecosystem) and the global ocean (through the AMOC) (Straneo et al., 2015).
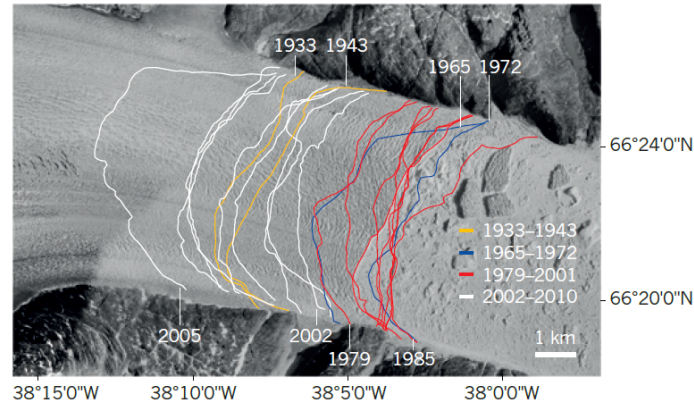
Figure 1.4: Helheim glacier retreat (Sermilik fjord, south-east Greenland). Reproduced from Straneo et al. (2013).

Modification of exported water   The freshwater flux from the GrIS is not distributed evenly around Greenland but, instead, is localized into a discrete number of points, corresponding to the major glacial fjords: fjords are the conduits through which GrIS freshwater reaches Greenland's continental shelves (see section 1.4). Thus, the freshwater discharged from Greenland is subject to fjord processes and dynamics before reaching the shelf: fjord processes can transform (e.g. by mixing) or delay (e.g. by storing) the glacier freshwater input. For example, given the high seasonality of the freshwater flux (due to the strong melting seasonality), fjord processes may delay this export by weeks or longer depending on the magnitude of the fjord circulation (Straneo et al., 2015).

Knowledge of the fjords dynamics and processes is therefore unavoidable to estimate glacier melt rates, understand by what and to what extent they are controlled and to find out where and when freshwater enters the ocean. This knowledge is necessary for determining appropriate boundary conditions for large-scale ocean and climate models (Straneo et al., 2015).

1.2.1.2   How climate affects Greenland's fjords

The increased surface melt (see section 1.2.1.1) is due to changes in precipitation and rising air temperatures (Box et al., 2009; Hanna et al., 2013; Hall et al., 2013).

The glaciers retreat (see section 1.2.1.1), especially the increase in submarine melting of the glaciers, is due to a rapid warming of the subpolar North Atlantic (SPNA) ocean and atmosphere (Straneo et al., 2013).

SPNA ocean warming began in the mid-1990s (Yashayaev, 2007; Bersch et

al., 2007) and continues today (Williams et al., 2013). It consists of a warm-
ing of the upper 500-1000 m of the waters off west Greenland, including the
continental shelf (Holland D. M. et al., 2008; Myers et al., 2013, 2007). More-
over, a simultaneous warming of the upper 1000-2000 m of the subpolar and
subtropical North Atlantic started in the late 1990s resulting in a large heat
content anomaly over the entire North Atlantic (Straneo et al., 2013). The
fjords response to shelf warming should be within few months, given the rapid
renewal times of fjord water (see sections 1.5.5 and 1.5.6): the ice-terminating
glaciers have been quickly exposed to these changes.

Warming of the SPNA is unprecedented in the historical record, except for a
similar warm period in the 1930s. Reconstructions from e.g. sediment cores
or photographs (satellite radar observations became available only from 1991)
suggest that during the twentieth century Greenland's glaciers retreated as
much as today only in the 1930s (see figure 1.4), concurrently with the SPNA
warming (Straneo et al., 2013).

The SPNA ocean warming is attributed to the anomalous inflow of warm, salty,
subtropical Atlantic water into the subpolar region (Hatun et al., 2005) driven
by shifting wind patterns over the North Atlantic (Hakkinen et al., 2004, 2011).
These are strongly correlated with winter episodes of atmospheric blocking over
Greenland (Hakkinen et al., 2011; Woollings et al., 2008) caused by large and
quasi-stationary waves in the jet stream. The increase in Atlantic water on the
shelves has probably led to a warmer and thicker layer of Atlantic water in the
fjords, both of which increase submarine melt rates (Sciascia et al., 2013).

From a climatological point of view the SPNA warming has been convention-
ally connected to the switching of the North Atlantic Oscillation[4] (NAO) from
a persistent positive phase in the early 1990s to a negative or quasi-neutral
phase until the mid-2000s. A negative NAO phase leads to a warming of the
subpolar, as observed, and a cooling of the subtropical area of the North At-
lantic. However, recent statistical analyses reveal that much of the wind stress,
SPNA heat content and sea-surface height anomalies cannot be attributed to
the NAO (Hakkinen et al., 2011; Lohmann et al., 2009). The subtropical ocean
has been accumulating heat (Levitus et al., 2012), partly as a consequence of
atmospheric warming (Williams et al., 2013), but some of this heat was trans-
ported into the subpolar region only when the NAO left its positive phase.

On multidecadal timescales, the warming of the SPNA is strongly correlated

---

[4]Leading pattern of atmospheric variability consisting in atmospheric pressure oscillations
on the Northern hemisphere Atlantic ocean. It's defined by the sea-level pressure difference
between weather stations in the Azores and Iceland.

with the Atlantic multidecadal oscillation[5] (AMO), even after the subtraction of the global rise in SST (Hakkinen et al., 2013; Polyakov et al., 2005).

In conclusion, the most probable causes of the SPNA ocean warming are the persistence of wind patterns driving subtropical waters into the subpolar region and the superposition of single modes of multidecadal natural atmospheric or oceanic variability on a long-term North Atlantic ocean warming trend (Levitus et al., 2012; Straneo et al., 2013).

Regarding the SPNA atmosphere warming, growing air temperatures lead to enhanced surface melting which increases subglacial discharge (see section 1.4). This, in turn, boosts submarine melting (see again section 1.4), augmenting glacier retreat. This is particularly worrying considering the evidence for polar amplification (the above-global average increase in Arctic near-surface temperatures) (Manabe et al., 1980; Chylek et al., 2009), which will further increment surface melting and extend summer melt season.

1.2.2 Other reasons to study fjords

Fjords are extremely important in biology for their complex ecosystems, including cold-water coral reefs, living at depth in the dark, discovered in Norwegian, New Zealand's and Chilean fjords, responsible for the huge fishing resources of the Norwegian coastline (Freiwald et al., 2004).

Moreover, fjords contain records of past ice sheet and glacier variability (Andresen et al., 2012).

One of the most important characteristics of fjords concerns carbon sequestration: while fjords account for less than 0.1% of the surface of Earth's oceans, they account for 11% of global marine organic carbon burial[6]. Per unit area, fjord organic carbon burial rates are one hundred times the global ocean average and at least five times the other marine systems rates; fjord sediments contain twice as much organic carbon as biogenous sediments underlying the ocean upwelling regions. This is partly because of the high rates of organic material fluxes they receive thanks to the convergence of surface water. The most efficient fjords, regarding carbon burial, are Alaskan fjords.

---

[5] Mode of oceanic variability defined by the sea-surface temperature (SST) anomaly over the North Atlantic (Schlesinger et al., 1994; Enfield et al., 2001). It is associated with AMOC variability, shifts in hurricane activity (Ting et al., 2009) and other climate processes.

[6] Organic carbon burial in marine sediments is a slow process involving the accumulation of sinking organic and mineral particles. Before being permanently buried, organic carbon is degraded by benthic macrofauna and microorganisms. The majority of the organic matter is remineralized back to inorganic carbon and then buried a metre or more below the sea floor, beneath the zone of active degradation (Keil, 2015).

Fjords may thus be fundamental in climate regulation on glacial-interglacial timescales, since marine carbon burial represents the dominant natural mechanism of long-term organic carbon sequestration[7], having therefore played an important role in regulating atmospheric O_2 and CO_2 concentrations over the past 500 million years (Smith et al., 2015).

1.3   Greenland's continental shelf dynamics
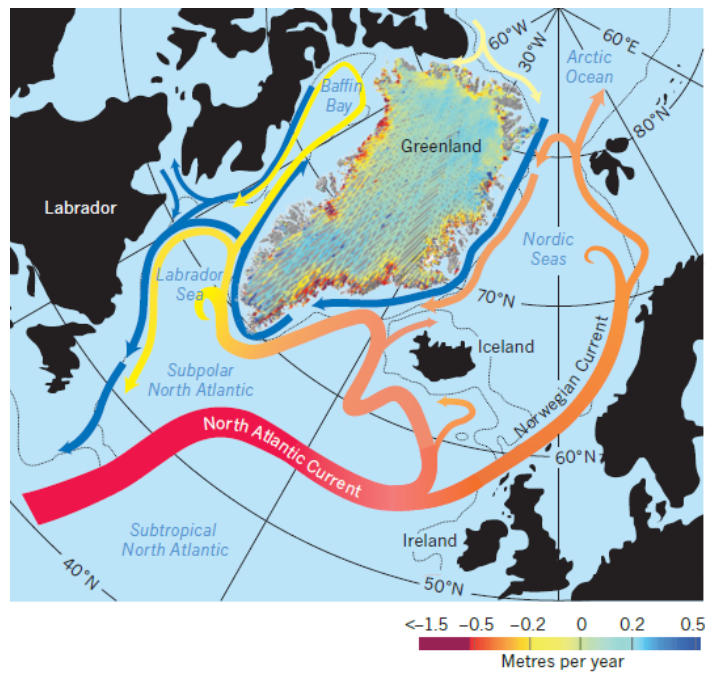
Figure 1.5: Large-scale ocean circulation around Greenland; colder currents are represented in blue, while warmer in red. The dynamic thinning of the GrIS is superimposed (Pritchard et al., 2009). Reproduced from Straneo et al. (2013)

Properties of the water inside fjords resemble those of the water on the nearby continental shelves, consistently with the fjords deep sills, that allow the exchanges with the shelves (see section 1.4). Polar Water (PW), cold, relatively fresh water of Arctic origin, carried by the East and West Greenland Currents (in blue in figure 1.5; Myers et al. (2007); Sutherland et al. (2008)), overlies Atlantic Water (AW), warm (0-4℃, while the freezing point of seawater is approximately -1.9℃), salty water of Atlantic origin (Holland D. M. et al., 2008; Rignot et al., 2010; Straneo et al., 2010; Christoffersen et al., 2011) (figure 1.6). Warm AW is found also near the glaciers at the fjords head (Straneo et

---

[7]Carbon removal from the active cycle.

al., 2012).

The average AW and PW properties on the shelf and slope, as well as in the fjords, vary according to the distance from their source regions along their mean pathways. For example, AW found in fjords abutting the Artic ocean (e.g. near Petermann Glacier) is colder than that found in fjords abutting the SPNA (e.g. near Helheim Glacier). Also the amplitude of the interannual and decadal temperature variations scales with distance from the source (Straneo et al., 2012).

The circulation around the SPNA is constituted by a cyclonic gyre with warm waters from the subtropics flowing around the continental slopes of Greenland and North America (Yashayaev, 2007; Vage, 2011). The Arctic water, instead, flows around the Greenland's 200-300 m deep continental shelves, partially sheltering Greenland's coast from AW (see figures 1.5 and 1.6) (Sutherland et al., 2008; Straneo et al., 2013).

AW in fjords is colder than that circulating offshore: it must be transformed while crossing the shelf (Straneo et al., 2012).

1.4 Characteristics of Greenlandic fjords and glaciers
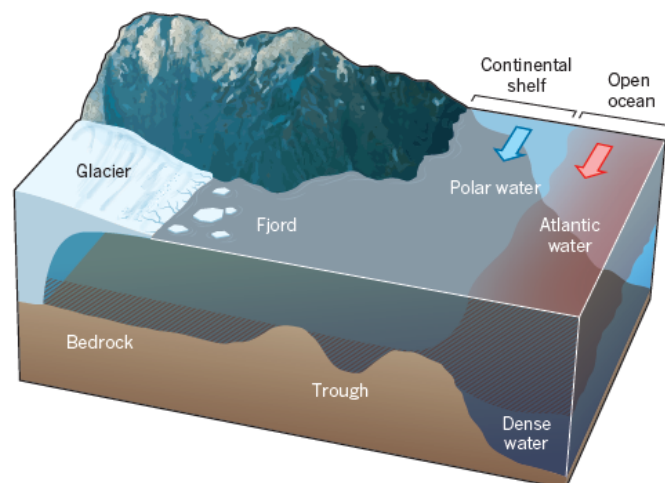
Figure 1.6: Polar water flows close to the coast, while Atlantic waters, circulating around the SPNA, reach Greenland's glacial fjords at depth after crossing the continental shelf. Reproduced from Straneo et al. (2013).

Greenland's fjords show several characteristics that distinguish them from other fjords, leading also to the partial inapplicability of existing fjord teories:

- Greenland's large fjords have deep (>200 m) sills, easily permitting water

exchange with the shelf. On the contrary, usually, fjords sills are way shallower, often inducing extreme tidal currents.

- As seen in section 1.3, Greenland's continental shelves show the presence of two distinct water masses, PW and AW, that, thanks to the deep sills, both enter the fjords, resulting in a strongly stratified water column before the additional freshwater is discharged into the fjord (figure 1.6). This opposes the assumption made by most fjord theories that a single water mass reaches the fjord from the shelf.

- Greenland's marine-terminating glaciers are usually grounded several hundreds of meters below sea level: the large amount of seasonal surface melt released from the GrIS, through a complex network of moulins and channels in the ice, the glacier hydrologic network (Das et al., 2008; Chu et al., 2009), is released at huge depth at the bases of glaciers (the grounding line depth) (Chu V. W., 2014). The freshwater that is released in Greenland's fjords in this way constitutes the subglacial discharge or runoff. It reaches the fjords either through several discrete channels or as a distributed source at the base of the glacier (Straneo et al., 2015).
  This is different from what happens in Antarctica, where surface melt is limited and the glaciers are grounded closer to the surface, or in typical estuaries, where again freshwater enters at the surface.

Greenlands's marine-terminating glaciers can fundamentally be divided into two different classes: some have mostly vertical glacier fronts and flow very fast (e.g. Jakobshavn Isbræ glacier, west Greenland's coast, which can move at 17 km/y, Joughin et al. (2014)), others have 50-100 km long floating ice tongues and flow at much slower speeds (e.g. 1 km/y for Petermann glacier, Munchow et al. (2014)). For the first category, the mass balance is controlled mainly by calving[8]. The fjords associated with these glaciers are typically clustered with icebergs and have a densely packed ice mélange[9] near the glacier (see figure 1.11, Amundson et al. (2010)). They are usually found in south-western and south-eastern Greenland, like, for example, Helheim, Kangerdlugssuaq and Jakobshavn Isbræ glaciers. Regarding the second type, submarine melting under the long floating ice tongue primarily controls the mass balance. This type of glaciers, like Petermann glacier, is typical of northern Greenland.

The presence of the ice mélange or the long ice tongue makes the near-terminus region almost inaccessible by boats. In addition, icebergs that travel

---

[8]The periodic breakoff of icebergs (Straneo et al., 2015).

[9]Dense mixture of sea ice (originated from the freezing of seawater) and icebergs (from glacier calving) that may influence glacier flow (see section 1.6.2).

along the fjords are particularly dangerous for ships and often preclude the possibility of moored observations. Near the quasi-vertical glaciers, calving and the ice mélange cause the region without data to extend 5-10 km from the terminus, while the long ice tongue prevents measurements up to its end, otherwise it would be necessary to drill through hundreds of meters thick ice (Straneo et al., 2012). Measurements in Greenland's fjords are then rare and sparse, a fact that appears to be especially negative when the need for densely packed and long term data, necessary to have the right comprehension of melting rates variability, is taken into account.

Field measurements of heat and salt fluxes have been used to estimate submarine melt rate by Inall et al. (2014); Rignot et al. (2010) and Sutherland and Straneo (2012), obtaining values in the range of $80 - 800 \ \frac{m^3}{s}$ for different fjords. However, these results are highly uncertain since they are derived from sparse observations, which are taken, for the reasons cited above, far from the glacier terminus, and not taking into account all the possible contributors to the heat balance, as, e.g., melting of the ice mélange and icebergs (see section 1.4.1), storage terms or barotropic transports (Jackson et al., 2016; Cowton et al., 2015). Considering all these contributors, Jackson et al. (2016) found an estimate of submarine melting in August for Sermilik fjord (south-eastern Greenland), comprising iceberg meltwater, greater than those of the previous studies: $1500 \pm 500 \ \frac{m^3}{s}$.

Along with observations, submarine melt rates could be inferred also using numerical models that include a termodynamical parametrisation of melting, taking into account e.g. glacial characteristics, ocean forcing and turbolence. Studies of this type (Jenkins, 2011; Sciascia et al., 2013; Xu et al., 2013) have suggested that submarine melt rate increases linearly with increasing water temperature and with a power of 1/3 with increasing subglacial discharge, thanks to higher melt rates where the rising runoff-driven plumes (see section 1.5.2) are in contact with the ice front.

However, quantitative models results are still particularly uncertain regarding the magnitude and the spatial and temporal variability of the submarine melt rates, since they are highly sensitive to the parametrisations employed. The ice-ocean boundary layer parametrisations (plumes dynamics and turbulent coefficients, see section 1.5.1), for example, have not been validated by measurements yet.

Moreover, estimating external forcings as subglacial discharge is particularly challenging (Straneo et al., 2015), especially with regard to subglacial runoff spatial distribution, i.e. the geometrical characteristics of the glacier hydrolog-

ical network. A better constraint of these characteristics would be extremely important since, for example, several small channels would result in weaker plumes than few large channels but also in a greater portion of the ice front in contact with the plumes, increasing the spatially averaged runoff-driven submarine melting (given the sub-linear relationship between submarine melting and subglacial runoff). At the same time the distribution of submarine melting (concentrated around a large channel or more smoothly distributed) may influence the way the ice could break and thus the calving rate of the front (Cowton et al., 2015).

To sum up, freshwater can enter a glacial fjord in different ways:

- subglacial discharge, also called subglacial runoff (see third point of the previous list);
- discharge of solid freshwater through calving icebergs and following icebergs melting and icebergs submarine melting;
- submarine melting at ice-ocean interface;
- sea ice melt;
- surface runoff;
- precipitation.

Water originating from submarine glacier, icebergs and sea ice melting enters at seawater freezing point and requires latent heat from the ocean to be melted. Water from surface or subglacial runoff, instead, reaches the fjord approximately at freshwater freezing point and does not require latent heat from the ocean (Jackson et al., 2016).
The GrIS total freshwater discharge, including icebergs, submarine melting and runoff of ice melting above sea level (not precipitation or rainfall runoff), estimated through ice flux derivation from remote sensing products and climate models results for runoff, was stable from 1961 to 1990 ($0.029 \pm 0.002 \ Sv$) (Bamber et al., 2012), but then it has been increasing to $0.041 \pm 0.002 \ Sv$ in 2012 (Enderlin et al., 2014).

1.4.1 Icebergs

According to Jackson et al. (2016), at least 30% of the total ice flux from the glaciers melts within the fjords, either at the terminus of the glaciers or from icebergs, whose melt rate within the fjords depends on the their residence time. This may vary from fjord to fjord (Straneo et al., 2015). The remaining

portion of the ice discharge leaves the fjord in the form of icebergs that don't completely melt in it.

Iceberg melting is likely a major heat sink and significant source of submarine meltwater in fjords with rapidly calving glaciers. Enderlin and Hamilton (2014) estimated the submarine melt rate of icebergs in Sermilik Fjord to be approximately 140 m/y, suggesting that, given the large number of huge icebergs present, they might contribute $O(100)$ $\frac{m^3}{s}$ or more to this fjord meltwater. This implies that the iceberg melt term is likely a major term in the fjord heat budget and total meltwater flux (Straneo et al., 2015). Icebergs contribution to meltwater hardens the effort to infer glacier only submarine melt rates from oceanic measurements. It should be necessary to distinguish the two different sources and, for example, icebergs presence makes the freshwater flux obtained from ocean measurements dependent on the distance from the glacier at which these measurements are taken (Jackson et al., 2016). Hence, further studies are necessary to assess icebergs contribution to freshwater and heat budgets.

1.5 Dynamics of Greenlandic fjords

Regarding the dynamics, fjords can be divided into three parts:

1. the ice-ocean boundary layer, a few meters thick;

2. the plume layer, a few tens of meters thick;

3. the 50-100 km long large fjord system.

The ice-ocean boundary layer, together with the plume layer, forms the near-ice zone, whose processes regulate the heat and mass exchange across the ice-ocean interface, including phase changes.
The large fjord dynamics, instead, control the supply of warm water to the vicinity of the glacier and the export of freshwater from the fjord to the continental shelf. They are governed by buoyancy forcing from the glacier and icebergs (see section 1.5.4), exchanges with the continental shelf (1.5.5), surface fluxes, local winds (1.6.2) and tides (Straneo et al., 2015). We will not focus on tides since for our case of study, Sermilik fjord, tides influence is scarce (tidal velocities are of order 10^{-3} $\frac{m}{s}$ inside the fjord; Jackson et al. (2016); Sutherland et al. (2014)).

1.5.1   Ice-ocean boundary layer

The ice-ocean boundary layer consists of a few meters thick turbulent region, where the turbulence is unaffected by the boundary, and a viscous sublayer (a few millimeters from the ice) where turbulent eddies are suppressed by the presence of the boundary and molecular processes dominate the exchanges (Holland et al., 1999; Jenkins et al., 2010).

The interaction between the ice and the fjord water at this boundary determines the heat and freshwater fluxes associated with phase changes at the interface. A correct representation of these fluxes is fundamental for a reliable estimate of the glacier melt rate (Straneo et al., 2015).

The melt rate is usually parametrised using a three equations model, one for the freezing temperature of sea water, depending on depth and salinity, and the other two equations for heat and salt conservation. The heat supplied to the glacier by the fjord water must be balanced by the latent heat necessary for melting and the heat necessary for increasing ice temperature to melting point.

The heat and salt fluxes supplied to the glacier by the fjord water are usually parametrised respectively as $Q_a^T = c_P \rho_a \gamma_T (T_a - T_b)$ and $Q_a^S = \rho_a \gamma_S (S_a - S_b)$, where T_a, S_a and ρ_a are the ambient water temperature, salinity and density, S_b and T_b the ice interface salinity and temperature, c_P the seawater specific heat, γ_S and γ_T the salinity and thermal exchange velocities, also called turbulent transfer coefficients, which take into account the nonlinear profiles of temperature and salinity in the boundary layer resulting from turbulence. As a consequence, the melt rate strongly depends on γ_T and γ_S, making their derivation a topic issue for melt rates estimation, especially given the following problems.

The thermal exchange velocities are generally expressed as

$$\gamma_{T,S} = C_D^{1/2} \Gamma_{T,S} U_a \tag{1.1}$$

where U_a is the ambient water velocity and $C_D^{1/2} \Gamma_{T,S}$ are the thermal and haline Stanton numbers (C_D is the drug coefficient).

For Greenland's vertical glacier fronts, U_a is mostly the velocity of buoyant plumes (see section 1.5.2), which, in a model, is a strong function of the numerical resolution: coarser resolutions result in slower plumes. This dependence on resolution should be taken into account. Furthermore, the plumes properties (and thus U_a) depend on oceanic and glaciological parameters as far field velocity, temperature and salinity, shape of the ice front and surface roughness; most of these relations are still to be investigated (Straneo et al., 2013).

Finally, the Stanton numbers have been derived from laboratory studies of boundary layers on flat, smooth plates (Kader et al., 1972) and this parametrization was developed for sloping ice shelves in Antarctica: the validity of equation 1.1 for vertical glaciers has not been tested yet. Thus, it would be necessary to validate the turbulent transfer coefficients for Greenland's glaciers with in situ observations (Straneo et al., 2015).
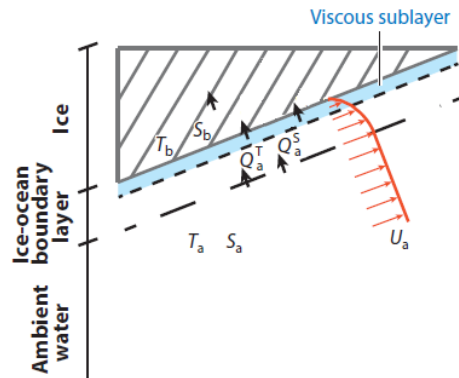
Figure 1.7: Schematic representation of the ice-ocean boundary layer. Figure adapted from Straneo et al. (2015).

1.5.2 Plume region

The plume region is characterised by the presence of a system of rising buoyant plumes driven by submarine melting and subglacial discharge. The first is distributed along the entire depth of the glacier, while the second reaches the fjord through channels discharging at the base of the glacier (Straneo et al., 2015).

Both the buoyant plumes originated by submarine melting or subglacial discharge rise near the glacier front, entraining ambient water, until they reach the surface or their level of neutral buoyancy. Once this occurs, the plume of glacially modified water[10] detaches from the glacier front, intrudes horizontally into the ambient water, and moves away from the glacier as a buoyancy-driven current. A slow flow of ambient water is driven toward the ice, as ambient water is entrained in the rising plumes (Straneo et al., 2015).

Observations have proven the existence of both plumes reaching the surface or glacially modified water intruding at mid-depth. Thus, the plume can reach its neutral buoyancy level at an intermediate depth (Sciascia et al., 2013).

---

[10]Mixture of ambient water and submarine melt and/or subglacial discharge.

For a two-layer stratification, the plume reaches the surface if it's able to penetrate the interface between the two layers, which means if its density at the interface is lower than the upper layer one. In this case, the freshwater is found in the surface layer. If the plume density at the interface is greater than the upper layer density, instead, the freshwater intrudes at depth along the interface. Therefore, the location of freshwater in the water column depends on the source geometry and on the buoyancy flux of the plumes (Straneo et al., 2015). For example, in summer, plumes are expected to reach a lower depth than in autumn, given the greater runoff input, i.e. greater buoyancy forcing, typical of the summer season (see section 1.7.1) (Cowton et al., 2015).

Usually the plume dynamics and the entrainment processes are partially or completely parametrized by a diffusive flux (Straneo et al., 2015).

1.5.3   Cross-fjord variations

Earth rotation typically has scarce influence on fjords circulation, given their narrow shape. Thus, along-fjord or depth variations tend to dominate over cross-fjord variations (Straneo et al., 2010; Johnson et al., 2011; Sutherland et al., 2014).

Isopycnals sloping across the fjord have been found in the fjord of Petermann Glacier (Johnson et al., 2011), whose average width is approximately 20 km, while in e.g. Kangerdlugssuaq Glacier fjord (south-eastern Greenland), whose mean width is $\sim$ 7 km, data have shown that most of the variability occurs in the along-fjord and depth directions (Straneo et al., 2010; Sutherland et al., 2014).

1.5.4   Buoyancy-driven circulation

The freshwater released at the head of Greenlandic fjords forces a buoyancy-driven circulation somewhat different from the classical estuarine one.

In classical estuaries freshwater is discharged at the surface, resulting in an outflow of light water at the surface and an inflow of denser (usually saltier) waters at depth. In glacial fjords, instead, while surface runoff is released at the surface, subglacial discharge and submarine melting constitute a source of freshwater at depth, that moves then towards the surface in the form of buoyant plumes (see section 1.5.2).

Given also the presence of both AW and PW in the fjord (see section 1.3), the buoyancy-driven flow is not described by a classical two layer flow, but by a three or four layer flow, with glacially modified water at the surface and/or at
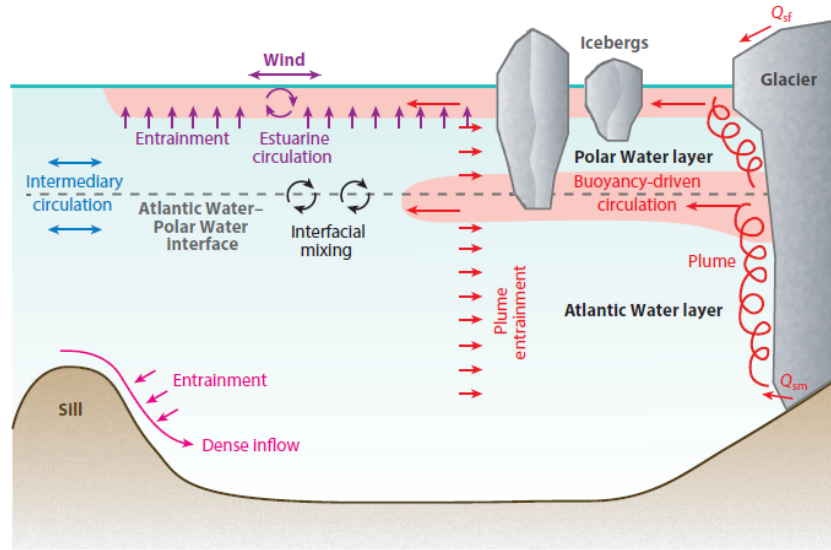
Figure 1.8: Schematic representation of the different circulations in a Greenlandic glacial fjord. Red indicates the buoyancy-driven circulation resulting from the submarine melting, subglacial discharge Q_{sm}, and surface runoff Q_{sf}; purple the estuarine circulation resulting from surface runoff only; blue the intermediary circulation; pink the circulation generated by the dense inflow over the sill. Reproduced from Straneo et al. (2015).

mid-depth, typically between the AW and PW layers (Mortensen et al., 2011; Straneo et al., 2011; Sutherland et al., 2014). This is valid both for winter and summer, although glacially modified water is generally shallower in summer, as a consequence of the stronger runoff input of this season (Cowton et al., 2015). Moreover, some of the icebergs melt while residing in the fjords. If these are deep (below the AW-PW interface), some of this meltwater will be trapped subsurface (Straneo et al., 2015).

The multiple-layers down-fjord current of glacially modified water is balanced by a ticker and slower up-fjord current at greater depth and, to a lesser extent, between the glacially modified water layers. This flow represents the transport of water required to replace the fjord waters entrained into the glacially modified water and subsequently exported from the fjord (Cowton et al., 2015, 2016).

1.5.5 Intermediary circulation

Intermediary flows are shelf-driven flows that occur above the sill depth. They are driven by density variations outside the fjord, which can originate from along-shore winds (upwelling or downwelling) or density anomalies that are advected near the mouth of the fjord (Straneo et al., 2015). The presence of

density variations outside the fjord causes a fjord-shelf density contrast, resulting in horizontal pressure gradients that drive baroclinic currents (Svendsen, 1980; Klinck et al., 1981; Stigebrandt et al., 1990).

In narrow fjords, the horizontal pressure gradient generates vertically sheared flows across the entire width. In wide fjords, instead, rotational effects drive geostrophic adjustment and geostrophic flows.

Intermediary circulation is especially relevant for fjords with sills deeper than the AW-PW interface: any fluctuation of the AW-PW interface on the shelf drives intermediary flows (Straneo et al., 2015).

The south-east Greenland shelf region shows exceptionally strong wind forcing and variability. As a consequence, fjords abutting this region, if characterised by deep sills, present large fjord velocities and heat/salt content variability due to advection from the shelf region, which are often associated with downwelling events (see section 1.6.2). The importance of intermediary circulation in south-east Greenland has been proven in Sermilik and Kangerdlugssuaq fjords (both located there and with sills well below the AW-PW interface) (Inall et al., 2014; Schjøth et al., 2012; Sutherland et al., 2012): moored data have shown that in these fjords intermediary flows dominate the circulation and water properties variability (on a three to ten days time scale) during the non-summer months - i.e. from September to May (Jackson et al. (2014), see figure 1.9).

Fjords on the west coast, instead, are found to have much weaker intermediary flows, given the smaller shelf forcing (Gladish et al., 2015; Mortensen et al., 2014).

In Sermilik and Kangerdlugssuaq fjords, the shelf-driven flows are characterised by strongly vertically sheared velocities, reversing every few days, with a two or three-layer structure, so that current is directed toward the shelf in some layers, toward the fjord head in others (see figure 1.9; Jackson et al. (2016); Sutherland et al. (2014)).

These velocity pulses are usually associated with isopycnals heaving[11], so that they change the thickness of PW and AW layers, significantly altering the fjords heat content. For example, up-fjord flow in the PW layer thickens that layer, increasing the volume of PW relative to AW and decreasing the average water column temperature. Some velocity pulses also advect variability in AW/PW water mass properties (changes within isopycnal layers) from the shelf into the fjord on synoptic time scales (Jackson et al., 2014).

---

[11]Adiabatic motions of the isopycnals associated with the adjustment of wind driven circulation.

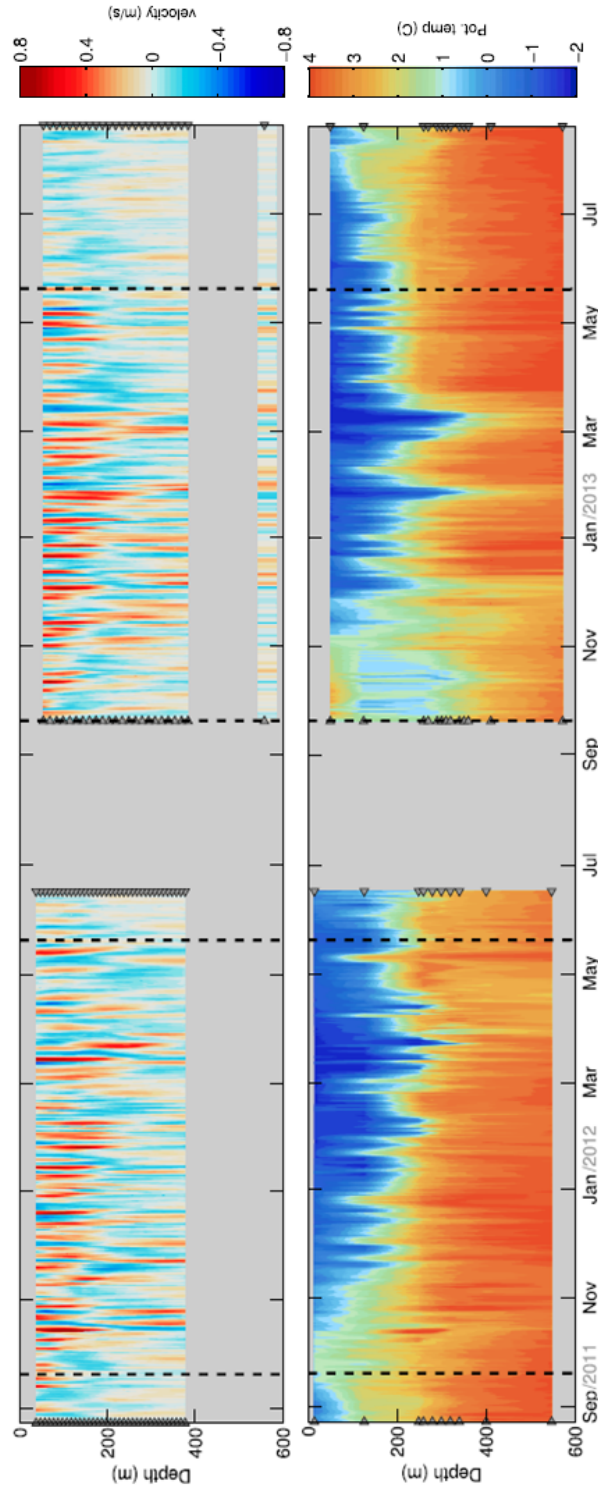Figure 1.9: High-frequency variability in Sermilik fjord from moored observations: along-fjord velocity, positive toward the glacier, and potential temperature from a mooring located in the middle of the fjord. Gray triangles indicate the depths of instruments. Vertical dashed black lines at 20 September and 20 May demarcate the summer vs non-summer regimes. Reproduced from Jackson et al. (2016).

Intermediary circulation is thus capable of driving rapid water exchange with the shelf and of renewing water above sill depth, following the shelf variability, on time scales of days or weeks (Jackson et al., 2014). For example, intermediary flows can explain the renewal of the upper 400 m of Sermilik fjord waters within two months observed by Straneo et al. (2010).
This strong shelf-driven variability also provides large amounts of energy to the fjord, contributing to mixing.

Considering the above cited effects of intermediary circulation, it might also impact on submarine melting and freshwater export. In Jackson et al. (2014), it is suggested that the submarine melt rate should vary significantly throughout non-summer months as a result of the fluctuations in temperature given by intermediary flows. On the basis of modelling studies showing submarine melt rate scaling linearly or quadratically with ambient water temperature (in absence of subglacial discharge) (Sciascia et al., 2013; Jenkins, 2011; Holland P. R. et al., 2008) and considering the fluctuations observed at mid-fjord[12], Jackson, Straneo and Sutherland (2014) hypothesize that submarine melt rate may vary by $\pm 20 - 50\%$ of its mean value on synoptic timescales.

1.5.6 Comparison of the effects of buoyancy-driven and intermediary circulation

As stressed in section 1.2.1.1, fjord circulation controls water properties at marine-terminating glaciers fronts. A way to estimate the timescales over which glaciers draining into a fjord may experience the variations in ocean temperature occurring on the shelf is quantifying the rate at which waters within the fjord are renewed by waters from the shelf.

Since intermediary flows can be an order of magnitude greater than estuarine flows (up to 0.8 $\frac{m}{s}$ compared to less than 0.1 $\frac{m}{s}$) (Stigebrandt et al., 1990; Jackson et al., 2014; Cowton et al., 2016), the transport associated with intermediary flows is much larger than that associated with buoyancy-driven flows: with a model of Kangerdlugssuaq fjord, Cowton et al. (2016) found that intermediary circulation can replace up to $\sim 25\%$ of this fjord waters volume with shelf waters within 10 days (during the passage of a coastal storm), while buoyancy-driven circulation (forced only by subglacial runoff) exchanges $\sim 10\%$ of the fjord waters volume over the same period under typical summer conditions.
However, they argue that buoyancy-driven circulation is the primary conveyor

---

[12]Assuming these temperature fluctuations to be representative of temperature fluctuations near the glacier, i.e. neglecting along-fjord variations.

of shelf water to the glaciers during summer. Tracking shelf water in the fjord with a passive tracer, Cowton et al. (2016) found that the turnover times[13] for winter intermediary circulation or summer buoyancy-driven circulation (respectively $\sim 90 - 130$ days and 105 days, for Kangerdlugssuaq fjord, according to Cowton's model) are much more similar than the total volume exchanges over the time of a single coastal storm written above. This is mainly because shelf water supply to the fjord resulting from two successive wind events notably reduces for the second: the periodically reversing nature of the intermediary circulation makes the imported shelf waters being re-exported back to the shelf rather than transported further up-fjord, with the same water exchanged repeatedly across the fjord mouth as the currents reverse. The buoyancy-driven circulation, instead, is steady over time during the melt season, with a persistent up-fjord current at depth.

Moreover, buoyancy-driven circulation is forced by inputs of freshwater at the head of the fjords, being effective at drawing water up to the glacier termini. The rapid intermediary circulation, on the other hand, can exchange water in the outer part of the fjord on timescales of few days, but it is much less effective at driving shelf water up to the fjord head. Cowton et al. found that, after 100 days, the summer buoyancy-driven circulation could replace $\sim 65\%$ of the waters within the innermost 13 km of Kangerdlugssuaq fjord with shelf water, compared with $< 30\%$ for intermediary circulation.

Therefore, in summer, thanks to the greater freshwater flux (see section 1.7.1) and the weaker and rare wind events (and thus weaker intermediary circulation, see section 1.6.2), buoyancy-driven circulation appears to dominate the up-fjord transport of shelf water.

In winter, instead, given the strong and frequent wind events (at least as far as south-eastern Greenland is concerned) and the minimum runoff, the renewal of fjords waters is likely controlled by intermediary flows.

1.5.7 Deep water renewal

Water below sill depth is periodically renewed by dense water inflow over the sill, along with entrainment of relatively fresher water from above. The residence time of this water, called deep water, depends on mixing rate, intermediary flows, volume of water below sill depth (Stigebrandt, 2012) and glacier-driven circulation. This last one is thought to reduce the residence time of deep

---

[13]Time taken for fjord-shelf exchange to dilute the original contents of the fjord by a factor $1 - e^{-1}$ (i.e. time until the fjord contains 37% of original fjord water and 63% of water imported from the shelf) (Cowton et al., 2016).

water, with respect to the water above sill depth, because of the entrainment
of deep water by the buoyant plumes at depth (Straneo et al., 2015).

The rapid variations, likely due to intermediary flows, found by Jackson et
al. (2014) in Sermilik fjord waters even at 900 m depth suggest shelf-driven
deep water renewal on timescales of months. However, studies in other fjords
have found different renewal times (Johnson et al., 2011) or have hypothesized
different drivers (as the buoyancy-driven circulation; Gladish et al. (2015)),
unrevealing our limited understanding of deep water renewal processes and of
its interactions with glacier meltwater (Straneo et al., 2015).

1.6   Sermilik fjord

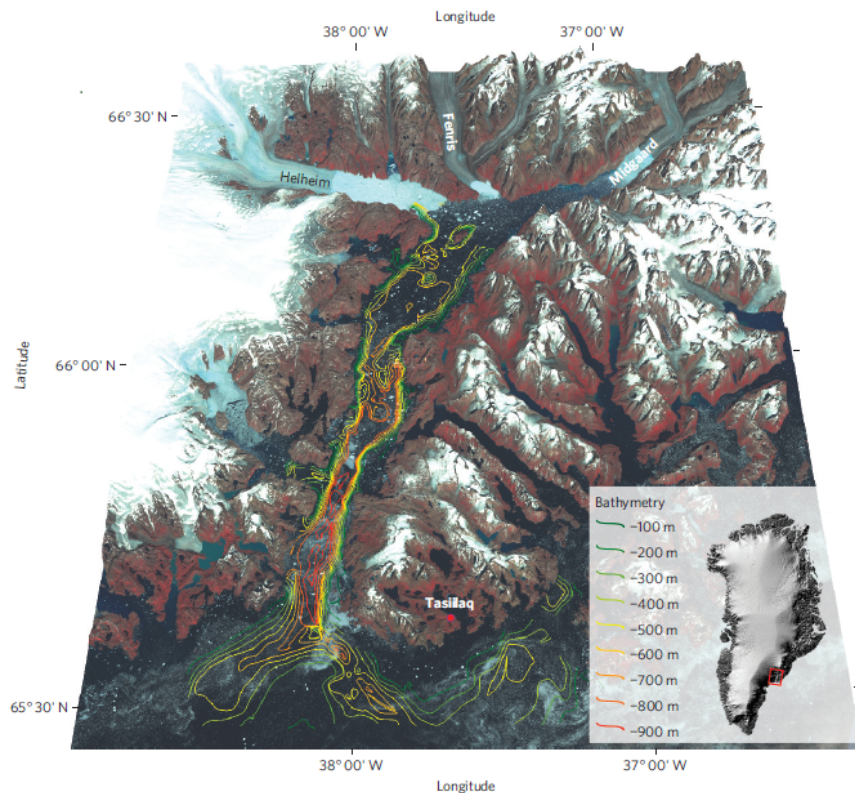Figure 1.10: Sermilik fjord from Landsat dataset with bathymetry superimposed. Reproduced
from Andresen et al. (2012).

Sermilik fjord, located in south-eastern Greenland (see figure 1.10), is 90
km long, 5-10 km narrow, 900 m deep at the mouth and 600 m deep at the
northern end. The shallowest sill, in the upper fjord, is 530 m deep, well
below the AW/PW interface, so that exchanges with the shelf are not impeded

(Jackson et al., 2016).   This allows icebergs to freely drift out of the fjord
without grounding on shallower grounds (Andresen et al., 2012).

Three glaciers discharge in Sermilik fjord: Helheim Glacier, the biggest, that
drains into the north-west corner of the fjord, Fernis Glacier, into the north,
and Midgård, into the north-east corner (see fig.1.10).

Water in the fjord is constituted by four different water masses: AW, PW, and
glacially modified water from submarine meltwater and from runoff (Straneo
et al., 2011).

The shelf region is relatively wide ($\sim$ 150 km) and deep ($\sim$ 200 m). Troughs
or canyons (> 400 m deep) in the shelf extend from the fjord mouth to the shelf
break (Jackson et al., 2018). This shelf shows strong oceanic fronts and large
variability in water properties, enhanced by the troughs that cause diverting
of the East Greenland Coastal Current (an inner branch of the East Greenland
Current, which carries PW into the region, see section 1.3) in close proximity
to Sermilik fjord mouth (Sutherland et al., 2008; Harden et al., 2014). Moored
data showed that 60% of the sub-monthly shelf properties variability is associ-
ated with along-shore, downwelling winds (see section 1.6.2), whereas the rest
is attributed to variability in the East Greenland Coastal Current advected
into the region (Straneo et al., 2015).

Helheim glacier has a typical vertical front and it's characterised by strong
calving, with a thick mélange of icebergs that extends 10-20 km from the glacier
terminus (Foga et al. (2014), see figure 1.11). On the contrary, the fjord is only
rarely covered by land-fast sea ice (Andres et al., 2015).

Outside the mélange, the fjord is littered with transiting icebergs. They can
move faster than 0.1 m/s (Sutherland et al., 2014) and have keels deeper than
300 m (Andres et al., 2015). These features make data collection particularly
difficult.

Figure 1.11: Helheim Glacier at its Sermilik Fjord terminus. Reproduced from Straneo et al.
(2013).

1.6.1   Why we choose Sermilik fjord

Sermilik fjord is one of Greenland's largest fjords. These fjords are associated with the largest glaciers, contributing the most to the recent changes: 15 of Greenland's glaciers account for more than 50% of the GrIS total ice discharge (not including runoff from surface melting, but only icebergs from glaciers calving and submarine melt, Enderlin et al. (2014)).

Helheim Glacier is the fifth-largest outlet of the GrIS in terms of total ice discharge (Enderlin et al., 2014). Moreover, Sermilik fjord is well known, in terms of observational data, with respect to other Greenland's fjords: the presence of data allows us to compare and validate our model results (see e.g. chapter 3). Results from Sermilik are expected to be partially applicable also to other fjords, even though some features may change, as, for example, the magnitude and seasonality of intermediary flows, depending on shelf variability and sill depth (see section 1.5.5) (Jackson et al., 2014).

1.6.2   Wind events in Sermilik fjord and the near shelf

The shelf region the fjord abuts (south-east Greenland's shelf) is energetic and highly variable owing to the presence of intense along-shore winds, called barrier winds, which result from low-pressure systems encountering Greenland's steep topography (Harden et al., 2011). Outside of Sermilik, barrier winds are usually from the north-east, thus causing downwelling phenomena.

These winds are characterised by a strong seasonality: non-summer months show frequent strong events, while during summer the forcing is weaker and less frequent. According to an ERA-Interim reanalysis climatology, barrier winds intensity peaks in February and it's weakest in July (Jackson et al., 2016).

In addition to along-shore shelf winds, Sermilik fjord is affected by strong and cold along-fjord down-slope winds, called *piteraqs*, that reach intensities of several tens of m/s (Oltmanns et al., 2014).

The flow originates from the Greenland ice cap where the radiational cooling of the boundary layer produces a katabatic wind that accelerates over the steeper slopes at the coast, advecting cold dense air. Therefore, down-slope wind events coincide with a surface air temperature drop inside the fjord (Oltmanns et al., 2014).

Along-fjord winds seasonality is similar to shelf winds one: there are occasional down-slope events in the non-summer months and almost none in the summer (Oltmanns et al., 2014).

Down-slope winds usually drive outflow in the upper layer of the fjord (Sutherland et al., 2014). However, they are almost always followed by strong alongshore shelf winds, making their influence difficult to separate from that of the shelf winds (Jackson et al., 2016). Moreover, the down-slope wind events are less frequent than along-shore winds: the strongest of them happen ~ 4 times per year, while the shelf-forced flows are nearly continuous throughout the year, being thus these last ones, and not the former, the principal drivers of fjord water variability (Jackson et al., 2018).

Nonetheless, the presence of down-slope wind events is still of notable importance: since they are directed offshore, they can advect sea ice offshore (Bromwich et al., 1984), reducing coastal sea ice cover. For example, Oltmanns et al. (2014) estimated a 29% reduction of sea ice inside Sermilik Fjord and a 26% on the surrounding shelf compared to the mean sea ice concentration the week before a wind event. This could explain the mobility of the ice cover in Sermilik fjord (see the beginning of section 1.6).

Water in Irminger Sea (off the south-east Greenland's coast) is warmer than that near the coast, thus causing faster melting of the sea ice advected offshore (Sutherland et al., 2012). This could lead to a local freshening of Irminger Sea, which is an important ocean convection region (Pickart et al., 2003; Vage, 2010), also contributing to the AMOC (Jungclaus et al., 2005; Stouffer et al., 2006).

Furthermore, sea ice has insulating properties and regulates the entering of sunlight in surface water: its removal impacts on surface water energy balance. Finally, it has been found that the presence of the ice mélange near outlet glaciers is important for glacier stability since it exerts back pressure on the glacier, inhibiting calving (Amundson et al., 2010). Removal of the local sea ice cover may then contribute to the destabilization of Helheim Glacier causing further glacier retreat (Howat et al., 2010; Walter et al., 2012; Oltmanns et al., 2014).

1.7   Dynamics of Sermilik fjord

1.7.1   Buoyancy-driven circulation

In Sermilik fjord, surface runoff and, as a consequence, subglacial discharge form only from June to August, when air temperatures are above freezing, the first having a peak in July and decaying to zero in September. This seasonality modulates the glacier-driven circulation and probably submarine melt rate, which should increase with subglacial discharge (see section 1.4).

Nonetheless, submarine melting is controlled also by a number of other factors, as AW temperature, density of the ice mélange, fjord stratification, presence of PW, isopycnal heaving and plumes distribution (Jackson et al., 2016). Indeed, using an idealised fjord model not taking into account intermediary circulation, Cowton et al. (2015) found that runoff variability, particularly on an interannual time scale, results only in a weak variability in submarine melt rate across the full width of the glacier, arguing that the ice front directly exposed to the runoff-driven buoyant plumes might be only a small part of the entire glacier margin. However, this result is still strongly dependent on the spatial distribution of subglacial discharge (see section 1.4) and on the poorly constrained melt rate (see section 1.5.1).

Jackson and Straneo (2016) calculated the ratio between runoff (surface and subglacial discharge) and submarine meltwater fluxes (from both glacier and icebergs) in August to be 1.1 ± 0.8 for Sermilik fjord, suggesting also that runoff may not be the predominant source of buoyancy forcing to the fjord during summer, in opposition to previous observational studies of glacial fjords that found ratios between 2 and 31 (Motyka et al., 2013; Xu et al., 2013; Rignot et al., 2010; Motyka et al., 2003).

From moored observations, Jackson and Straneo (2016) found that during winter Sermilik fjord is a two layer system, with peak stratification between 150 and 250 m. In summer, instead, the stratification is stronger and increases toward the surface.

Below approximately 200 m, fjord water characteristics match shelf water ones, while above 200 m fjord water properties may differ from shelf water depending on the season. During summer and fall, waters above 200 m show modification from mixing with submarine melting and runoff: a considerable part of the upper layer could probably be a mixture of deep AW upwelled through mixing with glacial freshwater (see section 1.7.3). In winter and spring (February-May), instead, there's no modification due to runoff and, in the upper layer, fjord water characteristics converge to shelf PW ones. At the same time, modifications due to submarine melting appear near the AW-PW mid-depth pycnocline and probably also near the surface.

1.7.2   Intermediary circulation

Jackson, Straneo and Sutherland (2014) showed that from September to May Sermilik fjord velocity field is dominated by a shelf-forced circulation consisting in a fast and fluctuating two-layer flow: the upper layer velocities are typically $0.3 - 0.5 \ \frac{m}{s}$, occasionally exceeding $0.8 \ \frac{m}{s}$. These velocity pulses are asso-

ciated with shelf density fluctuations and most are preceded by along-shore, downwelling-favourable winds on the shelf. The Ekman transport resulting from these winds causes the shelf isopycnals to be depressed and raises the sea surface[14] towards the coastline, driving inflow in the upper layer of the fjord and outflow in the lower layer. After a downwelling event, the mid-depth AW-PW pycnocline, that was before depressed, rebounds, rising, and velocity reverses, with outflow in the upper layer of the fjord and inflow in the lower (see figure 1.9).

The relation between shelf pycnocline fluctuations and shelf winds is remarked by the high coherence found between shelf wind and shelf density at periods of two to ten days. The energy of these shelf-forced flows in the fjord coherently peaks at periods of 3-10 days (Jackson et al., 2014).

The vertical displacements of the pycnocline in the fjord can range from tens of meters to one hundred meters; these excursions, together with the AW and PW properties changes advected from the shelf, dominate fjord water temperature and salinity variability.

Comparing moored density records from the shelf, mid-fjord and upper fjord, Jackson et al. (2014) observed that a signal takes less than a day to reach the head of the fjord from the mouth. Thus, pycnocline heaving, which occurs over synoptic time scales, is approximately uniform throughout the fjord on time scales longer than a day. Moreover, from the comparison of the moored data, emerges that toward the head of the fjord velocity decays, while pycnocline depth fluctuations are slightly amplified (Jackson et al., 2018).

As expected from the summer reduction of wind forcing on the shelf (see section 1.6.2), intermediary flows are much less energetic during summer, as also the amplitude of fjord density fluctuations diminishes (see again figure 1.9): in summer months the standard deviation of the pycnocline depth, approximated by the 26.6 $\frac{kg}{m^3}$ isopycnal, is reduced by 57%, while the mean speed is reduced by 59% in the moored data collected by Jackson et al. (2016).

1.7.3   Freshwater, heat and salt fluxes

Through extensive measurements from midfjord moorings, Jackson and Straneo (2016) observed that in Sermilik fjord, from September to May (non-summer months), the advective heat and salt transports from the shelf are balanced by changes in heat and salt storage. During these seasons, the freshwater fluxes, as well as the heat extracted from the ocean to melt ice, were found to be indistinguishable from zero.

---

[14]The sea surface is raised by $\sim$ 15 cm on the shelf and at mid-fjord (Jackson et al., 2014).

In summer (from June to August), as shelf-forced flows are reduced, a clear structure emerges in the flow averaged over time so as to remove intermediary circulation component (see figure 3.1): AW flows toward the glacier at depth, upwells through mixing with glacial inputs and flows away from the glacier in an upper layer of glacially modified water, consisting of a mixture of AW, submarine melt and runoff (Straneo et al., 2011; Jackson et al., 2016).

According to Jackson and Straneo, during this period, the total freshwater flux becomes distinguishable from zero and increases from June to August. Regarding salt and heat budgets, warm and salty water inflowing at depth and cooler and fresher water outflowing in the upper layer result in an import of heat and salt in the fjord. This import of salt is balanced by an export of salt resulting from barotropic currents, while the import of heat is counterbalanced by the extraction of heat to melt ice and by changes in heat storage. The ocean heat employed to melt ice becomes distinguishable from zero in July and is a leading-order term in the heat budget by August.

1.8 Thesis objectives

The purpose of this thesis is to simulate the Sermilik fjord dynamics with a high resolution nested model, in order to unravel the characteristics and drivers of the fjord circulation. We will use a numerical primitive equation general circulation model to realistically represent the three-dimensional fjord circulation, including the local effects of large scale changes on the shelf, using nesting techniques (see chapter 2 and, in particular, section 2.2.4). We will not insert glacier melting in our simulation: we will therefore focus on the analysis of the interactions of the fjord circulation with the shelf dynamics.

We will exploit the nested configuration of our model to demonstrate the importance of shelf circulation as a trigger of fjord circulation, analysing fjord dynamics variability on different time scales, from the seasonal to the daily: we will study intermediary circulation, its seasonal changes and the effects on the fjord of the shelf-scale and basin-scale circulation seasonal variations.

Moreover, the use of a model will give us the ability to carry out sensitivity experiments to the atmospheric forcings, so as to be able to identify the drivers of the fjord circulation modes. In particular, we will be able to assess the time and spatial scale of the intermediary circulation forcing.

In addition, the model high spatial resolution allows us to investigate the influence of the shelf processes on the part of the fjord nearest to Helheim glacier, that could not be adequately modelled in literature models with lower resolu-

tion, given the fjord head narrowness, and whose properties can't be directly observed as a consequence of the presence of the ice mélange (see section 1.4): we will be able to assess the real impact that intermediary circulation has on water properties near the ice, and, thus, on glacier melting. We will unravel what is the extent of the heat and salt transport to the glacier that this circulation causes, so as to pave the way for future studies of the influence that long-term changes in Atlantic and Polar Water properties may have on the glaciers: the understanding of the dynamics that repeatedly carries heat to the glaciers on short (synoptic) time scale is indeed essential to discern how and how quickly these much slower changes may reach out to the fjord head. Furthermore, this thesis will show for the first time the successful downscaling of a global ocean prediction model to the fjord scale and will make justified statements about future modelling requirements for climate downscaling.

Large scale and shelf scale numerical models

Contents

2.1   Large scale modelling: GOFS16

GOFS16 is the CMCC (Euro-Mediterranean Center for Climate Change) short-term predictions operational ocean forecasting system. It uses 98 unevenly-spaced[1] vertical levels and a tripolar grid[2] with a horizontal resolution of 6.9 km (1/16°) at the equator (~3 km at Sermilik fjord latitude), thus being one of the few mesoscale eddies resolving[3] operational systems in the world (Iovino et al., 2016, 2018).

GOFS16 is based on an eddying global modelling framework called NEMO (Nucleus for European Modelling of the Ocean, version 3.4). NEMO numerical model is a coupled ocean/sea-ice model, including a three-dimensional primitive equation ocean general circulation model (OPA, Océan Parallélisé, see section 2.1.1) and a dynamic-thermodynamic sea-ice model (LIM2EVP, Louvain-la-Neuve sea Ice Model, Fichefet et al. (1997)) (Iovino et al., 2016).

NEMO is coupled to a three-dimensional variational data assimilation scheme[4], called OceanVar (Storto et al., 2015), to provide daily initialization fields. The

---

[1]The vertical grid spacing increases from approximately 1 m near the surface to 160 m in the deep ocean.

[2]The location of the geographical South Pole is conserved, while two distinct poles are introduced in the northern hemisphere, in order to avoid singularities associated with the convergence of meridians at the North Pole.

[3]Mesoscale eddies pervade the ocean at all latitudes and usually account for the peak in the kinetic energy spectrum. Most of their energy comes from baroclinic instabilities of large-scale flows. Their presence is fundamental for e.g. transporting and mixing temperature and salinity, controlling the mechanisms of deep water spreading and deep convection pre-conditioning, and modulating air-sea interactions (Morrow et al., 2012; Iovino et al., 2016). The horizontal length scale of mesoscale eddies is given by the first baroclinic Rossby radius of deformation, defined as $R = \frac{N \cdot H}{f}$, where N is the Brunt-Väisälä frequency, H the depth scale, f the Coriolis parameter, thus varying with stratification, depth and latitude. While at the tropics R is of the order of 200 km, at 50-60° is around 10-20 km (Chelton et al., 1998). A mesoscale resolving, or eddy-permitting, model must use a horizontal grid resolution finer than R. As a consequence, the necessary resolution varies with latitude, being a 1/10° (~12 km) resolution sufficient below a latitude of 50° (Smith et al., 2000), but not more in the continental shelf of the Arctic region, our region of interest, where R is just few kilometres (Nurser et al., 2014).

[4]Variational data assimilation methods are those which provide an analysis $\mathbf{x}^a$ via the minimization of a prescribed cost function J: this is typically the sum of the squared deviations

system assimilates salinity and temperature profiles, sea surface temperature, sea surface height and sea-ice concentration on a daily basis. This improves the forecast performance since combines the information that comes from our knowledge of ocean dynamics (the ocean circulation model) with the global ocean observing system data.

GOFS16 is forced with 6-hourly momentum, daily radiation and daily precipitation fluxes from the operational NCEP Global Forecast System fields (NCEP GFS, 2015). The spatial resolution of NCEP GFS is 1/4°.

The forecast system runs once a day to produce a 6-day forecast. Results include global sea surface height, three-dimensional temperature, salinity and velocity fields, sea-ice thickness, concentration and drift (Iovino et al., 2018).

Through the Structured and Unstructured Relocatable ocean model for Forecasting (SURF), nested within the global operational model (see section 2.2), GOFS16 is used for regional and coastal downscaling in several regions of the world ocean.

2.1.1 NEMO-OPA

In the following we mainly refer to NEMO manual (Madec and the NEMO team, 2016).

2.1.1.1 Governing equations

NEMO-OPA is a primitive equation, free-surface[5], finite differences, 3-D ocean model, built for modelling ocean circulation at regional and global scales. It

---

of the analysis values from the observations $\mathbf{y}$, weighted by the accuracy of the observations $\mathbf{R}$ (the observations error covariance matrix), plus the sum of the squared deviations of the forecast fields $\mathbf{x}^b$ from the analyses, weighted by the accuracy of the forecast $\mathbf{B}$ (the forecast error covariance matrix). The term *three dimensional* is referred to the particular form of the cost function used: $J(\mathbf{x}) = \frac{1}{2}(\mathbf{x} - \mathbf{x}^b)^T \mathbf{B}^{-1}(\mathbf{x} - \mathbf{x}^b) + \frac{1}{2}(\mathbf{y} - h(\mathbf{x}))^T \mathbf{R}^{-1}(\mathbf{y} - h(\mathbf{x}))$, where h is the relation between the analysis fields and the observations. The resulting analysis is given by $\mathbf{x}^a = \min_{\mathbf{x}} J(\mathbf{x})$.

[5]A variable η is introduced to describe the sea-surface height with respect to a reference height $z = 0$. This variable is solution of a prognostic equation: $\frac{\partial \eta}{\partial t} = -\nabla \cdot [(H + \eta)\mathbf{U}_{BT}] + P - E$, where H is the positive ocean depth with respect to $z = 0$, $\mathbf{U}_{BT}$ is the vertically averaged horizontal velocity vector (see section 2.2.2.1), E and P are the volume fluxes of water through the surface due to evaporation and precipitation.

In GOFS16 (and also in SURF, see section 2.2) a linear free-surface formulation is adopted: a linearised version of the previous equation is used, the vertical levels thickness is constant in time (also the one of the first level at surface) and the vertical boundary conditions (see section 2.1.1.3) are applied at the fixed surface $z = 0$ rather than on the moving surface $z = \eta$.

solves the Navier-Stokes primitive equations under the hydrostatic[6] and Boussinesq[7] approximations, along with a turbulence closure[8] and a nonlinear equation of state which couples temperature and salinity with momentum and mass conservation. The fluid is assumed to be incompressible.

The coordinate reference system chosen is a curvilinear spherical one with an orthogonal set of unit vectors (**i**,**j**,**k**) linked to the earth such that **k** is the local upward vector and (**i**,**j**) are two vectors orthogonal to **k** (tangent to the geopotential surfaces, which are assumed to be spherical).

The vector invariant form of the primitive equations[9] in the (**i**,**j**,**k**) vector system is given by the following six equations (the momentum balance, the hydrostatic equilibrium, the incompressibility equation, the heat and salt conservation equations and an equation of state):

$$\frac{\partial \mathbf{U}_h}{\partial t} = - \left[(\nabla \times \mathbf{U}) \times \mathbf{U} + \frac{1}{2}\nabla(\mathbf{U}^2) \right]_h - f\mathbf{k} \times \mathbf{U}_h - \frac{1}{\rho_0}\nabla_h p$$
$$- A^{lm}\nabla^4 \mathbf{U}_h + \frac{\partial}{\partial z}\left(A^{vm}\frac{\partial \mathbf{U}_h}{\partial z}\right) + \mathbf{F^U} \tag{2.1}$$

$$\frac{\partial p}{\partial z} = -\rho g \tag{2.2}$$

$$\nabla \cdot \mathbf{U} = 0 \tag{2.3}$$

$$\frac{\partial \theta}{\partial t} = -\nabla \cdot (\theta \mathbf{U}) + \nabla \cdot (A^{lT}\nabla\theta) + \frac{\partial}{\partial z}\left(A^{vT}\frac{\partial \theta}{\partial z}\right) + \mathbf{F}^T \tag{2.4}$$

$$\frac{\partial S}{\partial t} = -\nabla \cdot (S\mathbf{U}) + \nabla \cdot (A^{lT}\nabla S) + \frac{\partial}{\partial z}\left(A^{vs}\frac{\partial S}{\partial z}\right) + \mathbf{F}^S \tag{2.5}$$

$$\rho = \rho(\theta, S, p) \tag{2.6}$$

where:

- $\mathbf{U} = (u, v, w)$ stands for the three-dimensional velocity vector;

- $\mathbf{U}_h$ is the horizontal velocity vector;

- t and z are the time and vertical coordinates;

---

[6]The vertical momentum equation (2.2) is given by a balance between vertical pressure gradient and buoyancy forcing.

[7]Density is assumed to be constant in all the Navier-Stokes equations terms, except for the buoyancy term (right hand side of equation 2.2).

[8]Turbulence moments for which explicit equations are not used are written as a function of moments of lower order, so as to equal the number of unknowns and equations after, for example, a Reynold's decomposition.

[9]Invariant under coordinate transformations so that they can be applied uniformly in any orthogonal curvilinear coordinate system such as spherical coordinates, avoiding the explicit representation of new metric terms, thanks to the identity $(\mathbf{U}\cdot\nabla)\mathbf{U} = (\nabla\times\mathbf{U})\times\mathbf{U} + \frac{1}{2}\nabla(\mathbf{U}^2)$ (mitgcm.org).

- θ, S and p are potential temperature, salinity and pressure;

- $f = 2\boldsymbol{\Omega} \cdot \mathbf{k}$ is the Coriolis parameter ($\boldsymbol{\Omega}$ the Earth angular velocity);

- g the gravitational acceleration;

- ρ_0 a reference density;

- ρ the in situ density given by the modified UNESCO equation of state formula by Jackett and Mcdougall (1995);

- A^{lm}, A^{vm} are the horizontal and vertical eddy viscosity coefficients;

- $A^{lT,S}$, $A^{vT,S}$ the horizontal and vertical eddy diffusivity coefficients;

- $\mathbf{F^U}$, $\mathbf{F}^T$, $\mathbf{F}^S$ the surface forcing terms.

The second and third terms from the end in equations 2.1, 2.4, 2.5 are the parametrisations of sub-grid scale physics (e.g. turbulence) for momentum, temperature and salinity: in GOFS16 a horizontal biharmonic operator is used to represent the lateral subgrid-scale mixing for momentum, while lateral tracers mixing and vertical tracers and momentum mixing are parametrised through the Laplace operator. The same for SURF (see section 2.2), except for the use of the Laplace operator also for lateral momentum mixing.

The horizontal eddy viscosity and diffusivity coefficients (A^{lm}, $A^{lT,S}$) are chosen to be constant in space and time, while, instead, the vertical eddy viscosity and diffusivity coefficients (A^{vm}, $A^{vT,S}$), comprising all the vertical sub-grid scale physics, can be specified as a function of the local fluid properties or with a turbulence closure model. In GOFS16, A^{vm} and $A^{vT,S}$ are computed through the TKE turbulence closure scheme, based on a prognostic equation for the turbulent kinetic energy and a closure assumption for the turbulent length scales. SURF (see section 2.2), instead, uses the Pacanowski-Philander mixing parametrization (Pacanowski et al., 1981), in which A^{vm} and $A^{vT,S}$ are a function of the local Richardson number $R_i = N^2/(\partial_z \mathbf{U}_h)^2$ (being N the Brunt-Väisälä frequency).

2.1.1.2 Spatial discretization

The NEMO governing equations are spatially discretised in finite differences on a staggered Arakawa C-type grid (Arakawa et al, 1977). Scalar quantities (sea level height, density, pressure, horizontal divergence, temperature and salinity) are located at the centre of grid cells (T-grid); while velocities (u, v and w) are shifted by half a grid to the centre of the grid faces in three different directions: west/east for zonal velocity (U-grid), south/north for meridional velocity (V-grid), up/down for vertical one (W-grid) (see fig. 2.1).
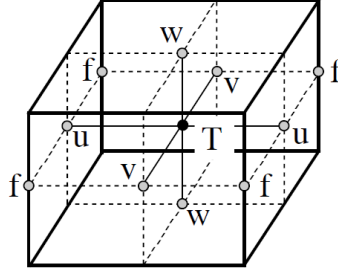
Figure 2.1: Arrangement of variables using Arakawa C-type grid. T indicates scalar points where scalar quantities are defined; u, v and w indicate vector points where the three components of velocity are defined; f indicates vorticity points where both relative and planetary vorticities are defined. Reproduced from Madec and the NEMO team (2016).

2.1.1.3   Boundary conditions

Surface boundary conditions   At the surface, the vertical velocity, momentum, salinity and heat fluxes are prescribed by

$$w|_{z=\eta} = \frac{D\eta}{Dt} + E - P \tag{2.7}$$

$$A^{vm} \frac{\partial \mathbf{U}_h}{\partial z}\bigg|_{z=\eta} = \frac{\boldsymbol{\tau}}{\rho_0} \tag{2.8}$$

$$A^{vs} \frac{\partial S}{\partial z}\bigg|_{z=\eta} = (E - P)S|_{z=\eta} \tag{2.9}$$

$$A^{vT} \frac{\partial \theta}{\partial z}\bigg|_{z=\eta} = \frac{Q_{ns}}{\rho_0 c_p} \tag{2.10}$$

where:

- η is the sea surface height with respect to a reference height $z = 0$. Actually, in GOFS16 and SURF (see section 2.2), since a linear free surface formulation is adopted (see footnote in section 2.1.1.1), the conditions in equations 2.7, 2.8, 2.9 and 2.10 are applied at $z = 0$ rather than at $z = \eta$;

- $\boldsymbol{\tau}$ is the wind stress;

- E and P are the volume fluxes of water through the surface due to evaporation and precipitation;

- $\frac{D\eta}{Dt}$ is a total derivative, i.e. $\frac{D\eta}{Dt} = \frac{\partial \eta}{\partial t} + \mathbf{U}_h|_{z=\eta} \cdot \nabla_h \eta$

- c_p is the ocean specific heat;

- Q_{ns} is the non-penetrative part of the net surface heat flux Q (positive when received by the ocean). Q can be divided into four terms:

$$Q = Q_{sr} + \underbrace{Q_{lw} + Q_s + Q_e}_{Q_{ns}}$$

Q_{sr} is the short wave heat flux, Q_{lw} is the long wave portion of the net radiation received at the sea surface, Q_s the sensible heat flux and Q_e the latent heat flux.

Bottom boundary conditions   At the bottom, the normal components of velocity, heat and salt fluxes are null and the friction is modelled by a quadratic function. These conditions are expressed, respectively, by

$$w|_{z=-H} = -\mathbf{U}_h|_{z=-H} \cdot \nabla_h(H) \tag{2.11}$$

$$A^{v_{T,S}} \left. \frac{\partial(\theta, S)}{\partial z} \right|_{z=-H} = 0 \tag{2.12}$$

$$A^{v_m} \left. \frac{\partial \mathbf{U}_h}{\partial z} \right|_{z=-H} = C_b \sqrt{u|^2_{z=-H} + v|^2_{z=-H} + e_b} \; \mathbf{U}_h|_{z=-H} \tag{2.13}$$

where:

- H is the (positive) ocean depth with respect to a reference height $z = 0$;

- C_b is the bottom drag coefficient;

- e_b a bottom turbulent kinetic energy due to tides, internal waves breaking and other short time scale currents.

Lateral closed boundary conditions   Along the coastline ($\partial\Omega$), the normal components of heat and salt fluxes are null:

$$A^{l_{T,S}} \left. \frac{\partial(\theta, S)}{\partial n} \right|_{\partial\Omega} = 0 \tag{2.14}$$

A no-slip condition is applied for SURF (see section 2.2), a free-slip condition for GOFS16:

$$(\mathbf{U} \cdot \hat{n})|_{\partial\Omega} = 0 \tag{2.15}$$

for both SURF and GOFS16;

$$(\mathbf{U} \cdot \hat{t})|_{\partial\Omega} = 0 \tag{2.16}$$

for SURF only, where $\hat{n}$ is the unit vector in the normal to the coast direction and $\hat{t}$ is the unit vector in the tangential to the coast direction.

2.2   Shelf scale modelling: SURF

The actual global data-assimilative ocean models are capable of realistically simulate mesoscale eddies and interactions with other components of the climate system (e.g. atmosphere and sea ice) (see section 2.1). Despite this, many practical applications (e.g., calculating the probability of extreme events, forecasting oil spill trajectories, supporting marine search and rescue, navigation routing, monitoring ship traffic and interpreting the movement of tagged marine animals) require information on smaller spatial scales and it's not practically feasible to model the global atmosphere/ocean with the spatial resolution needed (Katavouta and Thompson, 2016).

Moreover, some large-scale processes, as, for example, western intensification of boundary currents or propagating Rossby waves, often control regional ocean conditions, leading to the need for downscaling to help estimate local and regional features from coarser scale patterns (Katavouta and Thompson, 2016). Thus, while large scale (coarse resolution) models are used to simulate the large scale dynamics with appropriate parametrizations for the subgrid-scale processes, limited-area regional models (finer resolution) resolve smaller spatial and temporal scale processes, trying to adequately represent the influence of the dynamical processes occurring outside the modelled domain (simulated by large-scale models) on their internal dynamics. This is done providing the initial and open boundary conditions for limited-area models from large scale models (see section 2.2.2) (Oddo and Pinardi, 2008).

The Structured and Unstructured Relocatable ocean model for Forecasting (SURF) is a numerical platform for the short-time forecasts of hydrodynamic and thermodynamic fields that characterise ocean circulation at high spatial and temporal resolutions. SURF is designed to be embedded into any region of a large scale ocean prediction system, in this case GOFS16 (see section 2.1), via downscaling: it is the *child* or *nested* model of a *parent* or *nesting* coarser resolution model that provides the child initial and lateral open boundary conditions (Trotta et al., 2016).

It is possible to include multiple nesting with increasing resolution consecutive nested models, starting from the large-scale parent model. For each nesting, the current model provides the initial and lateral open boundary conditions for the successive one; each parent model can have different numerical discretisation and physical parametrisations (e.g. viscosity and diffusivity coefficients) than its child (Trotta et al., 2017).

SURF high-resolution ocean forecasts are provided to the offshore oil spill com-

panies in order to define optimal and safer conditions of work at sea and, in the future, establish risk and hazard mapping (Iovino et al., 2018). Moreover, Trotta et al. (2016) proved that the increase in resolution, along with the applications listed above, is capable of improving the quality of the forecasts, thanks to the better representation not only of ocean dynamics, but also of coastal geometry and bathymetry.

SURF includes three basic components:

- a structured grid hydrodynamic model based on the NEMO code (Madec and the NEMO team (2016), see section 2.1.1);

- an unstructured grid hydrodynamic model based on the SHYFEM code (Umgiesser et al., 2004; Bellafiore et al., 2010), useful for representing coasts complex geometry;

- a wave model based on the SWAN code (Booij et al., 1999), since coastal and shelf circulations should be coupled with surface wind waves (McWilliams et al., 2004; Breivik et al., 2015).

Here we focus on the structured grid component only, since we will only take advantage of this one in the following chapters of the thesis. We leave the implementation of SHYFEM, that will help in the representation of coastal scale dynamics, and the coupling with SWAN to further studies.

Unfortunately, SURF doesn't include a coupled ice model yet, preventing us from studying glacier-driven circulation, but only shelf-driven one.

2.2.1   SURF model characteristics

In this section we describe the technical characteristics of the SURF standard structured grid component and the SURF model work-flow.

Governing equations, spatial discretization, surface, bottom and lateral closed boundary conditions are described in details in section 2.1.1, since SURF structured component is based on NEMO-OPA code (version 3.6).

In the following we mainly refer to Trotta et al. (2016).

2.2.1.1   Horizontal and vertical grids

The horizontal grid is a regularly spaced latitude/longitude grid in a spherical coordinate system: it has coordinate axes aligned with parallels and meridians and constant spacing in both latitude and longitude directions. Hence, it is simply defined by setting the number of points and the grid sizes in the zonal

and meridional directions, and the reference longitude and latitude coordinate
of the lower left corner of the T-grid.

In the vertical direction, SURF employs $N = 100$ stretched z-coordinate
vertical layers which are distributed in such a way as to better resolve the
surface and intermediate layers: the nearly uniform vertical locations of levels
at the ocean top and bottom, with distances between consecutive layers shorter
at the top (minimum distance: 0.6 m) than at the bottom (maximum: 18 m),
are divided by a smooth hyperbolic tangent transition.
Thus, according to what prescribed in the NEMO code (Madec and the NEMO
team, 2016), the locations of the T-grid vertical levels are given by the following
analytic expression:

$$z(k) = h_{sur} - h_0 k - h_1 log \left[cosh \left(\frac{k - h_{th}}{h_{cr}} \right) \right] \tag{2.17}$$

where k indicates the vertical level considered ($k = 1, 2, ..., N$), h_{cr} denotes the
stretching factor of the grid, h_{th} the approximate model level at which maxi-
mum stretching occurs and h_{sur}, h_0, h_1 are defined from h_{cr}, h_{th}, the number
of vertical levels N, the maximum depth z_{max} and the top layer minimum
thickness dz_{min}.
Partial cell parametrisation is used: the first vertical level located under $z = -H$ is shifted to $z = -H$, so that the bottom layer thickness varies with
geographical location, following the real bathymetry.

2.2.1.2   Time-steps

To solve the three-dimensional prognostic equations for active tracers and mo-
mentum, SURF adopts the split-explicit free surface (or time-splitting) formu-
lation (Griffies, 2004), separating the fast barotropic part (e.g. fast propagating
external gravity waves) and the slow baroclinic part of the dynamics.
Baroclinic velocities and tracers, depth dependant prognostic variables that
evolve more slowly, are solved with a larger time-step Δt (depending on the
horizontal resolution, in order to satisfy the CFL condition); the barotropic
part of the dynamical equations (the free surface equation and the associated
barotropic velocity equations), instead, is integrated explicitly with a shorter
time-step Δt_e (the external mode or barotropic time-step), which is provided
through the name-list parameter nn_baro as: $\Delta t_e = \Delta t / nn\_baro$. nn_baro
must also be chosen in such a way as to make Δt_e satisfy the CFL criterion.

2.2.1.3 Open boundary conditions

Because of the adoption of the time-splitting formulation (see paragraph 2.2.1.2), the lateral open boundary conditions must be formulated separately for the barotropic and baroclinic modes. The algorithms used are the Flather scheme for barotropic velocities and sea surface height and the Flow relaxation scheme for baroclinic velocities and active tracers.

Given the particular importance that open boundary conditions hold in the dynamical downscaling problem, they are treated separately in section 2.2.2.

2.2.1.4 Diffusivity and viscosity coefficients

The horizontal eddy diffusivity and viscosity coefficients, constant in space and time, can be directly specified through the correspondent name-list parameters or they can be obtained from the parent coarse resolution model ones. In the latter case, if a_0 is e.g. the parent viscosity, the child correspondent coefficient is $a = a_0 \left(\frac{\Delta x_F}{\Delta x_L} \right)^m$, where Δx_F and Δx_L are respectively the fine and large scale model grid spacings and m is to be chosen on the basis of the model numerical stability issues and on the basis of the parametrisations used for sub-grid scale lateral mixing (see section 2.1.1.1).

The vertical eddy viscosity and diffusivity coefficients are computed following the Richardson-number dependent scheme of Pacanowski and Philander (1981). Where there might be unstable stratification, they are replaced by a higher value of $10 \ \frac{m^2}{s}$.

2.2.1.5 SURF work-flow

SURF works on a Linux virtual machine environment where the three model components (written in fortran), inputs data, numerical outputs and several pre- and post-processing tools (written in NCL, NCO and python and specifically developed for SURF) are reciprocally connected.

The user has to initially choose the simulation parameters for NEMO. When these are set, the system accesses the following input datasets: bathymetry, coastline, parent model u, v, T, S and η fields and atmospheric forcings.

After these first two steps, the numerical grid is generated and data are reformatted, computing the atmospheric forcing, bathymetry, boundary and initial conditions datasets on the child grid through interpolation. This is done using the sea-over-land procedure (Kara, 2007; De Dominicis, 2014): this method is necessary to provide the input fields in the areas near the coast where the parent model variables are not defined, due to the coarser representation of bathymetry

and coastline on the large-scale model grid. The sea-over-land procedure hor-
izontally extrapolates the coarse resolution model ocean variables on the land
grid points for each vertical level, in order to interpolate these quantities to the
child grid in between. This is applied also to atmospheric fields, so as to avoid
land contaminations near the coast, given the different characteristics of sea
and land boundary layers. To perform the interpolation a bilinear method is
used in the horizontal (only for the structured grid component), while a linear
one is adopted in the vertical direction.

As a final step, numerical integration produces the outputs, which can be
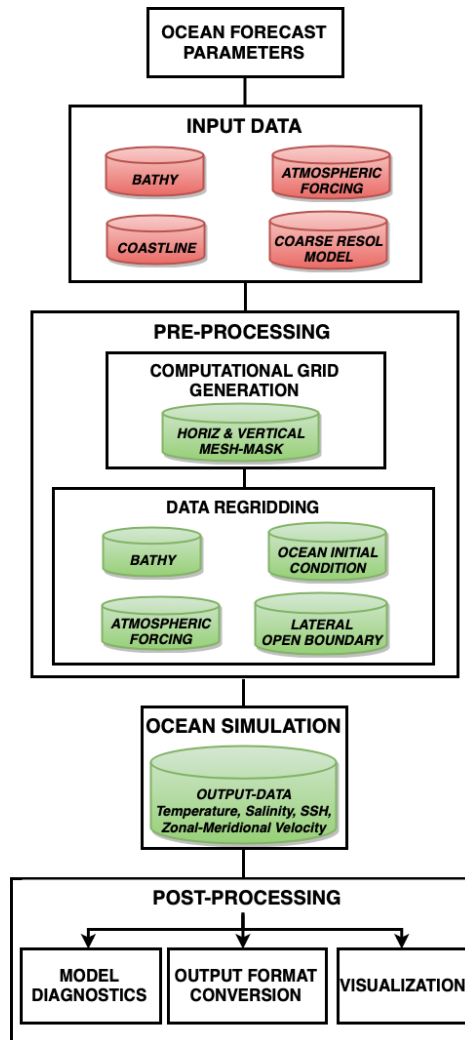displayed in the SURF virtual machine thanks to the post-processing tools
present.

Figure 2.2: SURF work-flow. Reproduced from Trotta et al. (2016).

2.2.2 Open boundary conditions

The problem of specifying the open boundary conditions for a limited area model has been found to be ill-posed[10] for the primitive equations (Oliger et al., 1978). Therefore, the adoption of a specific open boundary condition can strongly affect the local solution.

Sometimes errors due to this ill-posedness may be negligible for the flow space and time scales of interest: in this case, the boundary conditions chosen may be considered acceptable from a practical point of view. However, usually, problems related to the specification of the open boundary conditions are not viable: boundary conditions may generate or reflect waves that propagate inside the domain, or they may not effectively transmit information into the interior, or allow information to exit (Oddo and Pinardi, 2008). Perturbations that remain trapped within the domain lead to unrealistic recirculations near the lateral open boundaries, which typically occur in areas where the regional model has large outflow in contrast to the weaker outflow, or even inflow, predicted by the large scale system (Katavouta and Thompson, 2016).

Furthermore, internally generated variability in the regional model may lead to decoupling of the regional model solution from the large scale fields used to drive it. This inconsistency may generate numerical instability and/or the insurgence of numerical noise in the interior area close to the boundary (Oddo and Pinardi, 2008).

2.2.2.1 Flather scheme

The Flather condition was derived by Flather in 1976 for two-dimensional barotropic flows. It prescribes a relationship between sea surface elevation and currents taking into account mass conservation. We derive this condition as in Oddo and Pinardi (2008).

Let $\mathbf{U}_{BT}$ be the horizontal barotropic flow field, $\mathbf{U}_{BT} = \frac{1}{H+\eta} \int_{-H}^{\eta} (u,v)dz$; integrating the mass conservation equation 2.3 between $-H$ and η, considering that the integral limits η and $-H$ depend on the horizontal coordinates, inserting equation 2.11 and equation 2.7 (neglecting E and P), we obtain:

$$\frac{\partial \eta}{\partial t} + \nabla \cdot [(H+\eta)\mathbf{U}_{BT}] = 0 \qquad (2.18)$$

---

[10]A PDE is called well-posed (in the sense of Hadamard), if a solution exists, the solution is unique and it is stable, i.e. it depends continuously on the input data (initial conditions, boundary conditions, right hand side) (MIT OpenCourseWare). Well-posedness does not give any information about the solution accuracy (Blayo and Debreu, 2006).

Problems that are not well-posed are called ill-posed.

If both the nested and nesting models separately obey eq. 2.18, i.e. conserve mass, the two mass conservation equations can be equated:

$$\frac{\partial \eta_c}{\partial t} + \nabla \cdot [(H_c + \eta_c)\mathbf{U}_{BTc}] = \frac{\partial \eta_f}{\partial t} + \nabla \cdot [(H_f + \eta_f)\mathbf{U}_{BTf}] \qquad (2.19)$$

where the subscript c indicates the *c*oarse resolution parent model and f the *f*iner resolution child.

Surface elevation tendency $\frac{\partial \eta}{\partial t}$ can be expressed with a two-dimensional (normal and tangential to the boundary) Sommerfield radiation equation, which means assuming that the solution for η propagates through the open boundary in a wave-like form:

$$\frac{\partial \eta}{\partial t} = -\nabla \cdot (\mathbf{C}\eta) \qquad (2.20)$$

where $\mathbf{C} = (C_{normal}, C_{tangential})$ is the phase speed of the waves.
Inserting 2.20 into 2.19, we obtain:

$$\nabla \cdot [(H_c + \eta_c)\mathbf{U}_{BTc} - \mathbf{C}_c\eta_c] = \nabla \cdot [(H_f + \eta_f)\mathbf{U}_{BTf} - \mathbf{C}_f\eta_f] \qquad (2.21)$$

Assuming that the child and parent model have the same wave phase speed, from eq. 2.21 we obtain the generalised Flather's boundary condition for the normal to the boundary barotropic velocity component $\mathbf{U}_{BT}^n$:

$$\mathbf{U}_{BTf}^n = \frac{H_c + \eta_c}{H_f + \eta_f}\mathbf{U}_{BTc}^n - \frac{C^n}{H_f + \eta_f}(\eta_c - \eta_f) \qquad (2.22)$$

where C^n is the normal component of the wave phase speed.
If $C^n = \sqrt{gH}$, the linearized free gravity wave speed, $H_c = H_f = H$ and $|\eta| \ll H$, eq. 2.22 becomes:

$$\mathbf{U}_{BTf}^n = \mathbf{U}_{BTc}^n - \frac{\sqrt{gH}}{H}(\eta_c - \eta_f) \qquad (2.23)$$

the Flather lateral boundary condition equation.
In SURF, we use eq. 2.23 for barotropic velocities.

2.2.2.2 Relaxation scheme

The Flow relaxation scheme, as described in Oddo and Pinardi (2008) and Blayo and Debreu (2006), consists of driving the model solutions towards some reference external data (observations or a larger domain model results) on or in the vicinity of the boundary.

The simplest type of relaxation condition is the Dirichlet boundary condition: it consist of applying $\phi = \phi_{ext}$, where ϕ is a model variable, on the open boundary. The ϕ_{ext} values are obtained interpolating the large scale model

solutions to the child model spatial grid and temporal steps. However, using this condition, the incoming and outgoing information is totally determined by the reference data, regardless of the nested model results: part of the outgoing information, possibly inconsistent with the external data, may be reflected back into the domain (see beginning of section 2.2.2).

In order to solve this problem, the relaxation to reference values is made space and time dependent and extended to a portion of the domain adjacent to the open boundary, often called *nudging layer*. This is done by adding a *nudging term* to the original model equation, $\frac{\partial \phi}{\partial t} + F(\phi) = 0$, that becomes:

$$\frac{\partial \phi}{\partial t} + F(\phi) + \lambda(\phi - \phi_{ext}) = 0 \qquad (2.24)$$

λ is a function of position, normally decreasing towards the interior of the nested domain, defining the amplitude of the nudging layer. In this way, it imposes the relaxation time scale to be fast next to the boundary and increasingly slow proportionally to the distance from the boundary. This can be shown integrating a simplified model equation, $\frac{\partial \phi}{\partial t} + \lambda(\phi - \phi_{ext}) = 0$, from $t = 0$ to $t = \widetilde{t}$:

$$\int_{\phi(t=0)}^{\phi(\widetilde{t})} \frac{1}{\phi - \phi_{ext}} d\phi = -\int_0^{\widetilde{t}} \lambda dt$$

The solution is:

$$\phi(\widetilde{t}) = \phi_{ext} + (\phi(0) - \phi_{ext})e^{-\lambda \widetilde{t}} \qquad (2.25)$$

where λ evidently defines the relaxation time scale $\tau = \frac{1}{\lambda}$. λ could also be expressed, more explicitly, as $\lambda(lat, lon) = \frac{f(lat,lon)}{\tau_{reference}}$. When $\widetilde{t} \longrightarrow +\infty$, equation 2.25 gives $lim_{\widetilde{t} \to +\infty} \phi(\widetilde{t}) = \phi_{ext}$.

In the discretised equations, the nested model solution $\phi(d)$ is replaced at each time-step by

$$\phi(d) + \alpha(d)(\phi_{ext}(d) - \phi(d)) \quad d = 1, N \qquad (2.26)$$

where d gives the discrete distance from the model boundary and α is a relaxation function that depends on λ, the time discretization scheme and the time-step, increasing from 0 in the interior domain $(d \geq N + 1)$ to 1 at the boundary $(d = 1)$.

In the NEMO code, and then in SURF, α is specified as following:

$$\alpha(d) = 1 - tanh\left(\frac{d-1}{2}\right) \quad d = 1, N ; \qquad (2.27)$$

the relaxation time scale τ can be calculated from α with this formula (Δt is the model time-step):

$$\tau(d) = \frac{1 - \alpha(d)}{\alpha(d)} \Delta t \quad d = 1, N ; \qquad (2.28)$$

the width of the nudging layer N is given by the namelist parameter *nn_rimwidth*.

The Flow relaxation scheme generally appears to be one of the best methods in comparative numerical studies (e.g. Roed et al. (1987); Palma et al. (1998); Nycander et al. (2003)).

We apply the relaxation condition to baroclinic velocities, temperature and salinity fields, providing external data along straight open boundary lines. The nudging layer width can vary between one internal grid point and several. Often the reference variables are given by time-averaged fields (see chapter 3), making the use of a wide nudging layer even more important: in a time-averaged field all the processes with a frequency higher than the time window used for computing the mean are filtered out, so that the discrepancy between the scales resolved by the nested model and the scales represented by the external data is amplified and also are the possible inconsistencies.

2.2.3   Spin-up time

The spin-up time is defined as the time necessary for the nested model to reach a steady state value of the volume averaged kinetic energy, disentangling from the nesting model one over the same area (Simoncelli et al., 2011). Indeed, after initialization from the interpolation of the coarser model fields, limited area models have to dynamically adjust these fields, developing the new dynamical structures allowed by the higher resolution, the new fields having generally greater energy content than the parent model ones.

The typical spin-up time is a few days, i.e. the regional modelling must begin a few days before the forecast period. However, it is normally tuned for every specific case, resulting from the balance of different requirements: first, providing realistic initial flow fields, given e.g. that Trotta et al. (2016) found the difference of predicted fields from observational data decreasing with an increasing number of spin-up days; second, considering that boundary condition errors propagate at a finite speed, increasingly influencing the nested model fields as the simulation proceeds; third, if we want to provide a forecast, we have to establish a reasonable level of confidence to avoid a computationally too expensive number of spin-up days before the real forecast is made.

2.2.4   Why using this tool to analyse fjords climate importance

Future warming of the Greenland region and the subsequent glacier retreat are indissolubly linked to long-term changes in oceanic heat uptake, storage and transport: the boundary layer millimetre scale at ice-ocean interface is linked

to the 1000 km basin-wide scale of the North Atlantic. Hence, if we aim at simulating GrIS long term trends and their feedbacks on climate, we have to build ocean models able to cover an extremely wide range of scales, roughly seven orders, and to represent different dynamics and physical problems (Straneo et al., 2013). This is currently faced using plenty of parametrisations of sub-grid scale physics (see e.g. section 1.5.1), which are often poorly constrained by observations, in order to fulfil the lack of models directly able to answer these demands. The use a multi-nest procedure is a step towards and a clever strategy to encompass distinct scales and physics without having to build large scale models with resolutions that cannot be practically achieved.

Furthermore, the importance of improving the resolution with which fjord scale or smaller scale processes are being represented is highlighted by the different response patterns shown by eddy-permitting models compared with that presented by coarser resolution models (Straneo et al., 2013): it is necessary to resolve the first baroclinic Rossby radius of deformation (about 7 km on the shelf adjacent to the fjord, see third footnote of section 2.1) to correctly simulate the exchange processes between the boundary currents and the interior that occur through mesoscale eddies (Gelderloos et al., 2011).

Finally, the strong fjord-shelf coupling (intermediary circulation, section 1.5.5) makes downscaling a necessity to properly represent this interaction (see beginning of section 2.2). Hence, it also makes the choice of proper boundary conditions for a nested limited area fjord model of extreme importance for a realistic representation of its dynamics.

2.3 Experimental set-up

2.3.1 Spatial domain

In order to study Sermilik fjord circulation we set up a double nested simulation of ocean dynamics using SURF environment (see section 2.2).

The first nested model (or first nesting or NEST 1 in the following) covers the region between 41.7°W and 36.4°W, 64°N and 66.5°N (first and last T-grid points, see section 2.1.1.2), encompassing part of the shelf area outside Sermilik, with a resolution of 1/48°.

This resolution, expressed in degrees, can be transformed in meters units through the following relations:

$$\Delta x = R_e \ \Delta \phi \ cos\theta_0 \ \frac{\pi}{180} \tag{2.29}$$

$$\Delta y = R_e \ \Delta \theta \ \frac{\pi}{180} \tag{2.30}$$

where Δx and Δy are the longitude and latitude resolutions in meters, R_e the Earth radius ($\sim 6.371 \times 10^6$ m), $\Delta\phi$ and $\Delta\theta$ the longitude and latitude resolutions in degrees, θ_0 the latitude where Δx is computed.

A 1/48° resolution ($\Delta\phi, \Delta\theta = 1/48°$) corresponds to 2317 m in latitude and 1016 m in longitude at 64°N, 924 m at 66.5°N.

The second nested model (or second nesting or NEST 2 in the following) domain is defined between 38.5°W and 37°W, 65°N and 66.45°N (first and last T-grid points) with a 1/144° resolution: $\Delta y = 772$ m, $\Delta x = 326$ m at 65°N and $\Delta x = 309$ m at 66.45°N.

The coarse resolution parent model is the global model GOFS16 (1/16° resolution, see section 2.1) with $\Delta y = 6950$ m, $\Delta x = 3047$ m at 64°N and $\Delta x = 2771$ m at 66.5°N.
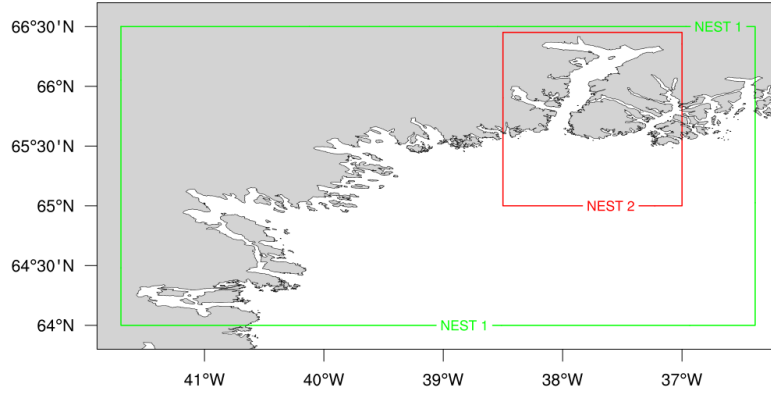
Figure 2.3: Representation of the nested domains limits.

2.3.2   Time period

We decided to run a simulation for a period of 10 months (EXP A - NEST 1 in table 2.10), so as to be able to analyse seasonal trends, compatibly with the computational resources available. The months selected are January-October 2017, since GOFS16 analysis are available only for this year.

This long simulation is compared with some shorter experiments, whose time periods are chosen in such a way that the study of both summer and winter seasons is allowed. The scientific question that each simulation is planned to answer determines the temporal coverage needed. However, the length of the various simulations is constrained also by the growth of the time necessary for computation with increasing open boundary conditions frequency (see paragraph 2.3.4) and with increasing temporal and spatial resolution. See table 2.10 for a detailed list of the time periods chosen.

2.3.3 Time-step

In order to prevent the generation of numerical instabilities, the time-step chosen for GOFS16 is $\Delta t^{GOFS16} = 200$ s. As long as the first nested model spatial resolution is three times greater than GOFS16 resolution, we had to set a time-step $\Delta t^{NEST\ 1}$ of 60 s for NEST 1. The CFL criterion is thus satisfied also for this nested model: $60\ s < \frac{200\ s}{3}$, therefore, if the propagation velocity $\mathbf{c}$ is the same, $\Delta t^{NEST\ 1} \cdot \sum_{i=1}^{3} \frac{c_i}{\Delta x_i^{NEST\ 1}} < \Delta t^{GOFS16} \cdot \sum_{i=1}^{3} \frac{c_i}{\Delta x_i^{GOFS16}} \leq 1$, where i indicates the spatial dimension.

For the second nested model, given the further increase in resolution (1/144°), we had to set a time-step of 24 s. The considerable computational resources required to run a model with such a fine spatial and temporal resolution prevents us from running the second nested simulations for periods longer than few weeks; nonetheless the covered time periods are still sufficient to show the differences and improvements in the dynamical outputs produced by the increase in resolution (see chapter 4).

nn_baro is chosen to be 60 for the first nesting and 24 for the second, so that the barotropic time-step is 1 s for both the nestings (see section 2.2.1.2).

2.3.4 Open boundaries

At the first nested model open boundaries, the external fields are provided by the daily GOFS16 outputs[11] (EXP B - NEST 1, C - NEST 1 and BW in table 2.10) or by the monthly means of the same fields (EXP A, AWJULY and AWJAN).

The use of monthly averaged open boundaries datasets allows us to study the fjord response to shelf forcing on a seasonal time scale, since the temporal averaging acts as a low pass filter that selects the open boundary conditions dynamics with frequency lower than a monthly one. Moreover, the monthly open boundaries permit to show to witch extent fjord dynamics can be reproduced starting from the outputs of an up-to-date climate model, which typically have a monthly frequency.

Regarding, instead, the second nested simulations, their variables are relaxed towards the correspondent first nested simulations output fields (which are given by hourly averages of the fields produced at every time-step), so as to capture the most of the temporal variability.

The nudging layer width is chosen to be 10 grid points for both the first and the second nested models. The nudging layer is thus thin enough not to reach

---

[11]Daily averages of the fields produced at every time-step.

our region of interest, the fjord (see figure 2.4), confining the relaxation to an area where we don't need to have new forecasting skills (i.e. solve predictive equations). On the other hand, a wide nudging layer is especially required for the monthly forced first nested simulations, since they experience a huge jump between the time scales that they resolve and the ones resolved by the time-averaged external data (see section 2.2.2.2).
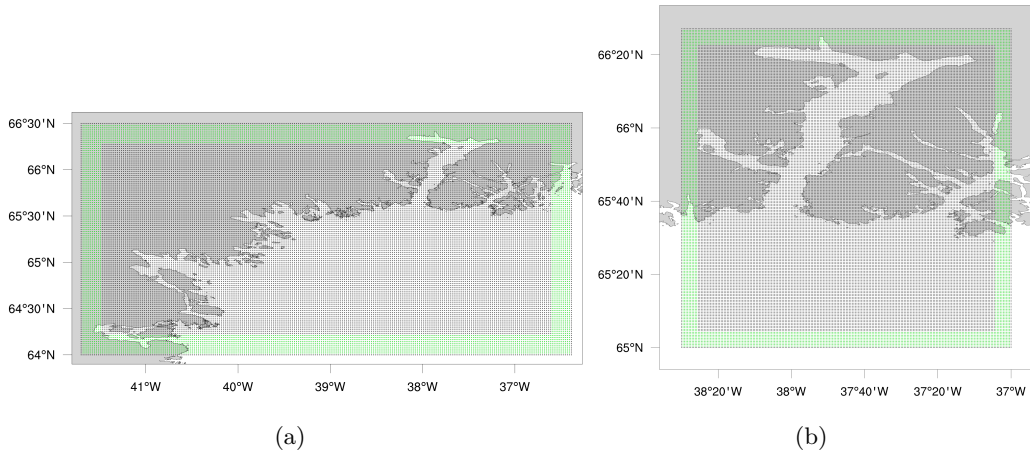

(a)   (b)

Figure 2.4: Width of the nudging layer for the two nested models (the first in fig. 2.4(a), the second in fig. 2.4(b)). The green grid points (T-grid) are those being part of the nudging layer, excluding all the green points corresponding to a closed boundary and those on land.

The relaxation time scale τ is given by equations 2.27 and 2.28, inserting the values of the two nestings time-steps (60 s and 24 s): at the tenth grid point from the boundary ($N = 10$ in equation 2.27) τ is equal to 2.81 days for the first nested model and to 27 hours for the second. Hence, a nudging layer of 10 grid points is sufficiently wide: the child models solutions at ten grid points from the boundary can follow the internal dynamics enough to be stable, not being too constricted to the external data, reducing then the reflection of outgoing information and the presence of inconsistencies (see section 2.2.2).
The tenth grid point corresponds roughly to a distance of 23 km from the southern boundary and 10 km from the eastern and western boundaries for the first nesting and respectively of 7.7 km and 3.3 km for the second nesting.

2.3.5   Initial conditions

The initial conditions for EXP A - NEST 1 (see table 2.10) are given by the GOFS16 daily outputs of the first day of simulation (1st January 2017), interpolated/extrapolated to the first nested model grid (see section 2.2.1.5) and

modified with a vertical extrapolation under 500 m depth (temperature, salinity, meridional and zonal velocity are set to their value at 500 m depth along the entire water column below). This is done in order to avoid the sea-over-land extrapolation of open ocean fields into the fjord (see paragraph 2.3.7 for further explanation).

The other simulations starting later than EXP A are, instead, initialised using the EXP A last instantaneous (produced at every time-step) fields of the day previous to the starting of the considered simulation. This means that they are a prosecution of A simulation, but with different forcings or different open boundaries conditions (see table 2.10). This trick was introduced in order to reduce the spin-up time required before the starting of the second nested simulations: the starting time of each second nesting must be delayed by at least some days (the spin-up time) with respect to the starting of the first nesting used to force it, in order to make the first nested model dynamics adapt to the new resolution before the second nested simulation begins (see section 2.2.3). The initial condition previously described reduces the spin-up time, because it contains dynamics already developed at the first nesting resolution rather than fields generated through an interpolation from a coarser grid to the fine grid considered (as would happen starting from GOFS16 outputs).

The second nestings are initialised with the first hourly output of the correspondent first nesting on the first day of the second nested simulation, which is analogous to the initial condition used for EXP A - NEST 1 (apart from the vertical extrapolation).

2.3.6   Diffusivity and viscosity coefficients

Lateral sub-grid scale mixing for momentum and tracers is parametrised through the Laplacian operator for both the first and the second nested models. This allows us to follow the results of Wallcraft et al. (2005).

As far as EXP A is concerned, the length of the simulation, 10 months, forces us to choose high values of the horizontal eddy viscosity and diffusivity coefficients, $50 \frac{m^2}{s}$, with respect to the value suggested in Wallcraft et al. (2005): this guarantees the model to be particularly stable, despite the simulation length, avoiding the numerical instabilities that develop with smaller eddy coefficients. We use the same eddy viscosity and diffusivity coefficients even for the other shorter first nested simulations in order to be able to compare the results.

Regarding the temporally shorter second nested simulations, instead, we could choose the two coefficients to be equal to $6 \frac{m^2}{s}$ without the generation of instabilities. This choice follows the quadratic relation between resolution and

eddy viscosity found by Wallcraft et al. (2005): according to this article, if a_0 is the parent eddy viscosity, the child correspondent coefficient should be $a = a_0 \left(\frac{\Delta x_F}{\Delta x_L} \right)^2$, where Δx_F and Δx_L are respectively the fine and large scale model grid spacings. In our case, $a_{NEST\ 2} = a_{NEST\ 1} \cdot \left(\frac{48}{144} \right)^2 = \frac{50}{9} \frac{m^2}{s} \approx 6 \frac{m^2}{s}$.

2.3.7 Bathymetry

To run GOFS16 parent model, a bathymetry obtained combining three distinct topographic products is used: ETOPO2 (U.S. Department of Commerce, 2006) for the deep ocean, GEBCO (General Bathymetric Chart of the Oceans, IOC, IHO and BODC (2003)) for the continental shelves shallower than 300 m, and Bedmap2 (Fretwell P. et al., 2013) for the Antarctic region, south of 60° S. The result is modified by two passes of a uniform Shapiro filter[12] and partial step parametrization (see section 2.2.1.1) is adopted. The maximum depth allowed is 6000 m and the minimum depth is set to 10 m (Iovino et al., 2016).

Unfortunately, GEBCO poorly resolves Sermilik fjord bathymetry: in this dataset, the fjord reaches a maximum depth of 35 m (see figure 2.5(a)), while in reality it extends to $\sim$ 900 m (see section 1.6). EXP A - NEST 1 initial conditions must then be set with the sea-over-land procedure (see section 2.2.1.5). However, being the shelf region in GEBCO shallower than the real fjord depth (and shallower than the fjord depth in the bathymetry used for SURF), the fjord ocean fields below a certain depth (that is approximately 500 m) would be extrapolated from a region out (or nearly out) the shelf, characterised by a completely different dynamics. To avoid this, we decided to vertically extrapolate the fjord initial condition fields (temperature, salinity, zonal and meridional velocity) below 500 m, setting them to their value at this depth along the entire water column below. To avoid discontinuities in the initial condition, vertical extrapolation is performed over a region chosen so as to have borders as much as possible shallower than 500 m in SURF first nested model bathymetry (and to include all Sermilik fjord, see figure 2.5(c)).

For SURF child models we use the higher resolution (150 m × 150 m) dataset IceBridge BedMachine Greenland, Version 3 (Morlighem et al. (2017), see figure 2.6 and figure 2.5(b)), which contains a bathymetric map of all Greenland obtained by combining sparse radar bathymetry measurements with

---

[12]Shapiro filter is a high order linear spatial filter implemented through a diffusive term that is applied separately to a variable each N time-steps. It is usually used to remove gridpoint-scale noise without affecting the physical structures of a field (Trotta et al., 2017). Here it is employed to smooth the bathymetry in order to prevent the generation of numerical errors as a consequence of too steep gradients that could be present in bottom topography.
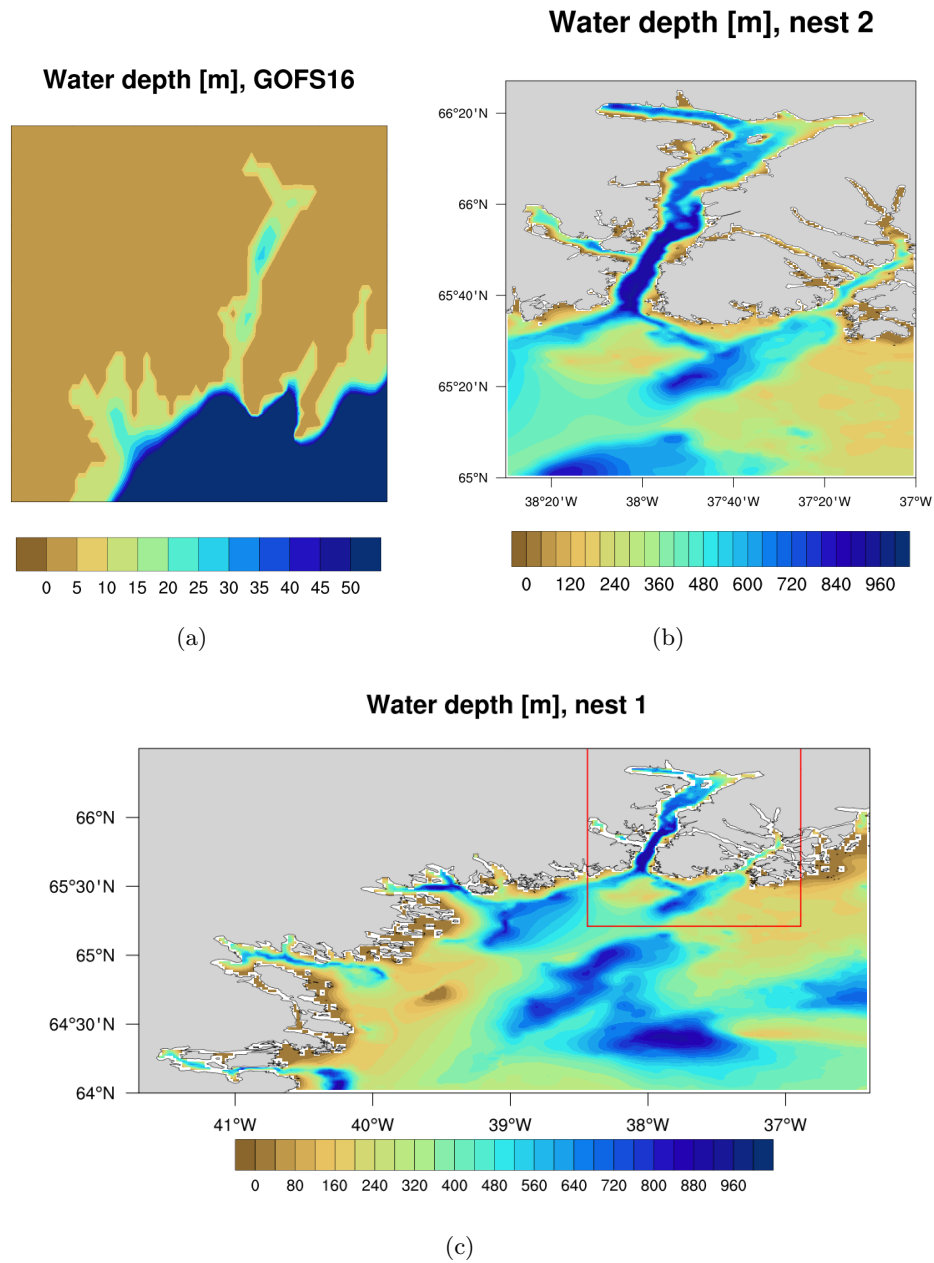
Water depth [m], nest 2

Water depth [m], GOFS16

(a)

(b)

Water depth [m], nest 1

(c)

Figure 2.5: 2.5(a): GEBCO bathymetry interpolated to GOFS16 irregular grid. The maximum fjord depth is 35 m.

2.5(b): BedMachine bathymetry interpolated to NEST 2 grid.

2.5(c): BedMachine bathymetry interpolated to NEST 1 grid. The red polygon limits the area in which vertical extrapolation of the initial condition fields is performed.
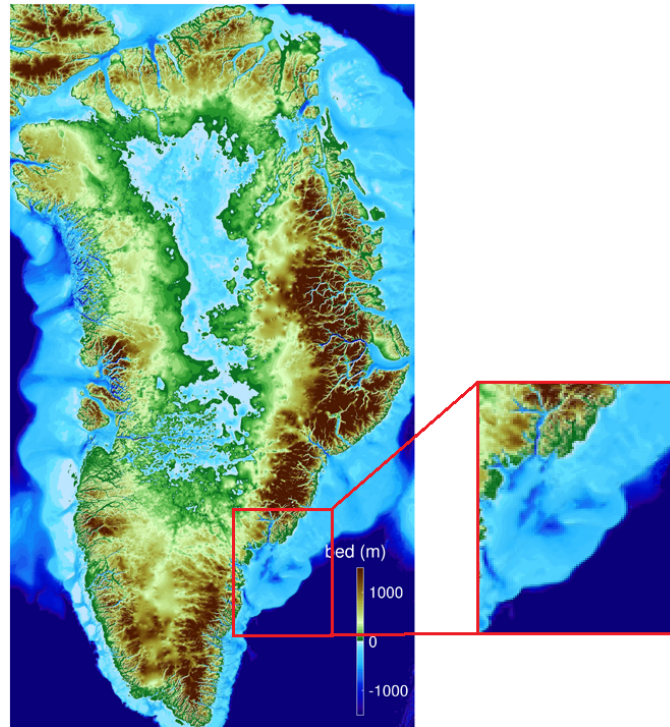
Figure 2.6: Greenland's bedrock topography from BedMachine dataset. Reproduced from Morlighem et al. (2017).

RTopo-2 dataset (Schaffer et al., 2016).

The fine resolution BedMachine dataset is interpolated to the coarser first and second nested models grids with a bilinear method. The resulting bathymetric maps are represented in figures 2.5(c) and 2.5(b). The minimum depth allowed is 5 m.

This dataset gives an accurate representation of Sermilik fjord bathymetry.

2.3.8   Atmospheric forcing

At the surface, both GOFS16 and SURF child models are forced with the 10 m-meridional and zonal wind velocity fields, the 2 m-air temperature field (with a temporal resolution of 6 hours), radiation fluxes and precipitation fluxes (with a temporal resolution of one day) from NCEP analysis (NCEP GFS, 2015). The spatial resolution is 1/4°.

2.3.9   Coastline

The coastline dataset used in SURF is NOAA GSHHG (Global Self-consistent, Hierarchical, High-resolution Geography Database) (Wessel and Smith, 1996).

2.3.10 Pycnocline depth

From now on, we will identify the pycnocline depth with the $1027 \frac{kg}{m^3}$ isopycnal, as done by Jackson et al. (2016). Actually, if we consider the time average over the entire EXP A (table 2.10) simulation of the hourly potential density profiles at point B in map 2.8 obtained from EXP A salinity and potential temperature outputs[13] (figure 2.7), emerges that the most appropriate isopycnal to identify the pycnocline with is the $1026.8 \frac{kg}{m^3}$ one. With a depth difference of $\sim 20\ m$, however, the $1027 \frac{kg}{m^3}$ isopycnal is still contained in the pycnocline and, thus, it's still a good proxy.
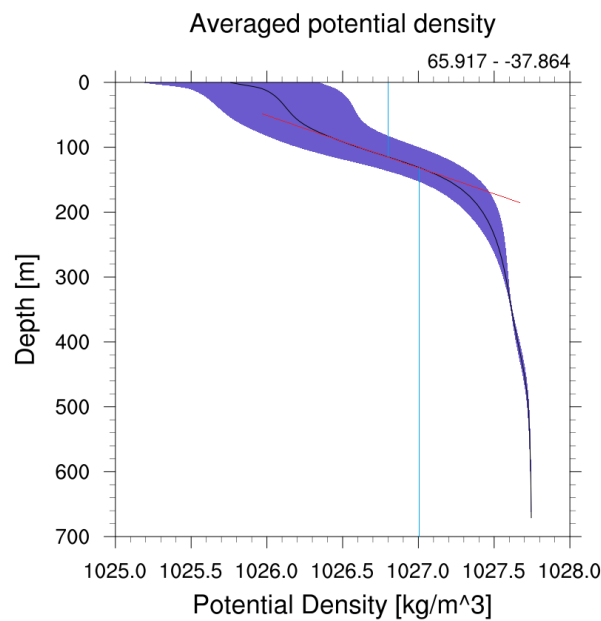
Figure 2.7: Time average of the hourly potential density profiles at point B in figure 2.8 obtained from the salinity and potential temperature outputs of the ten months simulation EXP A (table 2.10) with the Jackett and Mcdougall (1995) modified UNESCO equation of state formula. Error bars show one standard deviation of the hourly profiles with respect to the time averaged one.

Table 2.9 shows a summary of the simulations settings.

Table 2.10 shows a list of the simulations.

---

[13]Potential density is computed with the Jackett and Mcdougall (1995) modified UNESCO equation of state formula.
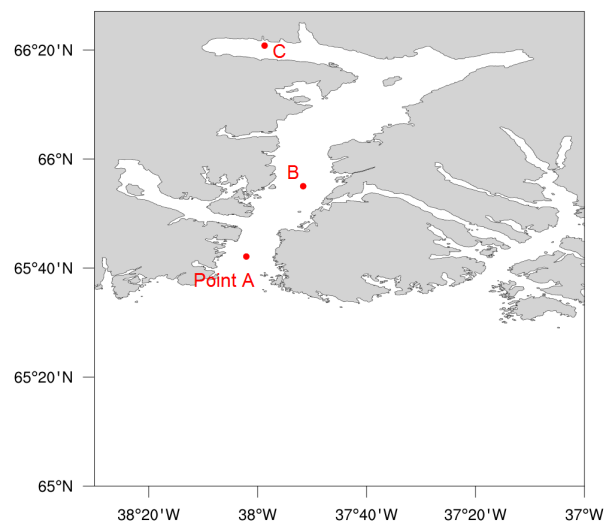
Figure 2.8: Locations at which fjord water properties will be represented (through e.g. some Hovmöller diagrams): point A (latitude: 65.703°N, longitude: 38.033°W), point B (65.917°N, 37.864°W), point C (66.344°N, 37.982°W).

		GOFS16	NEST 1	NEST 2
TIME STEP		200 s	60 s	24 s
SPATIAL GRID		*Horizontal Grid*		
		Curvilinear coordinate on the sphere (non-uniform tripolar grid)	Geographical mesh on the sphere with regular grid-spacing	
	N° of points *Grid resol.*	5762x3963 1/16° 3.0x6.9 km	256x121 1/48° 1.0x2.3 km	217X210 1/144° 0.326x0.772 km
		Vertical Grid		
		z-coordinate with partial step		
	N° of levels *Parameters* *Doubletanh*	98 h_{sur}= -4068.377 m, h_0=82.4 m, h_1=6.815951 m, h_{th}=30.35101, h_{cr}=12.0 True, h_2=75.0 m, h_{th2}=64.0, h_{cr2}=17.0	100 z_{max}=957.8 m, dz_{min}=0.6 m, h_{cr}=16.0, h_{th}=50.0 False	100 z_{max}=934.0 m, dz_{min}=0.6 m, h_{cr}=16.0, h_{th}=50.0 False
PHYSICS		*Horizontal Subgrid-scale physics*		
		Bilaplacian/laplacian operator	Laplacian operator	
	Viscos. coeff *Diffus. coeff*	-0.5e10 m⁴/s bilaplacian 80 m²/s laplacian	50 m²/s 50 m²/s	6 m²/s 6 m²/s
		Vertical Subgrid-scale physics		
		TKE mixing	Pacanowski-Philander mixing parametrization	
	EVD Mix coeff	10 m²/s	10 m²/s	10 m²/s
INITIAL CONDITION		-	Monthly means of GOFS16 fields or daily GOFS16 fields (T, S, u, v and SSH)	Hourly NEST 1 fields (T, S, u, v and SSH)
BOUNDARY CONDITION		*Surface BC*		
		CORE bulk formulae	CORE bulk formulae	
		Lateral close BC		
		Free-slip condition	No-slip condition	
		Lateral open BC		
		No	Flather scheme 10 grid points Flow relaxation scheme	
		Bottom BC		
		Non linear friction	Non linear friction	
SPECIFIC NUMERIC FORMUL.		*Moment Advection*		
		EEN scheme	EEN scheme	
		Tracer Advection		
		TVD scheme	MUSCL scheme	
SURFACE		Split-explicit linear free surface	Split-explicit linear free surface	
WATER INPUTS		Runoff	No rivers, no ice	
ATMOSP. FORCING		NCEP analysis every 6 hours (1/4°)	NCEP analysis every 6 hours (1/4°)	
BATHY.		GEBCO	BedMachine	

Figure 2.9: Summary of the simulation parameters.

		NEST 1	NEST 2	SCIENTIFIC QUESTION
EXP A	Period	1/1/2017 - 31/10/2017	-	Study seasonal fjord circulation
	N° days	304	-	
	Boundary cond.	monthly averaged GOFS16 fields	-	
	Initial cond.	1/1/2017 GOFS16 output	-	
EXP B	Period	15/1/2017 - 8/2/2017	17/1/2017 - 5/2/2017	Study intermediary circulation - focus on winter case
	N° days	25	20	
	Boundary cond.	daily GOFS16 outputs	hourly averaged EXP B - NEST 1 fields	
	Initial cond.	14/1/2017 last instantaneous fields of EXP A - NEST 1	17/1/2017 first hour averaged EXP B - NEST 1 fields	
EXP C	Period	2/7/2017 - 29/7/2017	5/7/2017 - 29/7/2017	Study intermediary circulation - focus on summer case
	N° days	28	25	
	Boundary cond.	daily GOFS16 outputs	hourly averaged EXP C - NEST 1 fields	
	Initial cond.	1/7/2017 last instantaneous fields of EXP A - NEST 1	5/7/2017 first hour averaged EXP C - NEST 1 fields	
EXP BW	Period	15/1/2017 - 8/2/2017	-	Investigate wind stress role in driving intermediary circulation
	N° days	25	-	
	Boundary cond.	daily GOFS16 outputs	-	
	Initial cond.	14/1/2017 last instantaneous fields of EXP A - NEST 1	-	
	Note	null wind stress		
EXP AWJULY	Period	1/7/2017 - 31/7/2017	-	Investigate wind stress role in driving the seasonal reversal and intermediary circulation
	N° days	31	-	
	Boundary cond.	monthly averaged GOFS16 fields	-	
	Initial cond.	30/6/2017 last instantaneous fields of EXP A - NEST 1	-	
	Note	null wind stress		
EXP AWJAN	Period	1/1/2017 − 8/2/2017	-	Investigate wind stress role in driving the seasonal reversal
	N° days	39	-	
	Boundary cond.	monthly averaged GOFS16 fields	-	
	Initial cond.	1/1/2017 GOFS16 output	-	
	Note	null wind stress		

Figure 2.10: List of the simulations performed.
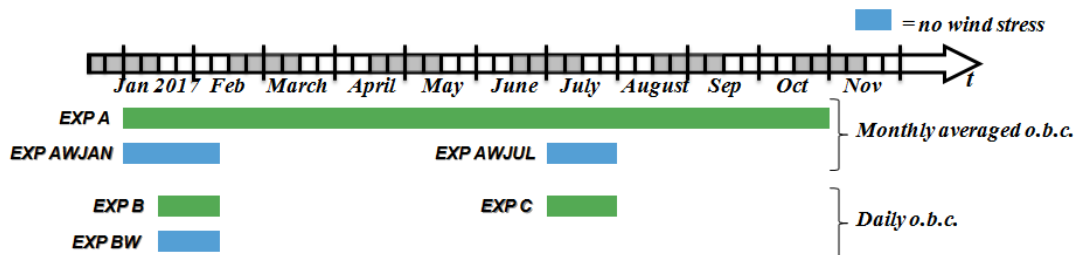
Figure 2.11: Visualization of the first nested simulations principal characteristics.

Sermilik fjord circulation analysis at seasonal time scale

3.1 Evidence of seasonal variability from observations

Seasonal fjord circulation changes are documented by the currents measured by Jackson et al. (2016): figure 3.1 represents the temporal running mean (with an averaging time scale of 25 days) of the along-fjord velocity measured at point B in map 2.8. The time scale of the running mean used in Jackson et al.
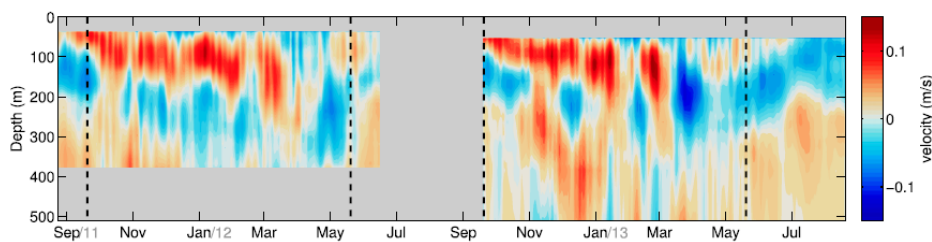

Figure 3.1: 25-day running mean of the along-fjord velocity measured with moorings at point B in figure 2.8. Velocity is positive when directed towards the head of the fjord; the black dashed lines separate the summer and non-summer seasons. Reproduced from Jackson et al. (2016).

(2016), 25 days, was chosen to isolate the mean from the current fluctuations due to the intermediary circulation (see section 1.7.2). This figure shows the
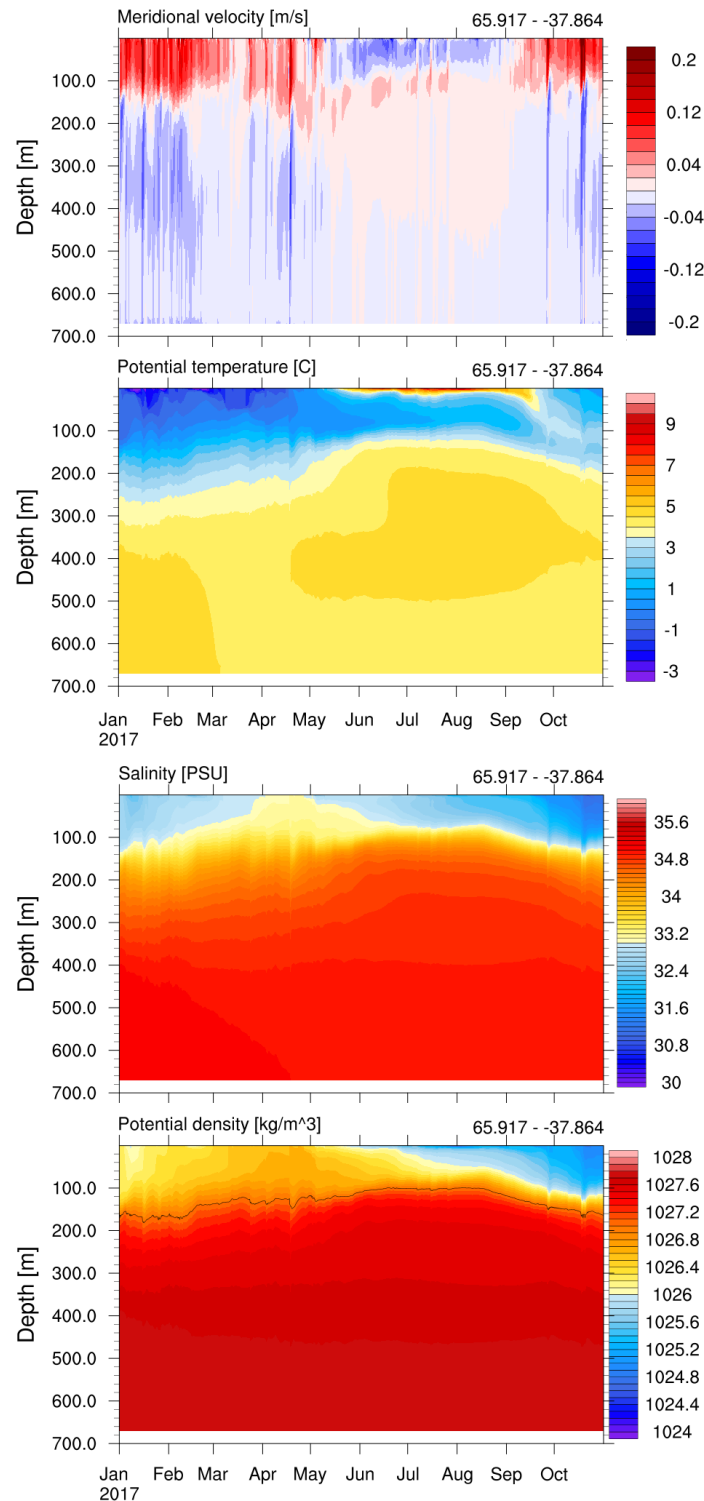
Figure 3.2: Meridional velocity, potential temperature, salinity and potential density obtained from EXP A - NEST 1 in table 2.10 at point B in figure 2.8. Meridional velocity is positive towards the north (entering the fjord); the black line superimposed on the potential density graph indicates the pycnocline depth, where the pycnocline is identified with the 1027 kg/m^3 isopycnal following Jackson et al. (2016).

presence of two different modes of circulation, one in summer (defined as the period between the 20th of May and the 19th of September) and the other in the non-summer season: while in summer a surface layer experiences an outflowing current and a deeper layer an inflowing one, in winter the surface layer shows an inflowing velocity and at major depth the current outflows.

3.2   Seasonal circulation from model results

The availability of a 10 months simulation (EXP A in table 2.10) allows to reconstruct the principal characteristics of Sermilik fjord circulation on a seasonal time scale.

Figure 3.2 represents meridional velocity[1], potential temperature, salinity and potential density resulting from the 10-month simulation at the same point at which the measurements in figure 3.1 were taken (point B in map 2.8). It is clear that the summer-winter circulation reversal observed in figure 3.1 is present and that the depth of the reversal coincides with the depth of the pycnocline for both the seasons. Thus, in the simulation, the two current directions correspond to two water layers, a cooler and fresher one at the surface and a saltier and warmer at greater depth. These two layers are the PW and AW layers described in section 1.3.

The measured along-fjord velocity is compared to the simulated meridional velocity in figure 3.3. Despite the evident correspondence between the summer and non-summer circulation modes, there are some differences: the depth of the summer reversal is clearly greater in the observations (approximately twice the simulated one); in winter the observed deep outflow is overall concentrated in a ~ 100 m thick layer, while deeper there is another inflow that is not present in the model output. Moreover, the observations show several episodes of surface (shallower than 80 m) outflow in winter, whereas, in the simulation, water only inflows till a depth greater than 100 m.

The match between modelled and observed data can be further analysed comparing figure 3.4(a) with figure 3.4(b). The first one is reproduced from

---

[1]Given that in NEMO the zonal and meridional velocities are defined on two staggered U and V grids (see section 2.1.1.2), the computation of the along-fjord and cross-fjord velocity components is not trivial. However, depending on the considered location, it is possible to approximate the along-fjord velocity with the meridional or zonal component alone. For example, at point B the zonal velocity is approximately one order of magnitude smaller than the meridional velocity; therefore, at this point, we have decided to neglect the correction to the meridional component that would be necessary to obtain the along-fjord current.
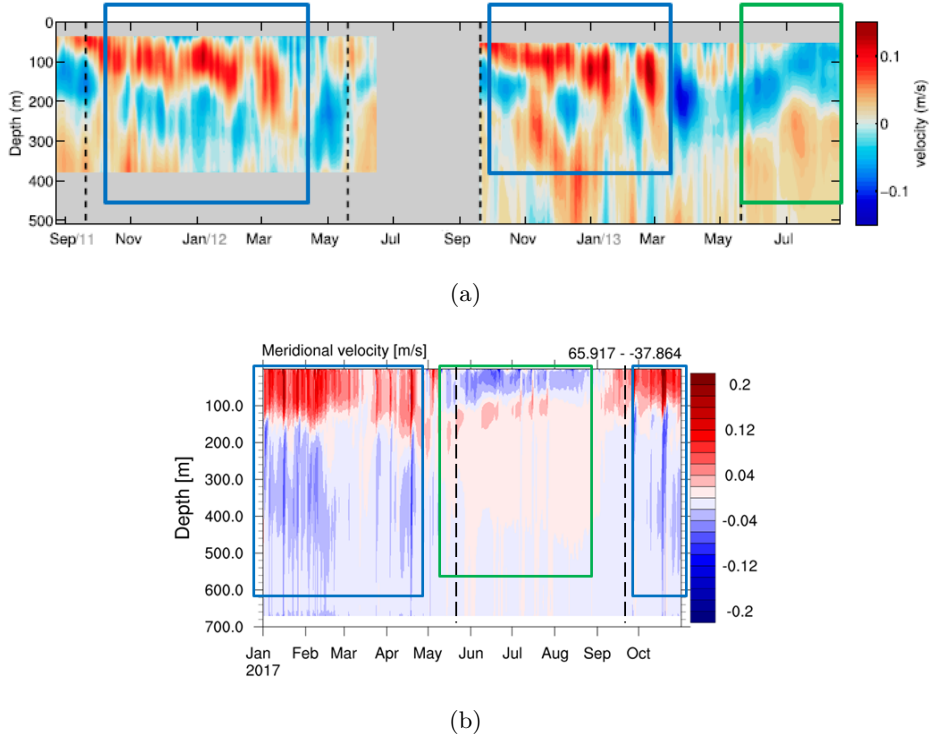
(a)

(b)

Figure 3.3: Comparison between figure 3.1 (3.3(a)) and meridional velocity in figure 3.2 (3.3(b)). The blue and green frames try to highlight the similarity between observed and modelled summer (green) and winter (blue) conditions; the black dashed lines separate the two seasons.

Jackson et al. (2016) and represents:

- the time mean over summer (20th May - 19th September) and non-summer periods of the filtered along-fjord velocity profiles represented in figure 3.1;

- the summer and non-summer time means of potential temperature (θ) and salinity (S) profiles measured at the same point (point B in figure 2.8) and modified by averaging with a 25-day running mean and then subtracting at each time and depth the average of the θ or S 25-day running mean over the cross-fjord section area.

Therefore, supposing that potential temperature and salinity are approximately constant along the cross-fjord direction, the fields whose summer and non-summer averages are depicted in figure 3.4(a) ($v_{rm}^{along-fjord}$, θ_{rm} and S_{rm}) are:

$$v_{rm}^{along-fjord}(z,t) = \overline{v_{m}^{along-fjord}(z,t)} \tag{3.1}$$

$$\theta_{rm}(z,t) = \overline{\theta_m(z,t)} - f_\theta(t) \qquad f_\theta(t) = \frac{1}{A} \int\limits_{-h}^{0} \overline{\theta_m(z,t)} W(z) dz \tag{3.2}$$

$$S_{rm}(z,t) = \overline{S_m(z,t)} - f_S(t) \qquad f_S(t) = \frac{1}{A}\int_{-h}^{0} \overline{S_m(z,t)}W(z)dz \qquad (3.3)$$

$$A = \int_{-h}^{0}\left[\int_{\partial\Lambda(z)} dl\right]dz \qquad W(z) = \int_{\partial\Lambda(z)} dl \qquad (3.4)$$

where $v_m^{along-fjord}$, θ_m and S_m are the fields measured at point B, l the coordinate in the cross-fjord direction, $W(z)$ is a line integral over the fjord width $\partial\Lambda$, h the water depth at point B and the overline indicates the 25-day running average. A is the cross-fjord section area above the point B water depth.

Figure 3.4(b), instead, depicts the summer and non-summer time averages of the modelled (EXP A - NEST 1 in table 2.10) meridional current (v), salinity (S) and potential temperature (θ) profiles at point B in map 2.8. The averages of potential temperature and salinity over a cross-fjord section intercepting point B are subtracted from the point B θ and S vertical profiles at each time-step and depth before averaging over summer and non-summer periods. Water properties are again supposed to be constant over the fjord width. Thus, the fields whose summer and non-summer averages are represented (v_{rs}, θ_{rs} and S_{rs}) are:

$$v_{rs}(z,t) = v_s(\widetilde{x},\widetilde{y},z,t) \qquad (3.5)$$

$$\theta_{rs}(z,t) = \theta_s(\widetilde{x},\widetilde{y},z,t) - f_\theta(t) \qquad f_\theta(t) = \frac{1}{A}\int_{-h}^{0}\theta_s(\widetilde{x},\widetilde{y},z,t)W(z)dz \qquad (3.6)$$

$$S_{rs}(z,t) = S_s(\widetilde{x},\widetilde{y},z,t) - f_S(t) \qquad f_S(t) = \frac{1}{A}\int_{-h}^{0}S_s(\widetilde{x},\widetilde{y},z,t)W(z)dz \qquad (3.7)$$

where v_s, θ_s and S_s are the outputs of EXP A simulation, $\widetilde{x}$ and $\widetilde{y}$ the longitude and latitude of point B. A and $W(z)$ are defined in equation 3.4.

The section averaged meridional velocity ($\frac{1}{A}\int_{-h}^{0} v_s(\widetilde{x},\widetilde{y},z,t)W(z)dz$) is neglected computing the simulated meridional current means[2] in figure 3.4(b), as are the section averages of the filtered along-fjord velocity ($\frac{1}{A}\int_{-h}^{0} \overline{v_m^{along-fjord}(z,t)}W(z)dz$) in the cited article.

---

[2]Computing the average meridional velocity over a cross-fjord section (approximately at mid-fjord) at each time step and comparing the result with the local current at each grid point corresponding to the same section, this last one appears to be at least one, but mostly two or three, orders of magnitude greater than the section average, depending on season and depth.
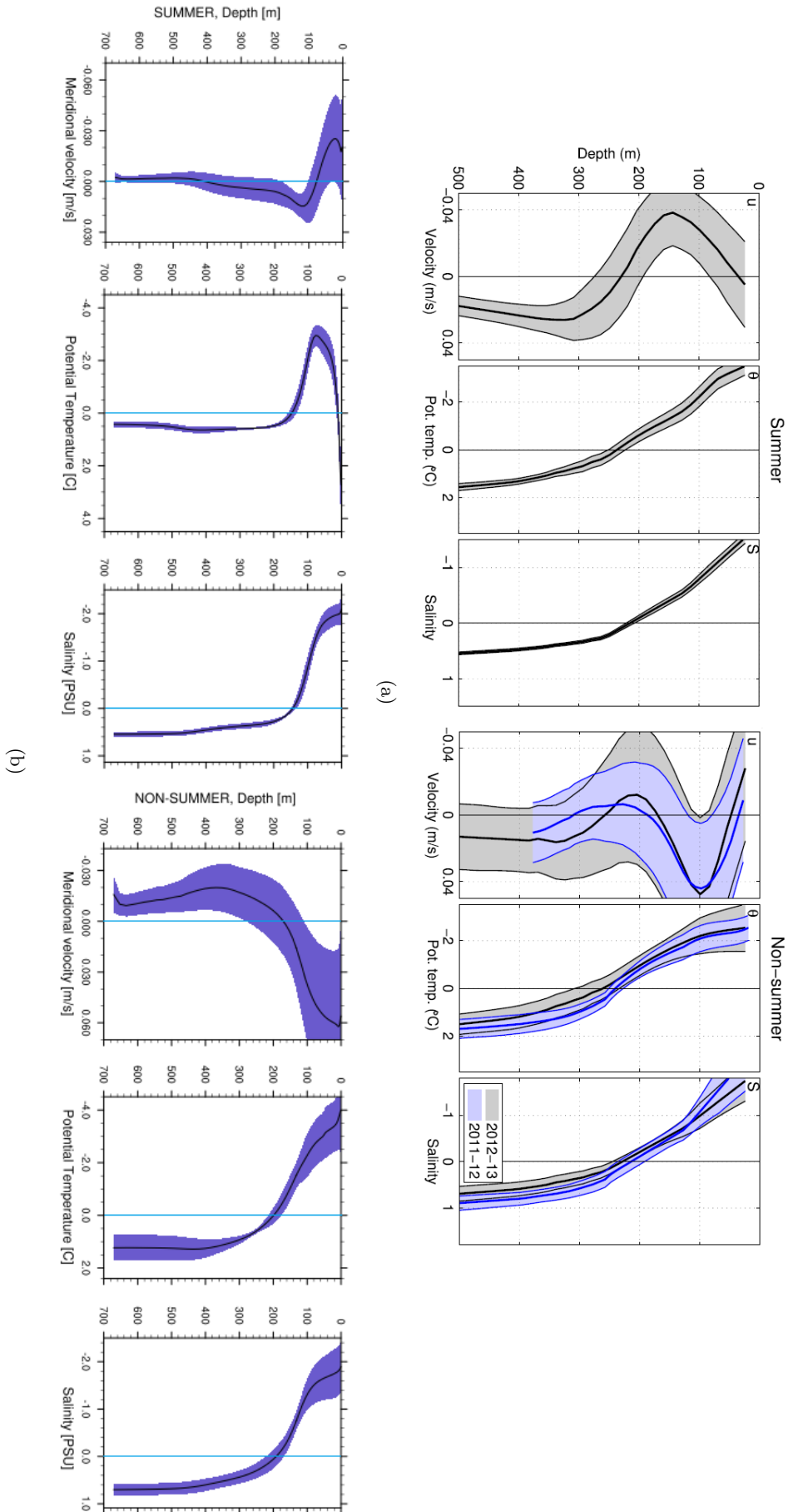
(a)

(b)

Figure 3.4: 3.4(a): Time means over summer (20th May - 19th September) and non-summer periods of

- the 25-day running time mean of the along-fjord velocity profiles measured with moorings at point B in figure 2.8;
- potential temperature and salinity profiles measured at the same point and modified by averaging with a 25-day running mean and then subtracting at each time and depth the average of the potential temperature or salinity 25-day running mean over the cross-fjord section area.

Error bars show one standard deviation of these fields (the ones whose summer and non-summer averages are computed, $v_{rm}^{along-fjord}$, θ_{rm} and S_{rm}) over the summer or non-summer period. Reproduced from Jackson et al. (2016).

3.4(b): Summer and non-summer time averages of the modelled (EXP A - NEST 1 in table 2.10) meridional current, salinity and potential temperature profiles at point B in figure 2.8. The averages of potential temperature and salinity over a cross-fjord section intercepting point B are subtracted from the potential temperature and salinity profiles at each time step and depth before averaging over summer and non-summer periods. Error bars show one standard deviation of these fields (the ones whose summer and non-summer averages are computed, v_{rs}, θ_{rs} and S_{rs}) over the summer or non-summer period.
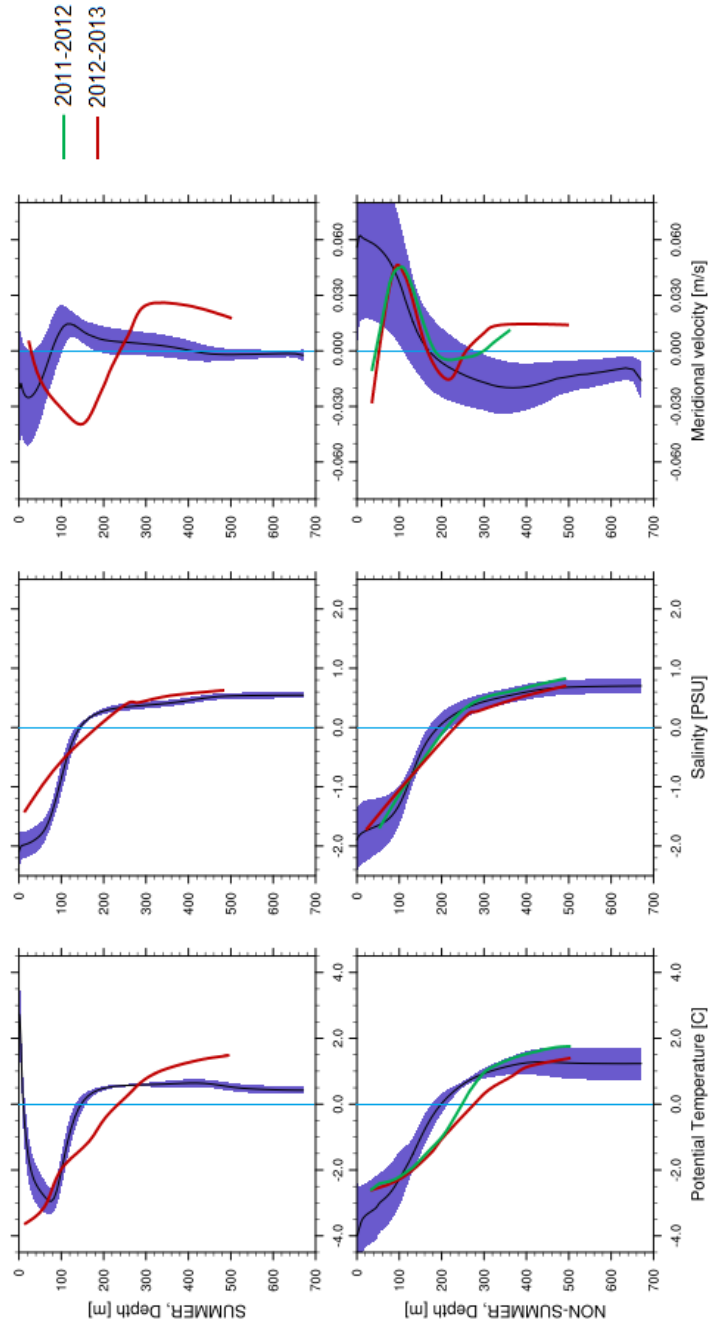
Figure 3.5: Comparison between figure 3.4(a) and figure 3.4(b). Figure 3.4(a) profiles are superimposed in red and green over figure 3.4(b) profiles.

The comparison of figures 3.4(a) and 3.4(b) facilitates the analysis of the differences between the filtered observed data and the model outputs that were already visible in the Hovmöller plots in figure 3.3.

Firstly, during the non-summer period, the current below 250 m is inflowing in the observations and outflowing according to the model; the non-summer reversal of the observed along-fjord velocity near 50 m depth is not present in the simulation. Moreover, during summer, the depth of the current reversal appears to be shallower in the simulation (~ 100 m) than in the observations (~ 200 m). Jackson and Straneo suggest that the non-summer surface outflowing layer present in the observational data could be due to outflows from the glaciers, thus being correctly absent in our simulation.

Analysing the salinity and temperature profiles, the thermoclines and the haloclines turn out to be sharper in the model than in the observations for both the seasons, maybe partially as a consequence of the time averaging of the observations starting from a signal containing huge pycnocline depth fluctuations that are not present in EXP A, especially in winter (see chapter 4 and figure 1.9). The major deviations with respect to data are observed in summer: this is probably due to the absence of the glaciers in our nested model, whose impact on water properties is greater in summer than in winter (see section 1.7.1).

The summer simulated potential temperature average shows one of the advantages of dealing with a model and not with sparse measurements: the placement of the observing instruments doesn't allow to capture the considerable warming of a ~ 20 m thick surface layer in this season, which is, instead, produced by the simulation.

Despite the differences in thermocline and halocline sharpness and number of winter reversals, the averaged profiles and the Hovmöller plots from the simulation outputs and from the observational data appear to share the basic characteristics. This proves that the choice of monthly averaged open boundary conditions for EXP A (see table 2.10) is effective in selecting low frequency modes of fjord circulation. Indeed, through the monthly averaging, the parent model dynamics entering our first nested domain is chosen and filtered so as to retain only phenomena that happen with a frequency lower than a monthly one: this low pass filter acting at the open boundaries is, at least in part, able to modify the interior dynamics retaining only the slow modes of fjord circulation.

This saves us from having to separate coexisting modes of circulation, avoiding all the problems deriving from the likely presence of interactions between the different time-scale modes, and it gives us greater control over the circulation

drivers[3].

Jackson and Straneo attribute the summer and non-summer current patterns present in the 25-day running mean of the measured along-fjord velocity to a buoyancy driven estuarine circulation in summer (see section 1.7.3) and to sampling biases in winter. Since ice is not present in our nested model, the simulated summer pattern cannot be explained as glacier-driven circulation. Thus, the summer current pattern shown by the filtered observational data might be a superposition of a glacier-driven flow to another component that must be independent from the presence of the glaciers (the one produced by our model). Nonetheless, some further investigation is needed, especially considering the different depth of the summer reversal in data or model, which may be due to the superposition and interaction between these two components in the observations.

Jackson and Straneo explain the observed non-summer inflowing at ~ 100 m depth as a result of the moorings being located slightly off-centre the fjord, on the eastern side: this should lead to the detection of a mean inflowing velocity in the depth range of pycnocline excursions (as a consequence of the cross-fjord pycnocline tilt, see appendix B in Jackson et al. (2016) and section 1.7.2). Actually, the inflow is located at shallower depth than the pycnocline (both in the simulation and in data) and the model clearly shows that it involves the entire width of the fjord (see figure 3.9). Thus, the observed ~ 100 m deep inflow and the ~ 200 m deep outflow may not be due to sampling biases but they may be part of a seasonal circulation mode. It is yet to be explained why the averaged observations show inflowing velocity under $\sim 250 - 300$ m depth while the model produces an outflowing current.

3.3 Seasonal circulation drivers

What is, then, the driver of the seasonal reversal produced in our simulation?

Firstly, the reversal could be attributed to the local wind forcing. Figure 3.6 compares the meridional velocity at point B obtained from EXP A, from EXP AWJAN and from EXP AWJUL. These two last simulations cover respectively January (and the beginning of February) and July, with exactly the same settings of EXP A but with the wind stress imposed to be null over the entire domain. The different summer and non-summer current patterns
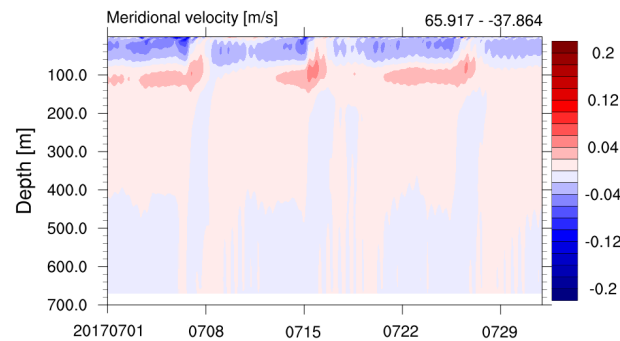
---

[3]Actually, instead of eliminating intermediary circulation through the application of a temporal running average to the nested model outputs, we directly remove its forcing from the nested model: see chapter 4.
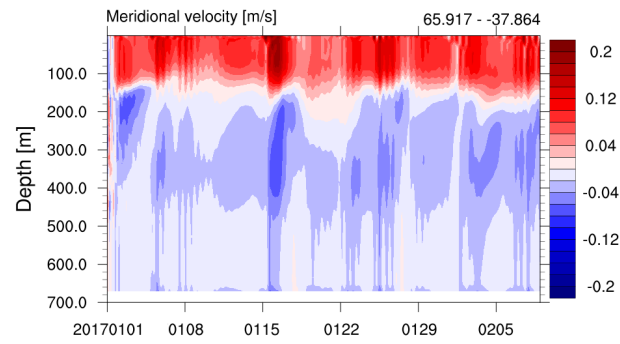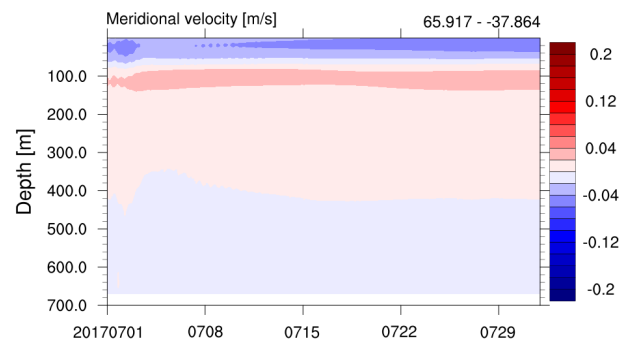
(a)
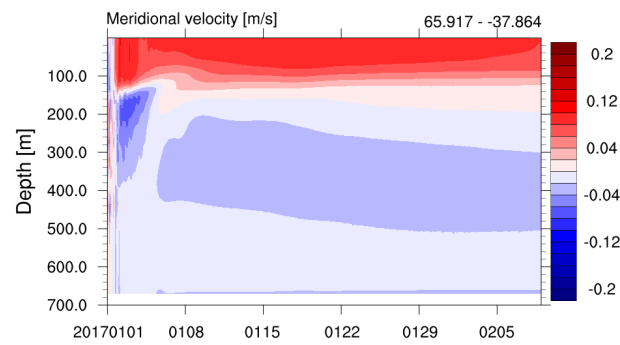
(b)

(c)

(d)

Figure 3.6: Meridional velocity obtained at point B in figure 2.8 from EXP A (3.6(a) - from 1 January to 8 February - and 3.6(c) - from 1 July to 31 July), EXP AWJAN (3.6(b)) and EXP AWJULY (3.6(d)) in table 2.10. Meridional velocity is positive northward.

are clearly still present (although the current intensity variability almost disappears), demonstrating that the local wind stress is not the source of the seasonal reversal.

Since ice is not included in the model and local wind is not the searched driver, the explanation for the seasonal reversal could be researched in the shelf currents behaviour throughout the year: figures 3.8, 3.10, 3.12 and 3.14 show the currents at 20, 120, 250 and 350 m depths over almost all the modelled shelf region, averaged over February and June[4]; figures 3.9, 3.11, 3.13 and 3.15 show the same monthly averaged currents with a zoom-in on the part of the shelf near the fjord mouth. Figure 3.7 explains the choice of these depths: the 20 m depth corresponds to the outflowing layer in summer and to the inflowing layer in winter; the summer inflow peaks at 120 m depth; the winter outflow is strong under 200 m depth (better not to choose a too deep level because of the shallowness of the shelf).
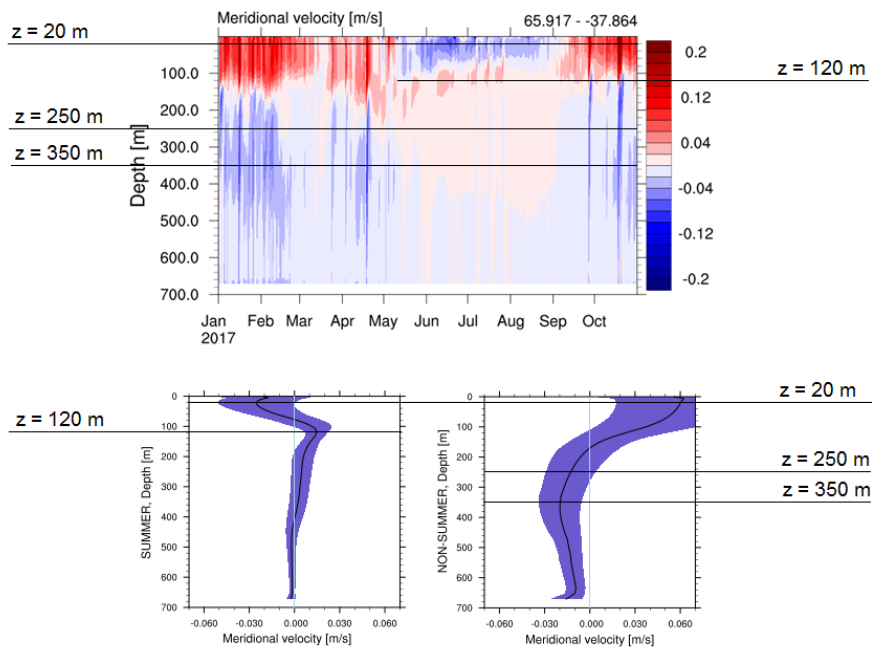
Figure 3.7: Depths at which the monthly averaged currents are represented: the 20 m depth corresponds to the outflowing layer in summer and to the inflowing layer in winter; the summer inflow peaks at 120 m depth; the winter outflow is strong under 200 m depth (better not to choose a too deep level because of the shallowness of the shelf).

---

[4]These two months are chosen as representatives of the non-summer and summer circulation.
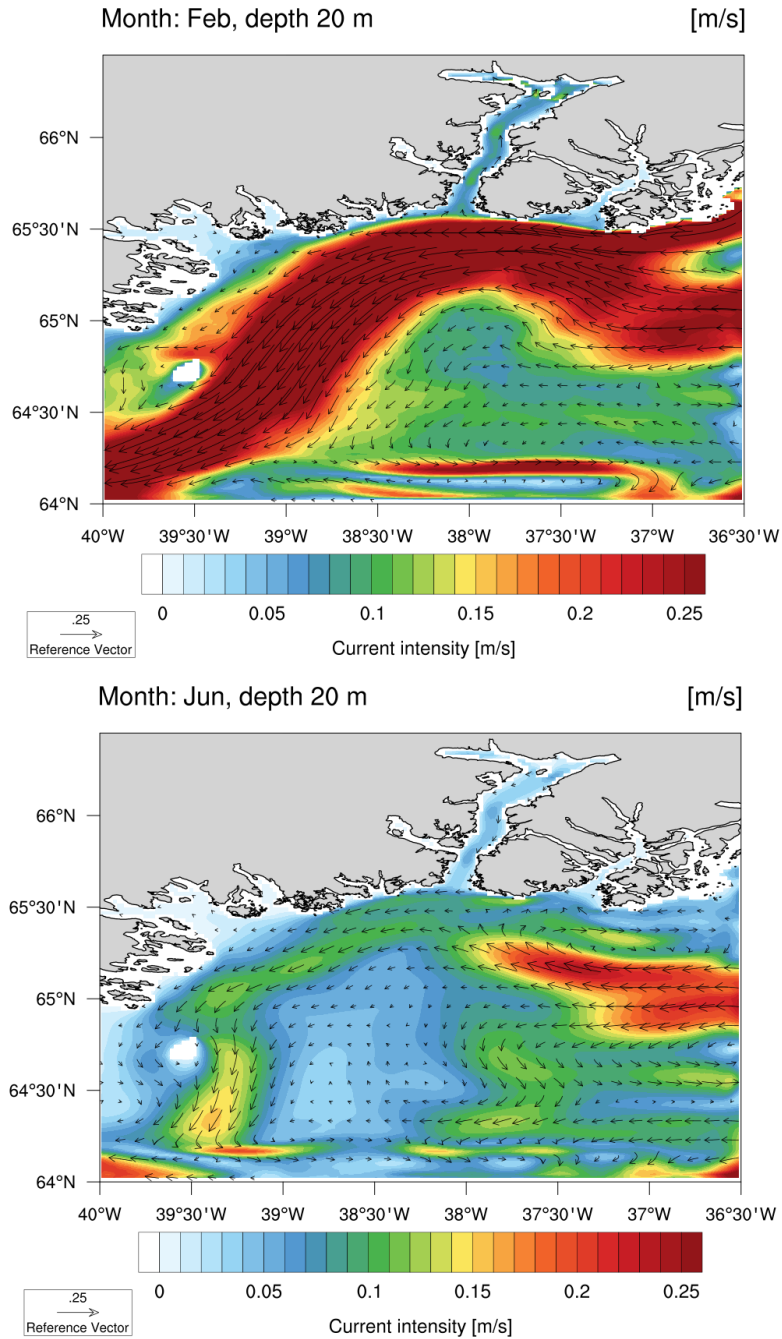
Figure 3.8: Monthly averaged currents at 20 m depth, EXP A: the arrows components are given by the monthly means of zonal ($\overline{u}$) and meridional ($\overline{v}$) velocity at each point, while the colours indicate current intensity computed as the monthly average of the hourly outputs intensities at each point: $\overline{(u^2 + v^2)^{\frac{1}{2}}}$, where the overline indicates the time average.
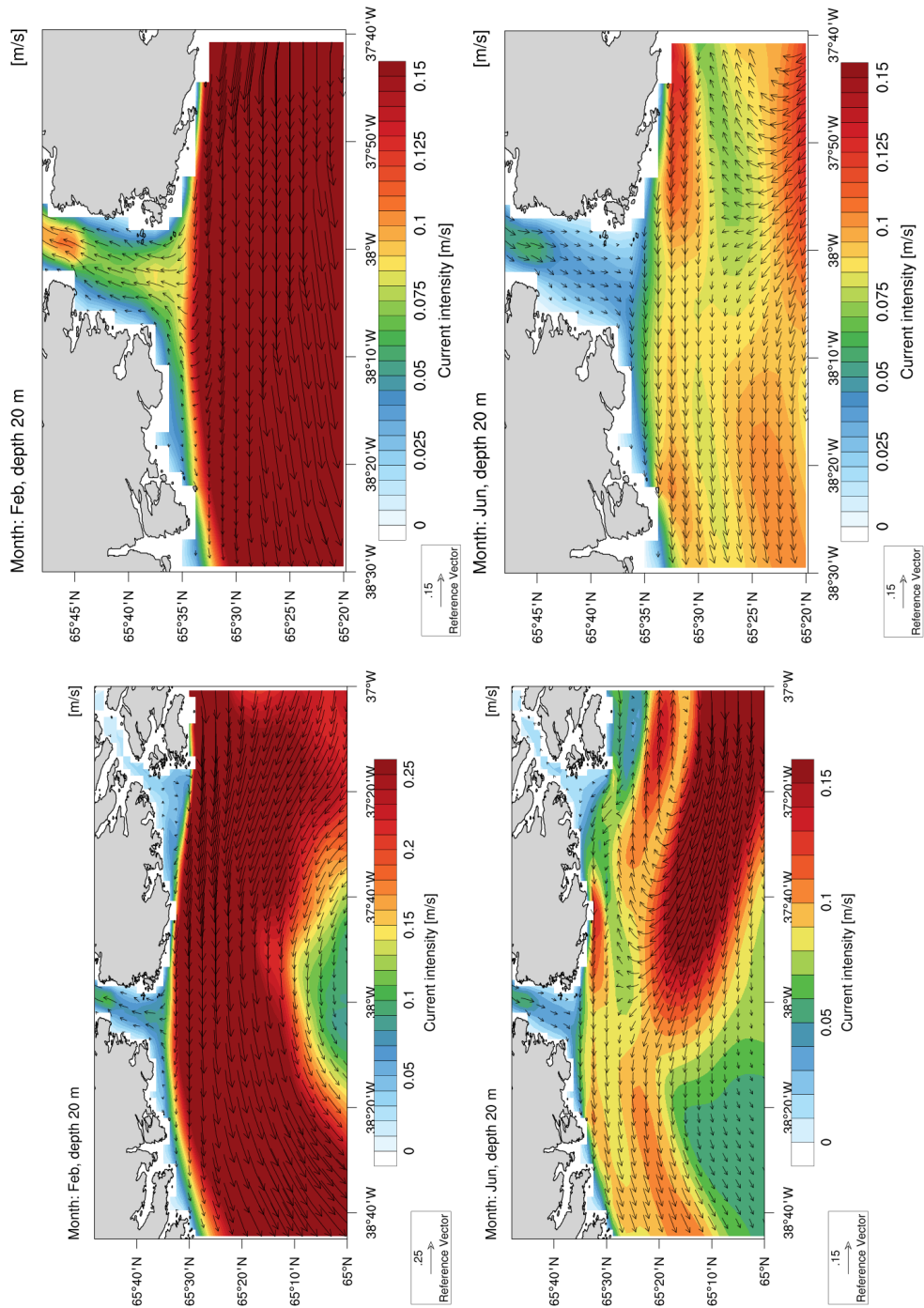
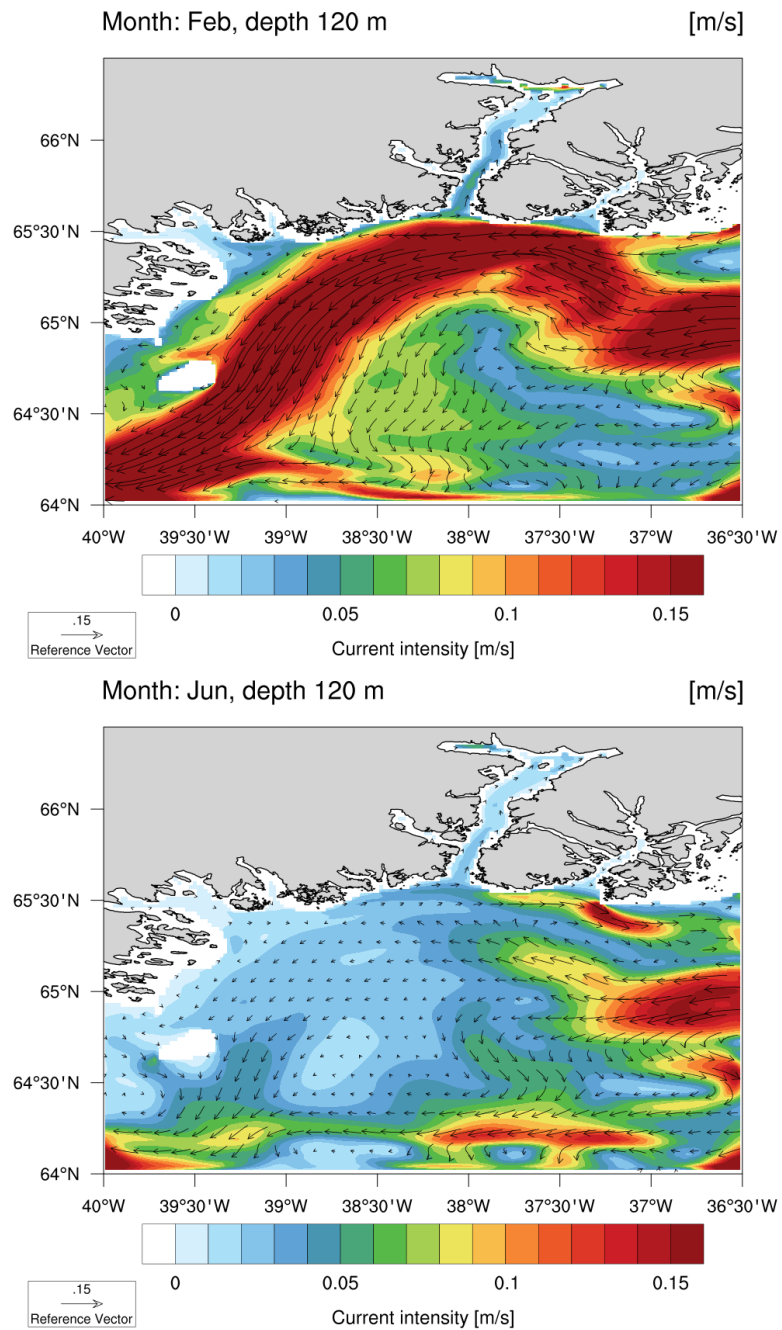Figure 3.9: Monthly averaged currents at 20 m depth, computed as in figure 3.8, EXP A.

Figure 3.10: Monthly averaged currents at 120 m depth, computed as in figure 3.8, EXP A.
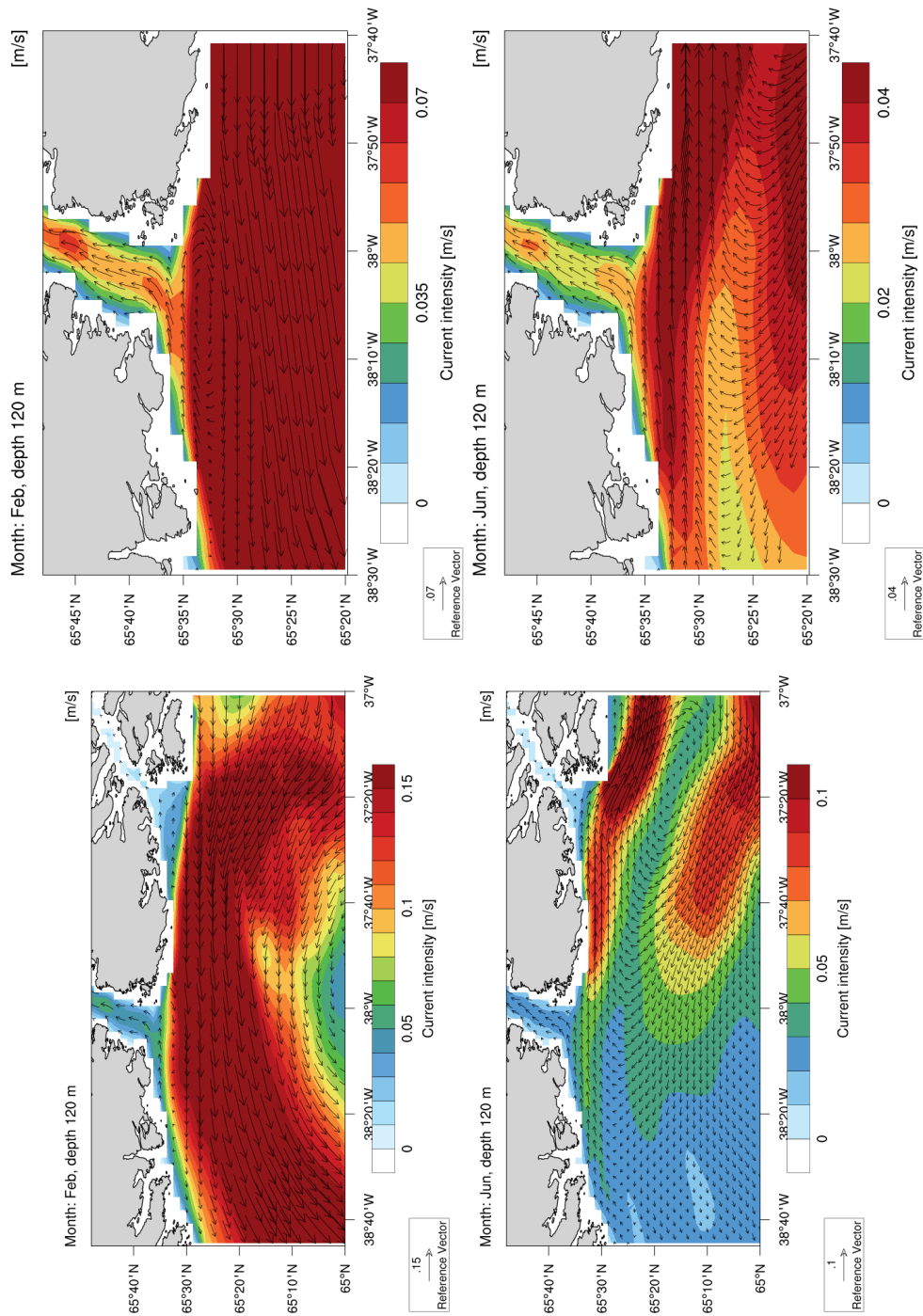
Figure 3.11: Monthly averaged currents at 120 m depth, computed as in figure 3.8, EXP A.
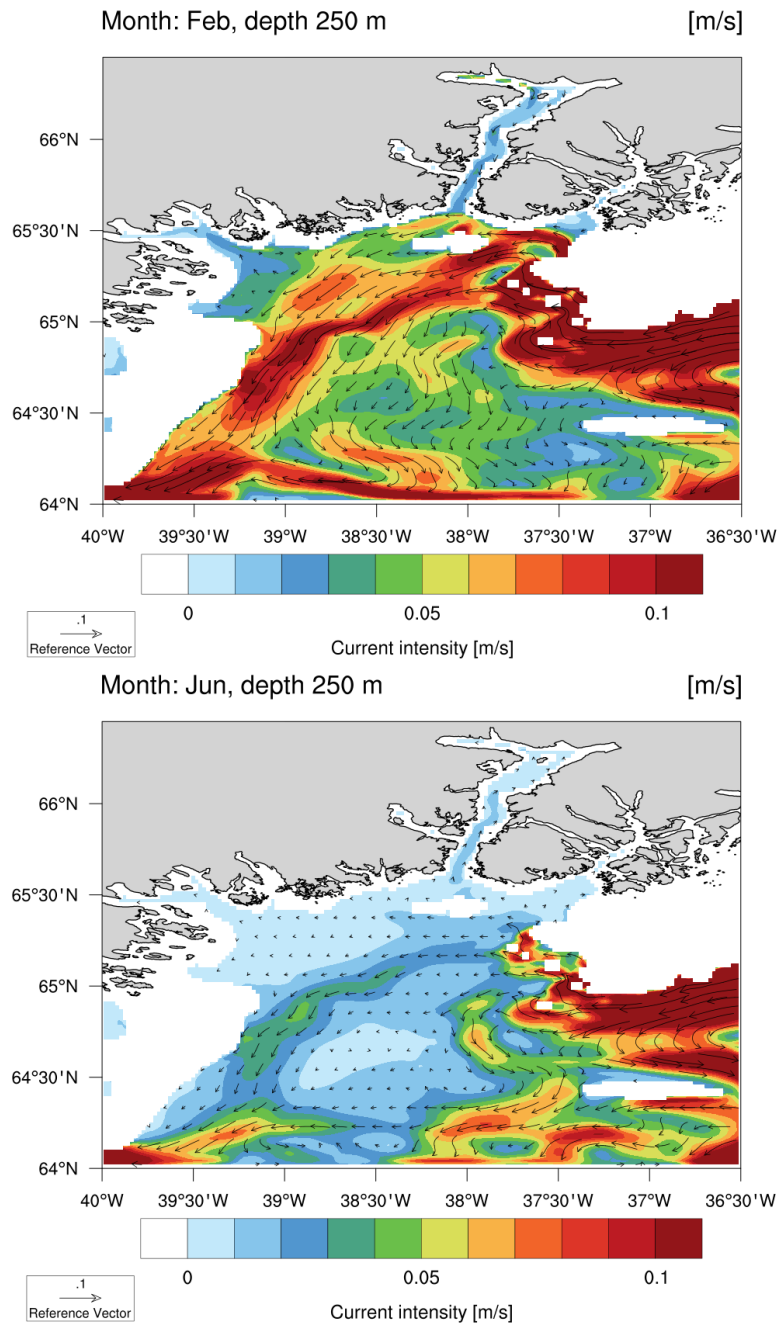
Figure 3.12: Monthly averaged currents at 250 m depth, computed as in figure 3.8, EXP A.
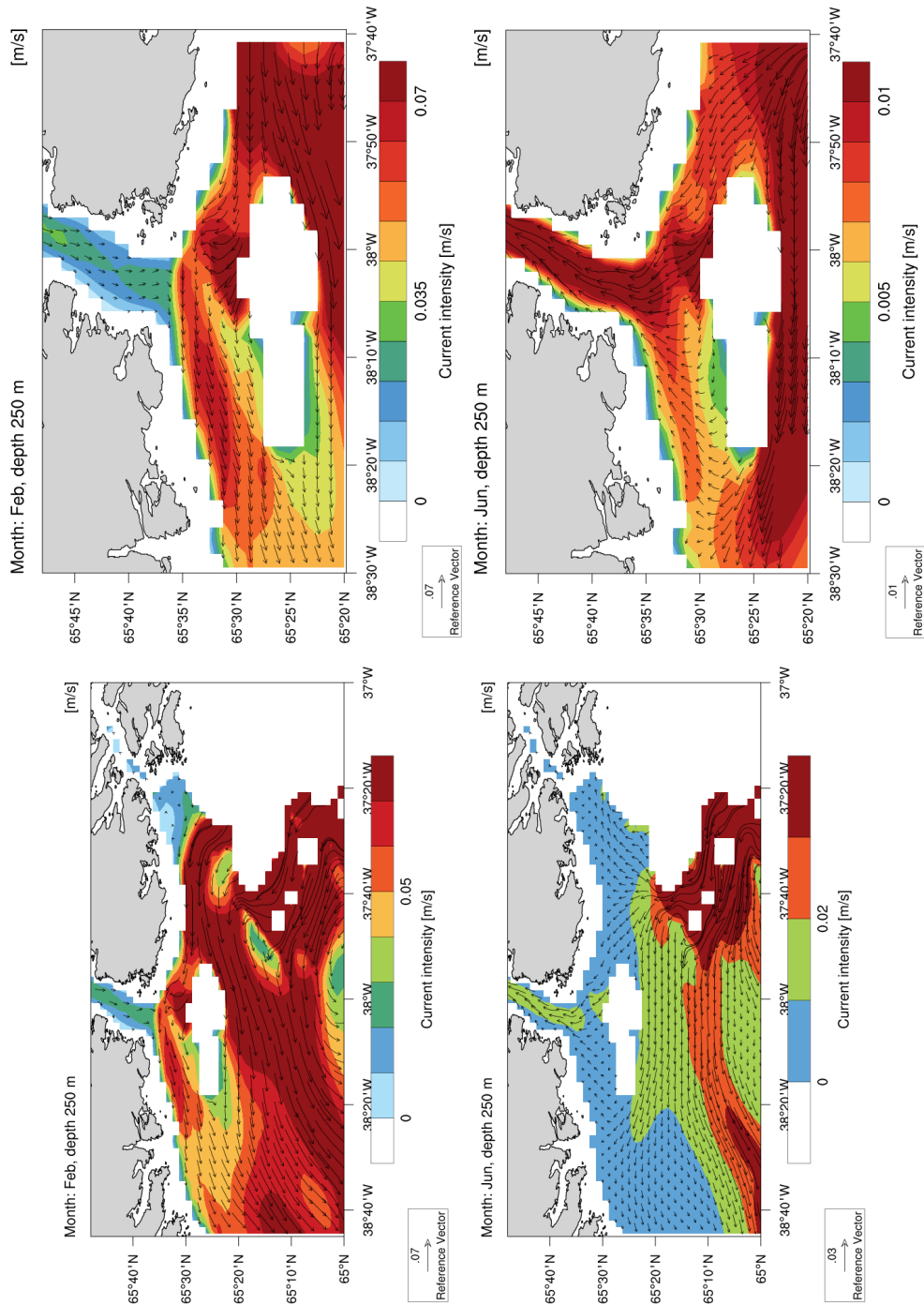
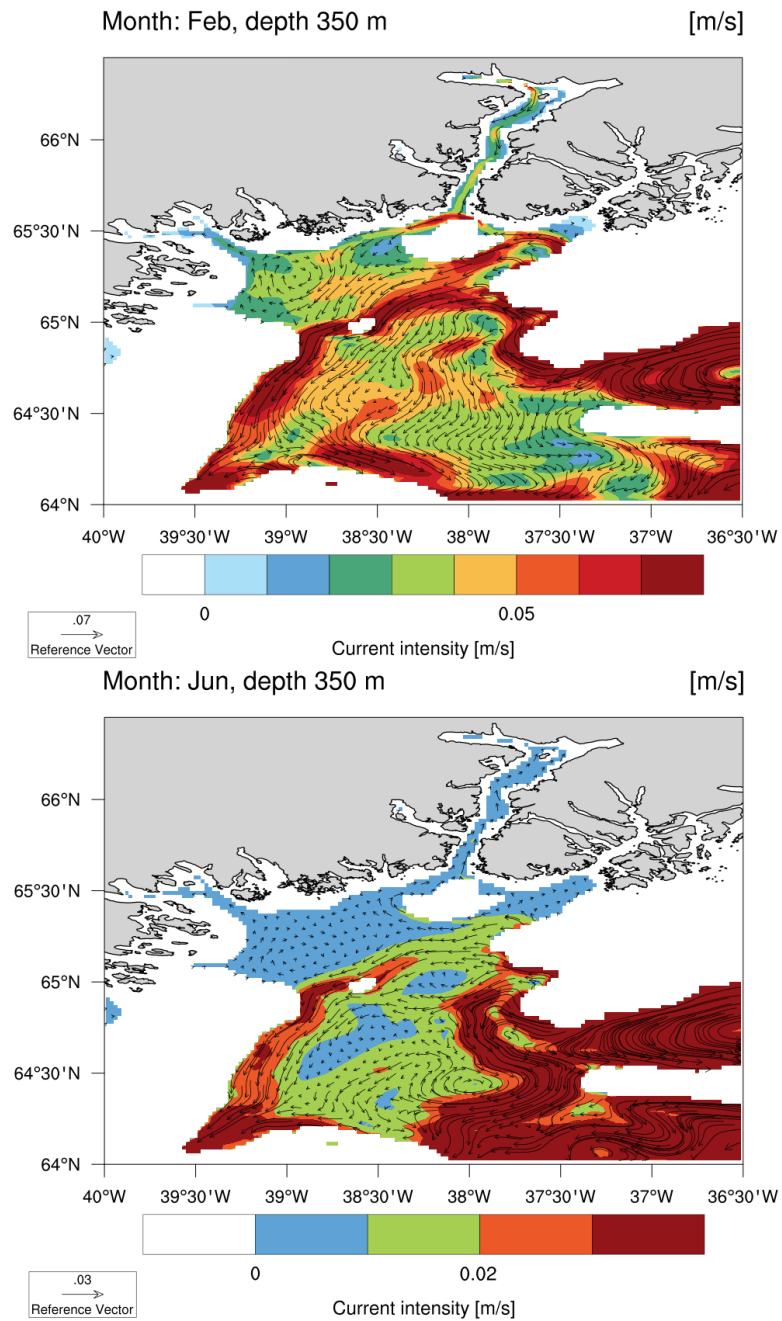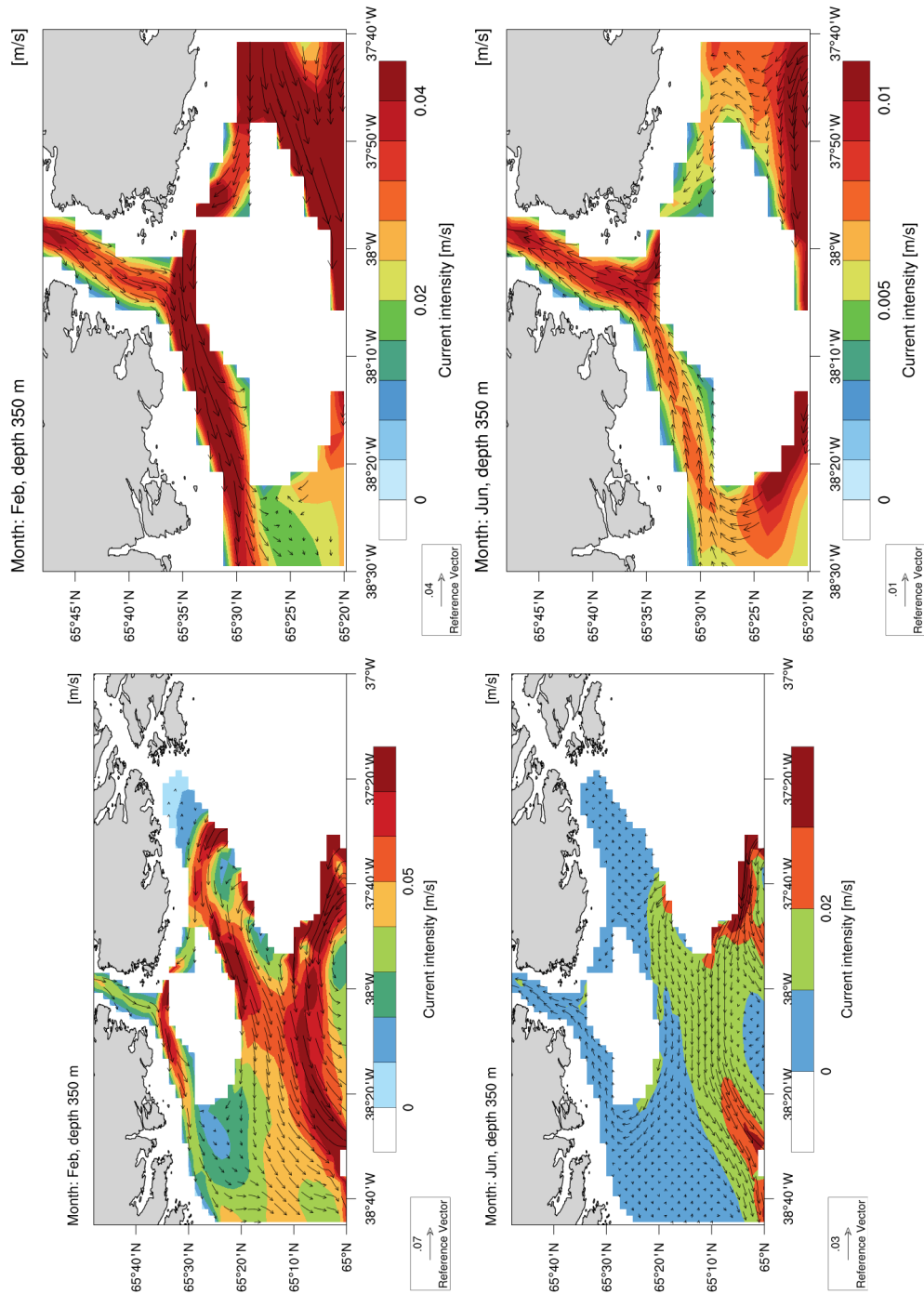Figure 3.13: Monthly averaged currents at 250 m depth, computed as in figure 3.8, EXP A.

Figure 3.14: Monthly averaged currents at 350 m depth, computed as in figure 3.8, EXP A.

Figure 3.15: Monthly averaged currents at 350 m depth, computed as in figure 3.8, EXP A.

At 20 m depth, the non-summer monthly averages (from October to April
- sampled by February in the figures) reveal the presence of a strong west-
ward cyclonic coastal current which laps the coast driving the inflow in the
fjord; summer (from June to August - sampled by June in the figures) instead
shows the weakening and detaching of this current from the coast, settling in
correspondence of a slope in the shelf bathymetry (not the continental slope:
compare figure 3.8 with figures 2.6 and 2.5(c)).

At 120 m depth the winter currents nearly resemble the ones found at 20 m
depth, as expected from the depth of the winter reversal (> 120 m) shown in
figure 3.4(b); on the contrary, the summer current pattern completely changes:
water enters the fjord from the west side of the shelf, thanks to the presence of
an eastward current that appears to be part of an anticyclonic area originating
from a meander of the weakened coastal current. The surface summer outflow
is probably the fjord reaction to this inflow, which is raising the pycnocline (as
seen in figure 3.2).

At 250 and 350 m depths in winter the coastal current is weaker and con-
strained by the bathymetry to flow farther from the coast. The fjord can thus
drive an outflowing current in response to the strong surface inflow (which
deepens the pycnocline). On the contrary, in summer, water inflows as at 120
m depth, with also a contribution from the eastern side of the shelf at 250 m;
the vorticity distribution at these depths (250 and 350 m) clearly appears to
be strongly linked with bathymetry, with the strongest currents converging on
the bottom slopes.

From the previous analysis emerges that the shelf circulation seasonal changes
are the source of the seasonal reversal. The winter cyclonic geostrophic coastal
current (East Greenland Coastal Current, see sections 1.3 and 1.6) is stronger
than the summer coastal current, as a consequence of the stronger winter wind
stress curl on a basin-wide scale: indeed, in the subpolar region, wind is dis-
tributed so as to force an Ekman suction in the open ocean and thus down-
welling conditions near the coasts and cyclonic currents around the subpolar
North Atlantic (the subpolar gyre). Moreover, frequent strong downwelling-
favourable synoptic wind events (associated to the passage of low-pressure
storms) encourage the surface entrance of shelf water in the fjord on a weekly
time scale (see chapter 4 and section 1.6.2), constraining the monthly averaged
eastern open boundary conditions to retain the characteristics of a downwelling
phenomenon: the strong coastal current entering the eastern boundary alter-
nates some days of exceptional intensity and greater closeness to the coast to
days of relative weakening (see figures 4.3 and 4.4), thus retaining a consider-

able intensity near to the coast also when monthly averaged. Therefore, the winter seasonal current pattern cannot be considered completely independent from the intermediary circulation downwelling events happening on a shorter time scale than the one used for averaging the open boundaries conditions in EXP A.

Regarding summer, the weaker coastal current does not have sufficient energy to remain close to the coast (where the shallow bottom leads to a great frictional energy loss) and thus it detaches from it to set on a slope in the shelf bottom. The horizontal shear, i.e. the requirement for velocity to approach zero towards the coast, and the wind driven geostrophic coastal current generate vorticity between the coast and the current itself: as a consequence, numerous vortices form and meanders originate weakening the coastal current by the process of mixed barotropic/baroclinic instability. The presence of an anticyclonic re-circulation area at the fjord mouth, probably linked to a coastal current meander, clearly determines the sub-surface inflow.

In conclusion, we can state that the seasonal circulation mode is controlled by the seasonal changes in basin-scale circulation and by the consequent modifications of the strength of the coastal current. Figure 3.16 shows a schematic representation of the summer and non-summer seasonal current patterns.
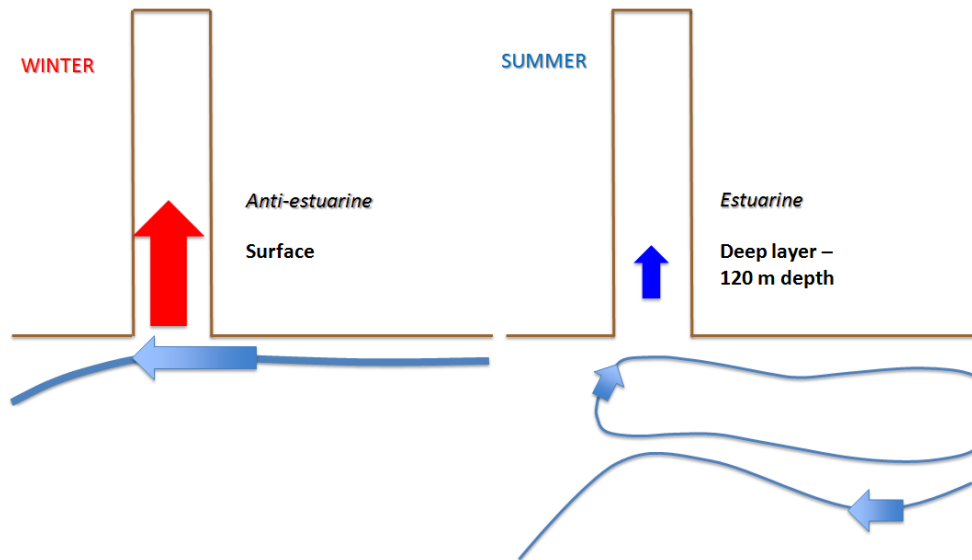

Figure 3.16: On the left: non-summer geostrophic coastal current due to the wind stress curl over the entire subpolar North Atlantic basin; downwelling-favourable synoptic wind events help the surface inflow in the fjord, as long as they influence the structure of the coastal current in the monthly averaged open boundaries conditions.

On the right: summer geostrophic shelf circulation patterns due to weaker basin-scale winds, inducing re-circulations at depth which force an entering flow at depth.

3.4   Low salinity water injection

We are left at least with one question for the summer seasonal circulation: where is the low salinity water observed in the surface layer in figure 3.2, thus exiting from the fjord, coming from?

Normally we would say it is coming from the melting of the glaciers at the head of the fjord but our model does not contain such process. We need then to investigate better our model results to see where the low salinity waters enter the fjord, to exit, then, through the summer estuarine circulation.

Comparing meridional velocity with potential density, salinity and potential temperature in figure 3.2, it is evident that the winter strong coastal current is driving relatively fresh and cold waters in the fjord at the surface (Polar Waters), determining a deep outflow of Atlantic Waters and the deepening of the pycnocline, while the summer anticyclonic currents are forcing AW to enter in the sub-surface, provoking the outflow of fjord waters at the surface and the rising of the pycnocline.

The salinity of the waters entering or exiting the fjord can be further established observing the water properties on the vertical sections on the shelf represented in figure 3.17 (sections S0 and S1).
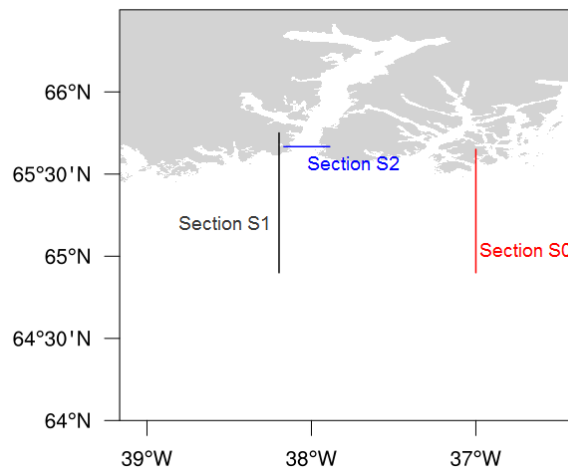

Figure 3.17: Vertical sections on which water properties are represented.

Section S0 (figure 3.18(a)) shows a correspondence between the fresher water and the negative (moving towards the fjord) surface zonal current in September and October, compatibly with the presence of low salinity water in the fjord surface layer during the same months in figure 3.2. This confirms that the relatively fresh water observed in the fjord surface layer during these months reaches the fjord from the eastern part of the shelf, probably carried by the
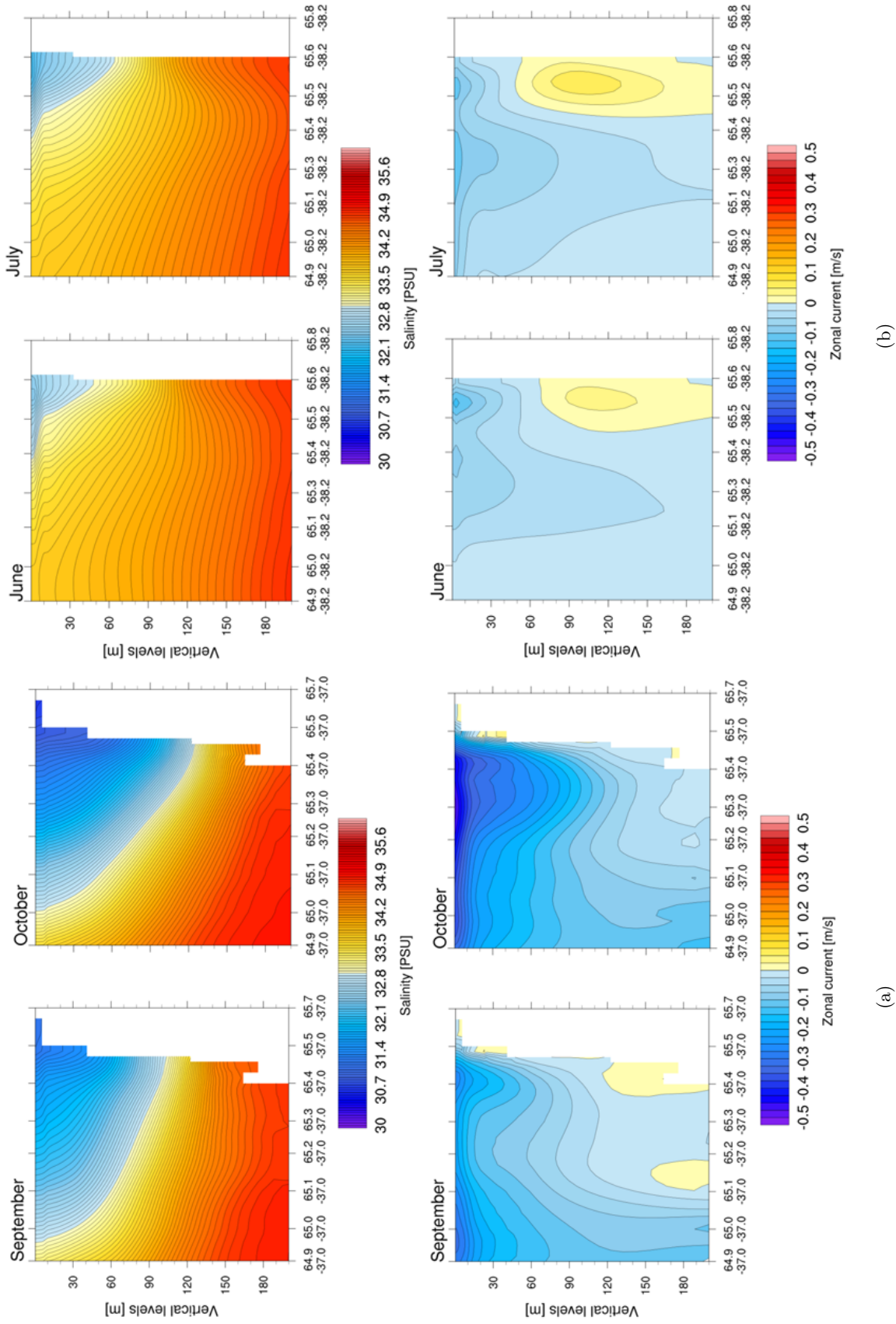
Figure 3.18: 3.18(a): Monthly averages over September and October of salinity and zonal velocity on section S0 in figure 3.17; first 200 m of the water column, EXP A.

3.18(b): Monthly averages over June and July of salinity and zonal velocity on section S1 in figure 3.17; first 200 m of the water column, EXP A.

East Greenland Coastal Current (a PW current) from the melting Arctic ice sheets (see figures 1.5 and 1.6).

The low salinity water in figure 3.18(a) is concentrated near the coast, as expected from the combination of the stratifying buoyancy input, the Coriolis force and the downwelling-favourable winds: like in a ROFI region[5] near an estuary (figure 3.19), the relatively fresh water coming from the Arctic attempts to overlay the heavier AW (the buoyancy input tends to induce stratification through an estuarine circulation in the direction of the gradient), while the action of the Coriolis force deviates the water movement to the right, thus constraining the PW current to flow with the coast to its right. The wind pattern reinforces this current configuration, further shifting the coastal current towards the coast (Simpson, 1997).
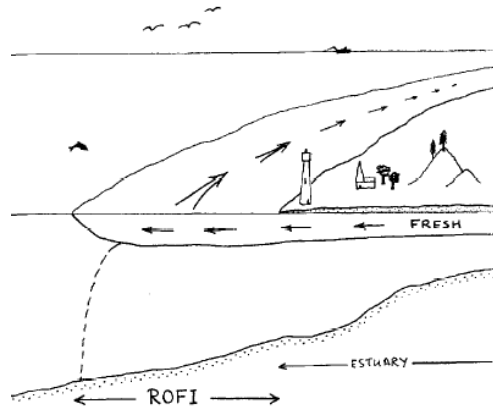

Figure 3.19: Schematic representation of a ROFI region. Reproduced from Simpson (1997).

The winter isopycnals in figure 3.20 - February are typical of a downwelling phenomenon.

Comparing, instead, zonal velocity and salinity on section S1 in June and July (figure 3.18(b)), the part of the section interested by positive zonal currents (moving towards the fjord), placed, as expected, around 120 m depth, shows the characteristic salinity of the AW layer, confirming that the summer anticyclonic current injects AW into the fjord.

The isopycnals and the isohalines from 100 m to 180 m depth in figure 3.20 - June present the characteristic rising that occurs during an upwelling, revealing the nature of the summer circulation.

---

[5]Region Of Fresh water Influence, defined as the region between the shelf sea regime and the estuary where the local input of freshwater buoyancy from the coastal source is comparable with, or exceeds, the seasonal input of buoyancy as heat which occurs all over the shelf (Simpson, 1997).
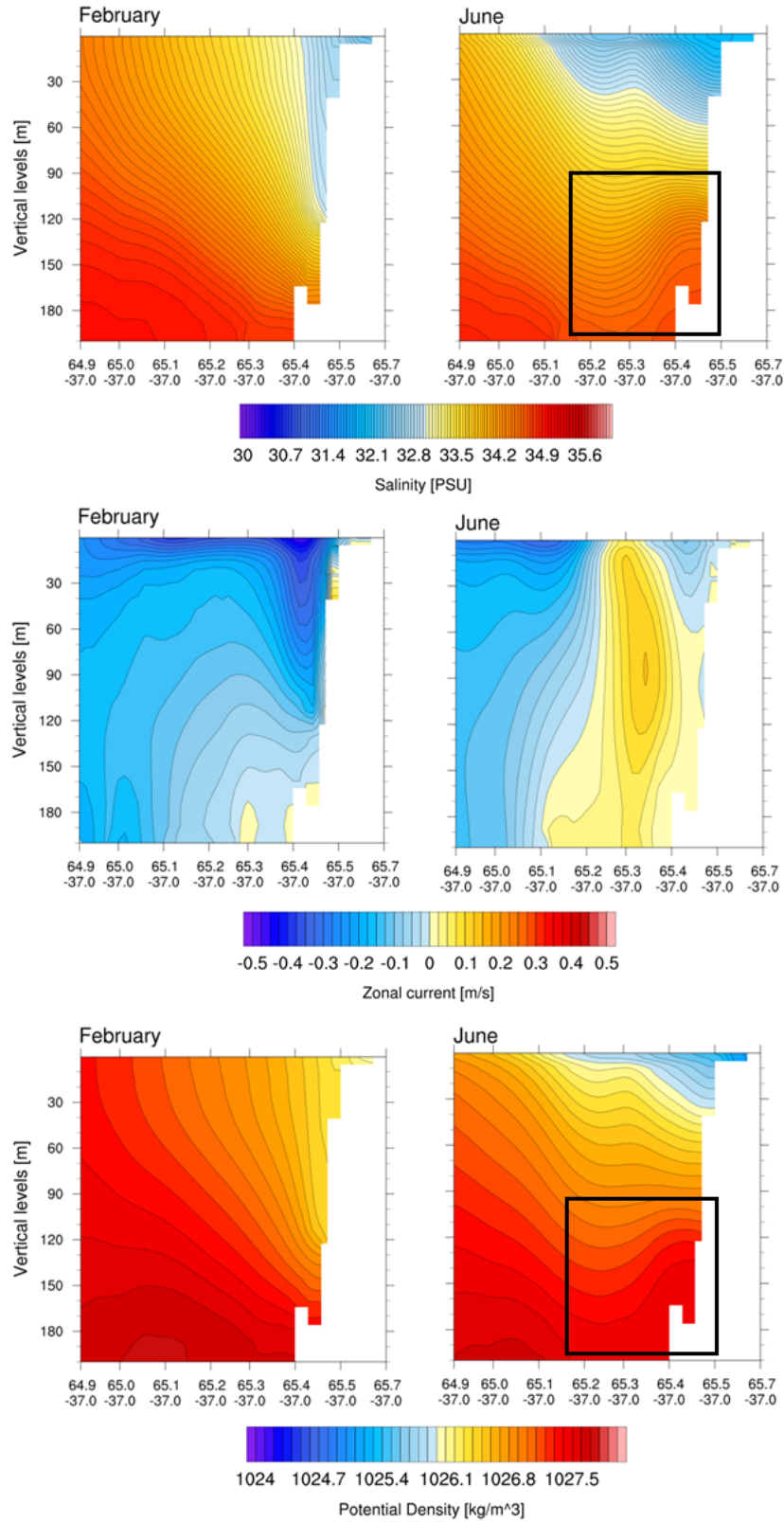
Figure 3.20: Monthly averages over February and June of salinity, zonal velocity and potential density on section S0 in figure 3.17; first 200 m of the water column, EXP A. These two months are selected as representative of non-summer and summer conditions.

As we have just proven, the principal summer mode of circulation imports warm and salty water into the fjord. Therefore, we haven't answered to the initial question yet: how can we explain the decrease in surface water salinity that is observed in the Hovmöller plot in figure 3.2, starting from the beginning of May? Observing salinity and meridional velocity on a cross-fjord section located near the fjord mouth (section S2 in figure 3.17), we find that the fresher water enters the fjord through a ~ 20 m or less deep surface layer located on the eastern side of the fjord, during occasional events lasting some days. These events are only slightly visible in figure 3.2[6] (meridional velocity), but they are well sampled by the daily averages of salinity and meridional velocity on section S2 on the 1st and the 24th of June in figure 3.21. Further entrance of fresh water happens during the three current directions reversals in July (see figure 4.17), while in August the fresher water layer depth slightly diminishes (figure 3.2 - salinity) thanks to the absence of other surface entrance events. The surface layer depth grows, then, from the end of August, as a consequence of the beginning of the winter circulation period.

---

[6]Probably because the entering layer is quite shifted towards the eastern side of the fjord, while point B is approximately on the fjord central axis.
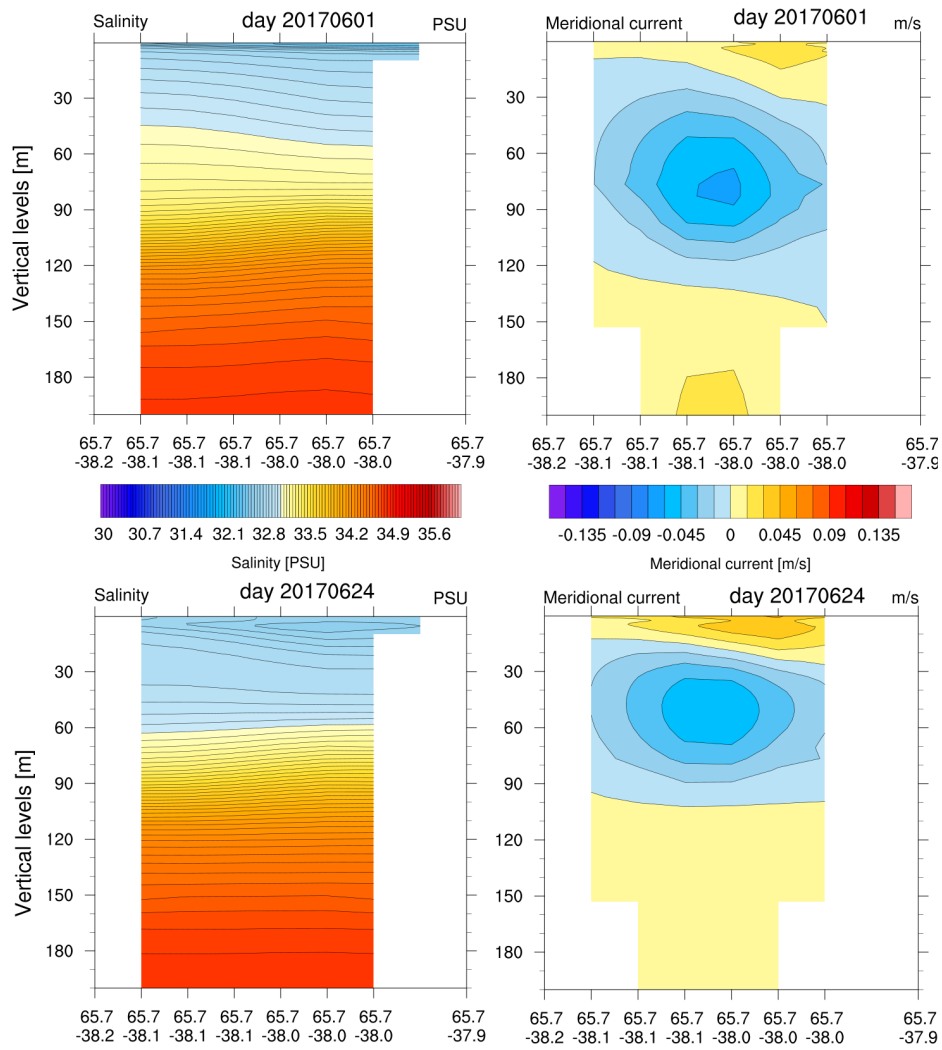
Figure 3.21: Daily averages of salinity and meridional velocity on section S2 in figure 3.17, 1 and 24 June; first 200 m of the water column, EXP A.

Sermilik fjord circulation analysis: Intermediary circulation

Contents

In this chapter we analyse the results of the simulations forced at the open boundaries by the daily outputs of GOFS16 (EXP B and EXP C in table 2.10). This leads us to study the characteristics of intermediary circulation, in particular its influence on the fjord part nearest to Helheim glacier. The analysis is conducted for the winter (EXP B, section 4.1) and summer (EXP C, section 4.2) seasons; the two seasons are, then, compared (section 4.3). At the end we examine the cross-fjord variability (section 4.4).

4.1 Winter intermediary circulation

EXP A - NEST 1 and EXP B - NEST 1 in table 2.10 differ only in the external fields that are imposed at the open boundaries: while EXP A is forced with the monthly averages of GOFS16 fields, EXP B relaxes to GOFS16 daily outputs. This difference changes the simulated fjord circulation.

Figure 4.1 represents meridional velocity and potential density obtained from EXP B - NEST 1 at point B in map 2.8. The presence of a pattern of reversing
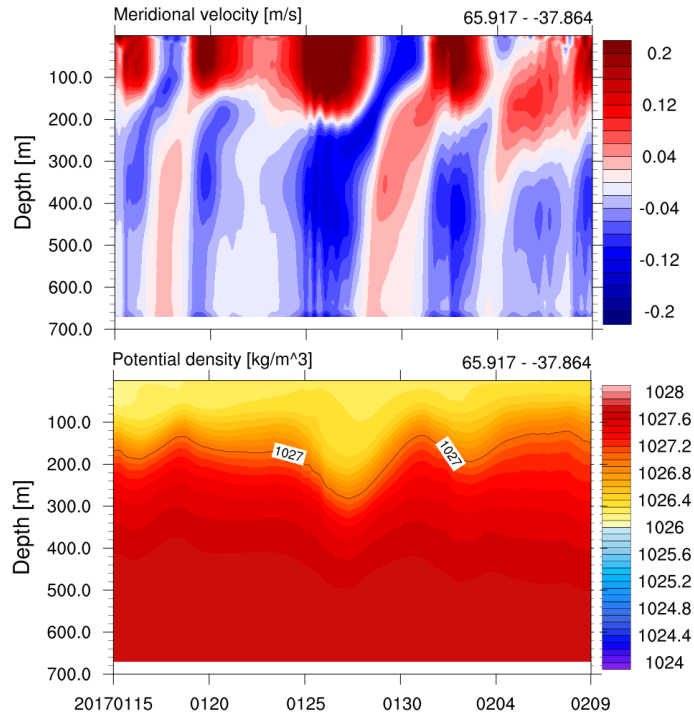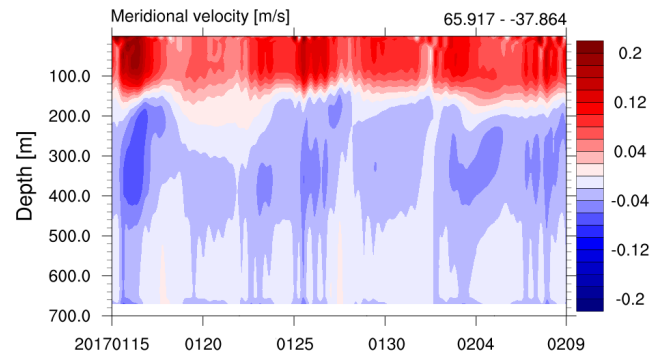
Figure 4.1: Meridional velocity and potential density obtained at point B in figure 2.8 from EXP B - NEST 1 in table 2.10. Meridional velocity is positive northward. The black line superimposed on the potential density graph indicates the pycnocline depth, where the pycnocline is identified with the 1027 kg/m^3 isopycnal following Jackson et al. (2016).

currents that wasn't produced by the EXP A simulation (see figure 4.2(a)) clearly emerges in this figure: two layers, one from surface to ~ 200 m depth and one deeper, show opposite meridional velocities; the current direction reverses at the same time in both the layers with a frequency of approximately one week. This reversals of the currents are combined with pycnocline fluctuations: water simultaneously inflows in the surface PW layer, outflows in the other (AW layer) and the pycnocline deepens; on the contrary, after the reversal, water exits the fjord at the surface, enters in the deep layer and the pycnocline rises. This is exactly what we have called intermediary circulation (see section 1.7.2).

Thus, our model is able to reproduce this circulation only when forced with the global model daily outputs at the open boundaries. This leads to the following conclusions:
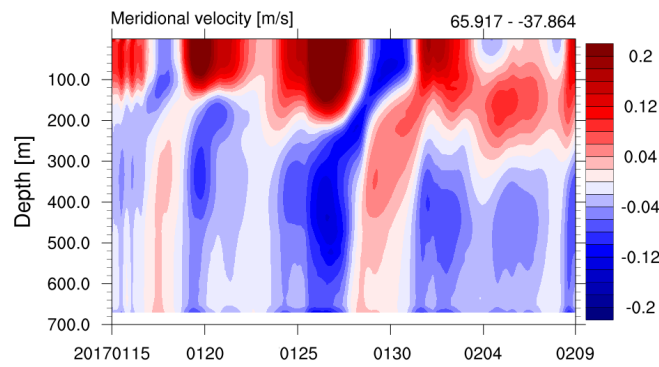
1. the presence of the high frequency reversals in EXP B - NEST 1 and not in EXP A (compare figure 4.2(a) and 4.2(b)) can be considered a proof of this circulation mode being forced by the shelf circulation, in particular by its variability on a synoptic time scale and on a spatial scale greater

(a)
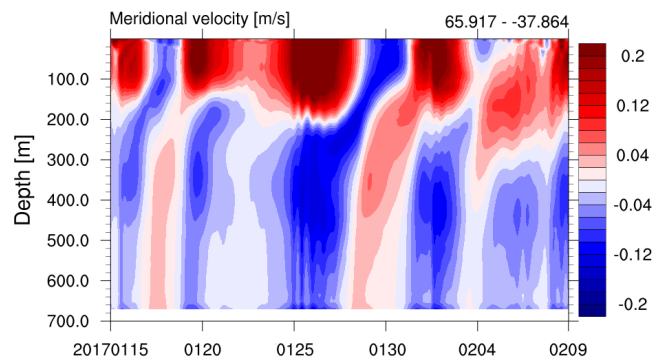
(b)

(c)

Figure 4.2: Meridional velocity obtained at point B in figure 2.8 from EXP A (4.2(a)), EXP B - NEST 1 (4.2(b)) and EXP BW (4.2(c)) in table 2.10. Meridional velocity is positive northward.

than our NEST 1 domain (i.e. more than 80 km to the east of the fjord mouth - upstream the shelf current).

As a consequence of the previous statement, intermediary circulation modelling in an east-Greenland fjord requires the simulation not only

of the fjord and near shelf dynamics, but also of at least the mesoscale shelf circulation (or even the basin-scale circulation, directly or through downscaling).

2. the up-to-date climate models, which generally do not generate outputs with frequency higher than a monthly one, cannot produce intermediary circulation in nested limited area models. This is particularly worrying if we want them to forecast and include the effects that this shelf-forced circulation might have on the glaciers retreat (see section 1.2). To do so, it would be at least necessary to build coarse resolution climate models able to store daily outputs: future climate downscaling is not possible with state-of-the-art outputs from climate models.

Figures 4.3 and 4.4 represent respectively the shelf currents at 20 m depth during a surface inflow event and during the subsequent estuarine fjord response. The shelf current is clearly exceptionally strong and remarkably near to the coast during the surface inflow event, then it weakens and moves away from the coast, allowing the fjord to react. Figure 4.4 shows also the presence of an anticyclonic recirculation vortex that facilitates the surface outflow from the fjord during the estuarine fjord response.
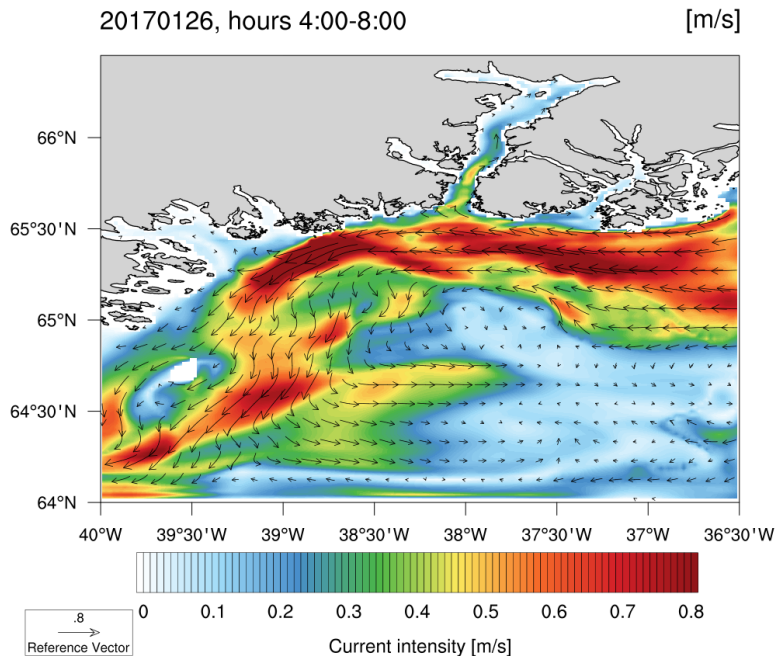

Figure 4.3: Shelf currents at 20 m depth as in figure 4.4, 26 January 2017, time average from 4:00 to 8:00, EXP B - NEST 1.
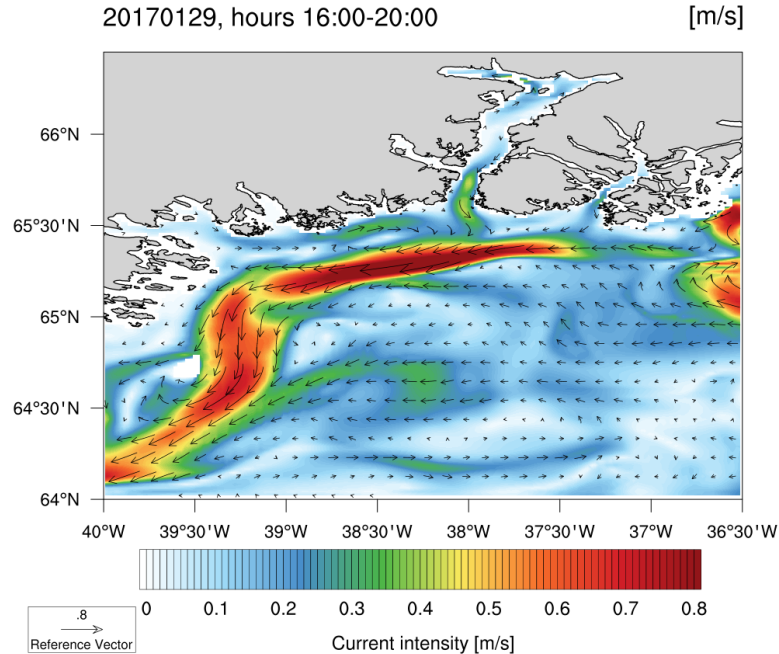
Figure 4.4: Shelf currents at 20 m depth, 29 January 2017, time average from 16:00 to 20:00, EXP B - NEST 1. The arrows components are given by the averages of the hourly zonal ($\overline{u}$) and meridional ($\overline{v}$) velocity outputs at each point, while the colours indicate current intensity computed as the time average of the hourly outputs intensity at each point: $\overline{(u^2 + v^2)^{\frac{1}{2}}}$, where the overline indicates the time average.

The role of the local wind stress in driving intermediary flows can be assessed setting up an experiment identical to EXP B, but with the wind stress constrained to be null in all the domain (EXP BW in table 2.10). Figure 4.2 shows a comparison of the currents generated at point B by EXP B - NEST 1 (4.2(b)) and by EXP BW (4.2(c)): the two Hovmöller plots show exactly the same reversals, slightly less intense without wind stress. This proves that the local wind is not responsible for the reversals, as expected from their absence in EXP A and further supporting the non-local nature of the forcing (and thus the statement in item 1 of the previous list).

The action of downwelling-favourable local wind stress is well represented in figure 4.5, which shows the circulation at 20 m depth at the beginning of day 25 January from EXP B - NEST 1 and from EXP BW: the shelf current near the fjord mouth clearly turns towards the coast in EXP B, while in EXP BW the turning is less pronounced. As a consequence, EXP B shows a slight intensification of the fjord surface inflowing current near the mouth with respect to EXP BW, which can be ascribed to local wind action.
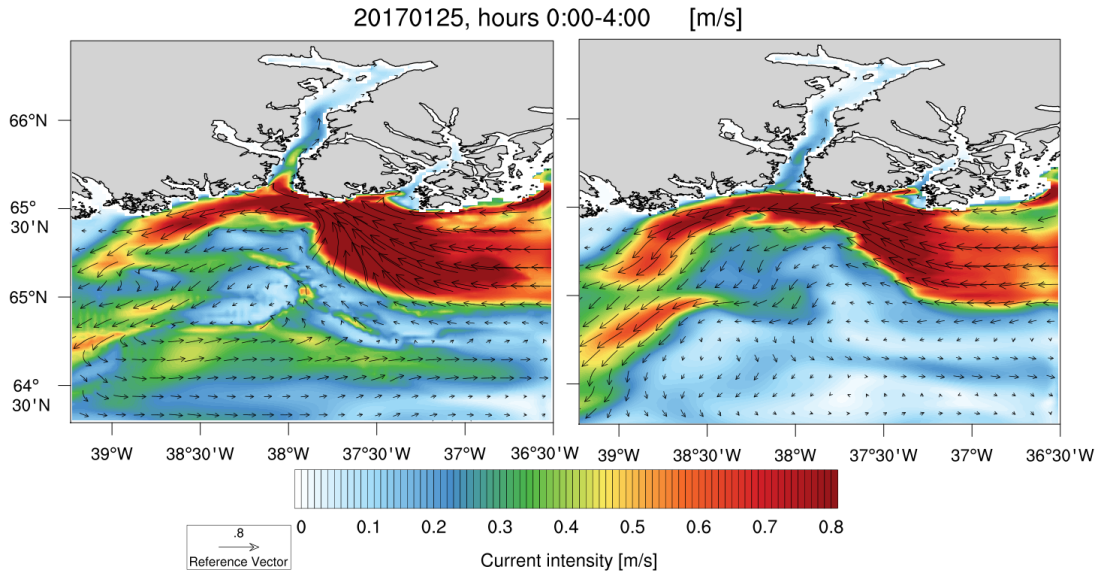
Figure 4.5: Shelf currents at 20 m depth as in figure 4.4, 25 January 2017, time average from 0:00 to 4:00 from EXP B - NEST 1 (on the left) and from EXP BW (on the right).

EXP B - NEST 2 shows a strengthening of the shelf-forced flows intensity with respect to NEST 1, especially in the deeper layer (see figure 4.6).

Together with determining an augment of currents speed, the greater resolution of NEST 2 allows to study the water properties along all Sermilik fjord, even near Helheim Glacier terminus, where the fjord width is reduced and also are the number of grid points corresponding to water: near to Helheim glacier the fjord width is resolved with just 2 or 3 points by the first nested model, while the second one represents it with 8-9 points.

Firstly, we compare the current intensities and the amplitudes of pycnocline displacements simulated at different distances from the fjord head: figure 4.7 represents meridional velocity (or the opposite of zonal velocity when it's a better approximation of along-fjord velocity) and potential density from EXP B - NEST 2 at points A, near to the fjord mouth, and C, near to the fjord head, in map 2.8. Current intensity and pycnocline displacement clearly appear to respectively reduce and amplify toward the fjord head, with a progressive reduction or growth, as one can see from some Hovmöller plots at locations in between point A and point C. This agrees with the moored observations of Jackson and Straneo (2016) and with the results of Jackson, Lentz and Straneo (2018) from analytical and numerical models.

Furthermore, the meridional current intensities observed in figure 4.6(b) are similar to the ones found at the same location by Jackson, Straneo and Suther-
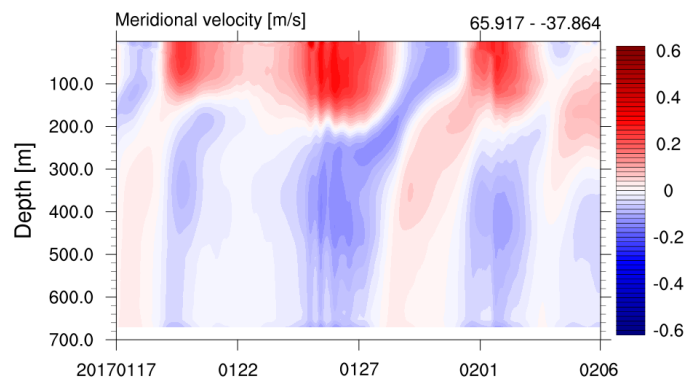
(a)
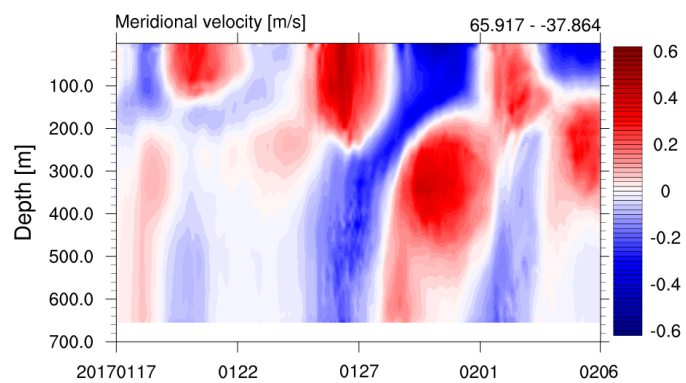
(b)

Figure 4.6: Meridional velocity obtained at point B in figure 2.8 from EXP B - NEST 1 (4.6(a)) and from EXP B - NEST 2 (4.6(b)). Meridional velocity is positive northward.
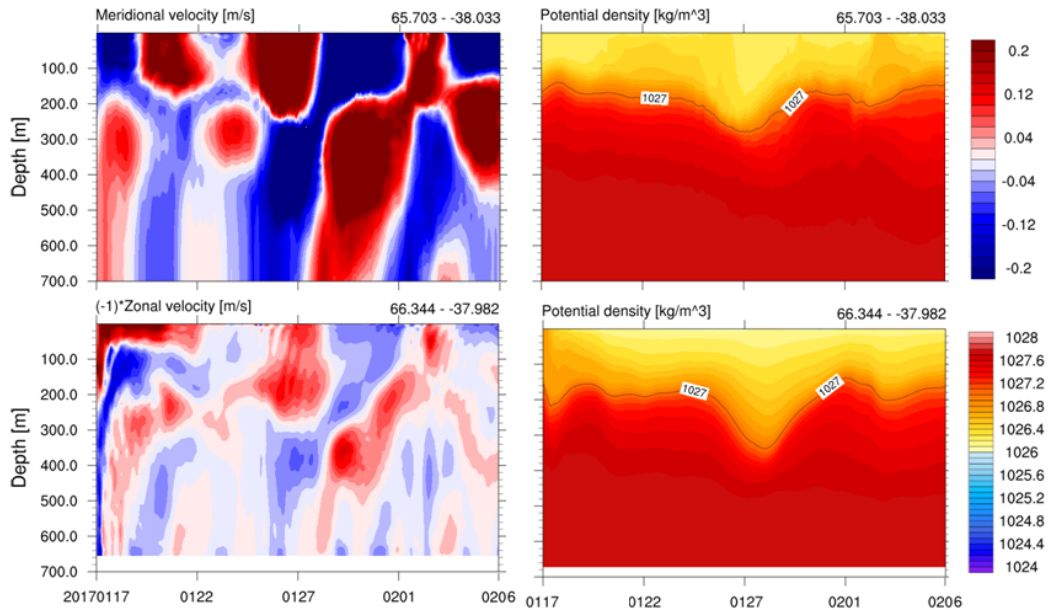
Figure 4.7: Meridional velocity (or the opposite of zonal velocity when it's a better approximation of along-fjord velocity) and potential density from EXP B - NEST 2 at points A (top panel) and C (bottom panel) in figure 2.8. The black line superimposed on the potential density graphs indicates the pycnocline depth, where the pycnocline is identified with the 1027 kg/m^3 isopycnal following Jackson et al. (2016).

land (2014) with moorings ($0.3 - 0.5 \frac{m}{s}$, see figure 1.9 and section 1.7.2), supporting again the consistency of our model results with the observed circulation. Also the amplitude of pycnocline displacements agrees with the one observed (tens to one hundred meters, see again figure 1.9 and section 1.7.2).

4.1.1   Heat and salt transports: how intermediary circulation influences water properties near the glacier terminus

We can further exploit the high resolution of the second nested model by investigating the influence of intermediary circulation on the water properties near Helheim glacier. Figure 4.7 already shows that pycnocline fluctuations near the fjord head (point C) - and thus mean water properties fluctuations - are greater than at the mouth (point A); here we want to quantify the water properties fluctuations amplitude near the glacier and to assess their relation to intermediary currents.

To do so we are going to evaluate salt and heat transports through five cross-fjord sections located at different distances from the fjord mouth and to compare salt and heat transports to the average temperature and salinity in a

fjord volume adjacent to Helheim glacier. The chosen sections and volume are represented in figure 4.8. The sections are all defined at constant latitude or longitude, so that the across-section velocity is given by the only meridional or zonal component: being the zonal and meridional velocities defined on two staggered grids (see section 2.1.1.2), indeed, the computation of the across-section velocity component wouldn't be trivial otherwise. The chosen volume is, at least during winter, usually covered by the ice mélange.
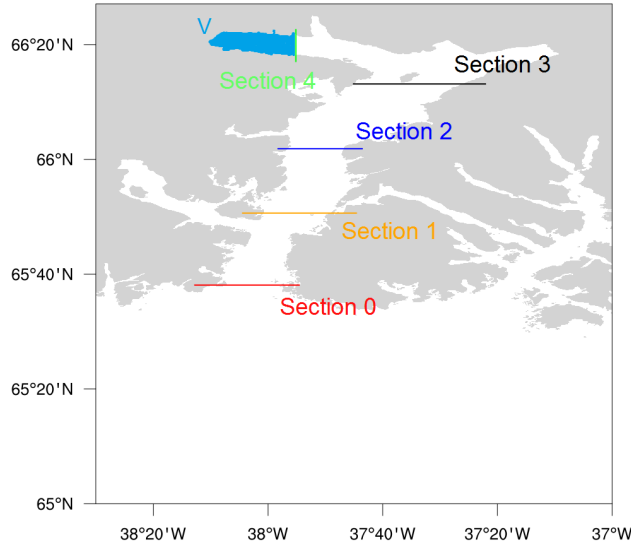

Figure 4.8: Sections through which salt and heat transports are computed. The light-blue area indicates the volume of the fjord whose water properties are analysed (V); it is bounded by section 4.

Figure 4.9 shows the heat and salt transports through these sections obtained from EXP B - NEST 2. Heat transport is defined as:

$$H_t(t) = c_p \int_A \rho(x,z,t)\theta(x,z,t)v(x,z,t) \ dxdz \tag{4.1}$$

and salt transport as[1]:

$$S_t(t) = \int_A \rho(x,z,t)S(x,z,t)v(x,z,t) \ dxdz \tag{4.2}$$

where A is the section area, v the across-section velocity in $\frac{m}{s}$ (positive towards the fjord head[2]), ρ density in $\frac{kg}{m^3}$, θ potential temperature[3] in kelvin, S salinity

---

[1]For section 4 longitude (x) must be substituted by latitude (y) in equations 4.1 and 4.2.

[2]It is, thus, meridional velocity for sections 0, 1, 2 and 3; the opposite of zonal velocity for section 4.

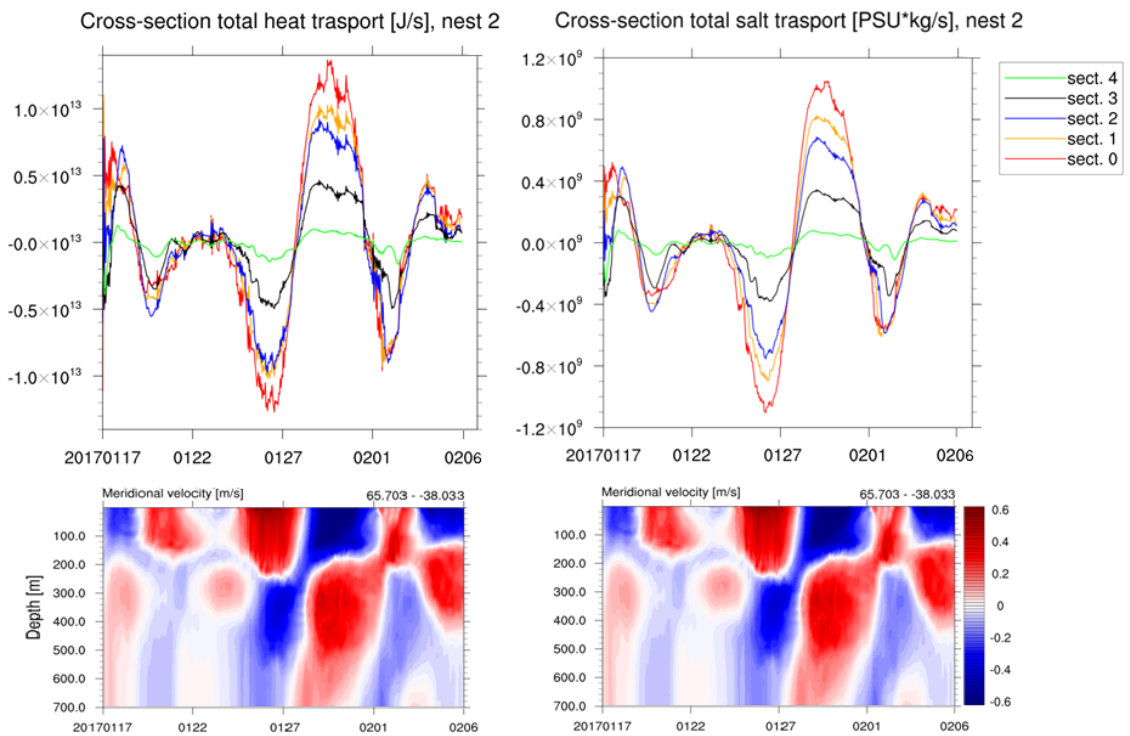[3]We use potential temperature instead of temperature since the maximum depth reached in

Figure 4.9: Heat and salt transports through the sections represented in figure 4.8 obtained from EXP B - NEST 2. They are compared with the meridional velocity Hovmöller plot at point A in figure 2.8 from the same simulation. Meridional velocity is positive northward; transports are positive towards the fjord head.

in PSU, $c_p = 4186 \; \frac{J}{kg \cdot K}$ water specific heat, x longitude and z depth in m. Thus, heat transport is expressed in $\frac{J}{s}$ and salt transport in $\frac{PSU \cdot kg}{s}$.

The sections are chosen so as to lay on the V-grid points (sections 0, 1, 2 and 3) or the U-grid points (section 4); therefore no interpolation is needed to compute the across-section velocity. θ and S fields are interpolated from the T-grid to the U or V-grid points corresponding to the sections; ρ is computed from the interpolated θ and S fields using the modified UNESCO equation of state formula by Jackett and Mcdougall (1995). The transports are then obtained recursively adding the values of $\rho S v$ or $c_p \rho \theta v$ of all the grid points on the section, each multiplied by the section area associated with the considered point ($\Delta z \cdot \Delta x$) and divided by the total area of the section.

The resulting transports can be compared with the Hovmöller diagram representing meridional velocity at point A in figure 2.8, in order to assess their relation with intermediary circulation (figure 4.9). The transports show considerable fluctuations (at least for the sections nearest to the fjord mouth) that appear to be totally coincident with the two current patterns of intermediary circulation: both heat and salt transports are positive (directed towards the fjord head) when water exits the fjord at the surface and enters it in the deeper layer; transports are, instead, negative with the opposite currents directions. This is due to the lower salinity and temperature of the surface layer water with respect to the deep layer one, combined with the pycnocline fluctuations that accompany the reversing currents[4]. We can therefore conclude that intermediary circulation is responsible for these fluctuations in the transports.

The amplitude of the transports fluctuations diminishes considering sections progressively approaching the fjord head (approximately of an order ten from section 0 to section 4). From the values of the transports alone, however, it is not clear if they significantly affect the water properties near the glacier or

---

our domain is less than 1000 m: this means that the maximum difference between temperature and potential temperature is of the order of 0.01°C, and thus it can be neglected.

[4]Considering, for example, the case of inflow at the surface and outflow in the deeper layer, the water entering the fjord, belonging to the surface PW layer, is fresher and colder than the one exiting, belonging instead to the AW layer. Therefore, supposing that the volume of water entering the fjord is approximately equal to the volume exiting the fjord (i.e. negligible variations of fjord water volume), heat and salt must be transported away from the fjord: computing the integrals in equations 4.1 and 4.2, the negative values of v are multiplied by greater values of θ or S than the ones that multiply the positive values of v, resulting in negative transports.

Furthermore, when water enters the fjord at depth and exits at the surface, if the thickness of the AW deep inflowing layer grows (i.e. pycnocline rises, see e.g. density in figure 4.7), the positive transport of heat and salt to the fjord associated with this current pattern must be amplified.

not. Indeed, as the amplitude of transports fluctuations reduces, also does the volume of water whose properties these transports are meant to change. One way to quantitatively assess the transports contribution to water properties changes near the glacier is to compare the transports trend with the one of the total heat and salt storage in the light-blue volume of figure 4.8.

The temporal variation of the total heat storage in the volume must be given by the advective and turbulent transports through section 4 (the only open boundary), by surface radiative fluxes and surface latent heat and sensible heat fluxes. We assume that the transports through section 4 are resolved by the advective component, so as to neglect the turbulent one, as done by Jackson et al. (2016); we also neglect the heat carried by surface mass fluxes, again following Jackson et al. (2016).

$$c_p \frac{\partial}{\partial t} \int_V \rho\theta \ dV = c_p \int_{A_4} \rho\theta v \ da + H_{surface} = H_{t-section \ 4} + H_{surface} \quad [\tfrac{J}{s}] \quad (4.3)$$

where $H_{surface}$ indicates the radiative, sensible and latent surface heat transports, V the light-blue volume of figure 4.8, A_4 the area of section 4.

Regarding instead salinity, the temporal change in salt storage in V is only balanced by the advective salt transport through section 4 (neglecting again turbulent transport) since all the surface mass fluxes are of zero salinity:

$$\frac{\partial}{\partial t} \int_V \rho S \ dV = \int_{A_4} \rho S v \ da = S_{t-section \ 4} \quad [\tfrac{PSU \cdot kg}{s}] \quad (4.4)$$

Let's call the total heat and salt storages in V H_s and S_s:

$$H_s = H_s(t) = c_p \int_V \rho\theta \ dV \quad (4.5)$$

$$S_s = S_s(t) = \int_V \rho S \ dV \quad (4.6)$$

and let's temporarily assume to neglect the surface contribution to heat balance. We can then integrate equations 4.3 and 4.4 in time from $t = 0$ (the beginning of the simulation) to a generic time $t = \tilde{t}$ obtaining:

$$H_s(\tilde{t}) - H_s(0) = \int_0^{\tilde{t}} H_{t-section \ 4} dt \quad [J] \quad (4.7)$$

$$S_s(\tilde{t}) - S_s(0) = \int_0^{\tilde{t}} S_{t-section \ 4} dt \quad [PSU \cdot kg] \quad (4.8)$$

Given this relation between the advective transports and the volume heat and salt storages and that $H_s(t=0)$ and $S_s(t=0)$ are constant in time, we can correlate the heat storage in the light-blue volume V, $H_s(t)$, as a function of time, to the cumulative time integral of the heat transport through each of the five sections, $\int_0^t H_{t-section\ x}(t')dt'$ (varying the upper boundary of the integration interval); the same for $S_s(t)$ and $\int_0^t S_{t-section\ x}(t')dt'$.

H_s and S_s are computed recursively adding the values of $c_p \rho \theta \Delta V$ or $\rho S \Delta V$ of all the T-grid points contained in volume V (corresponding to water, according to the sea-land mask used), where ΔV is the volume associated to each grid point[5] and ρ is given again by the Jackett and Mcdougall (1995) formula.

Figure 4.10 represents the lagged correlations between the previous quantities. The lag ranges from a minimum of 1 hour to a maximum of 15 hours, since the correlated terms are computed from the hourly outputs of the model. For example, +1 hour lag means that the correlation is computed relating the cumulative integral of transport at time t_0 ($\int_0^{t_0} H/S_t(t')dt'$) to the total heat or salt storage at time $t_0 + 1\ hour$.
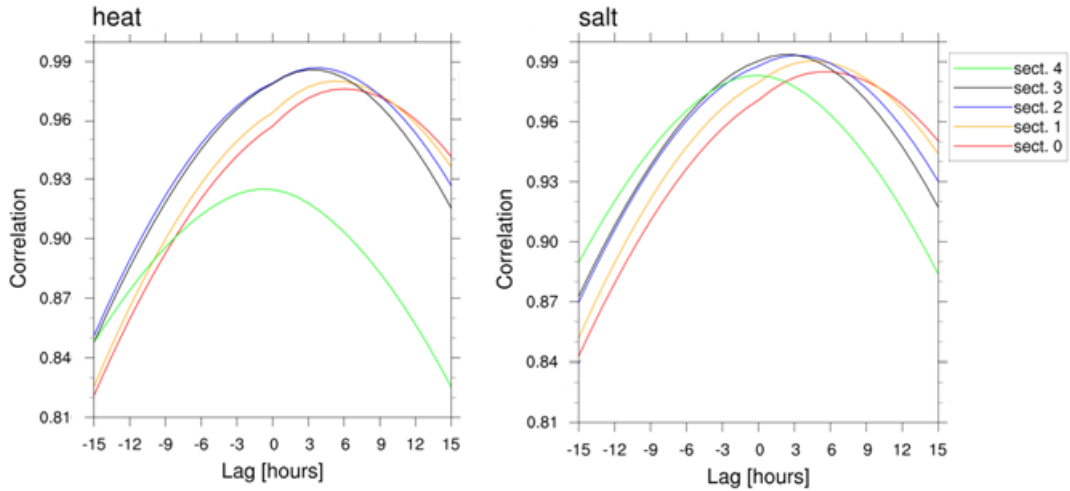

Figure 4.10: Lagged correlations between the cumulative time integrals of the heat (salt) transports in figure 4.9 and the total heat (salt) storage in the fjord volume highlighted in light-blue in figure 4.8, EXP B - NEST 2.

Figure 4.11, instead, compares the cumulative time integrals of heat and salt transports ($\int_0^t H_{t-section\ x}(t')dt'$, $\int_0^t S_{t-section\ x}(t')dt'$) to the average salinity

---

[5]The total volume of water in V is assumed to be constant in time, as the volume associated to each grid point is, since in a linear free surface model the thickness of the vertical levels is fixed. The changes in sea surface height are therefore neglected.

and potential temperature in volume V, computed as H_s and S_s but recursively adding $\theta \Delta V$ and $S \Delta V$ instead of $c_p \rho \theta \Delta V$ and $\rho S \Delta V$. Since ρ varies not more than 0.1% in the volume, the trends of the averaged salinity ($\int_V S \ dV$) and total salt storage ($\int_V \rho S \ dV$) are overall the same; the same holds for mean potential temperature and total heat storage.
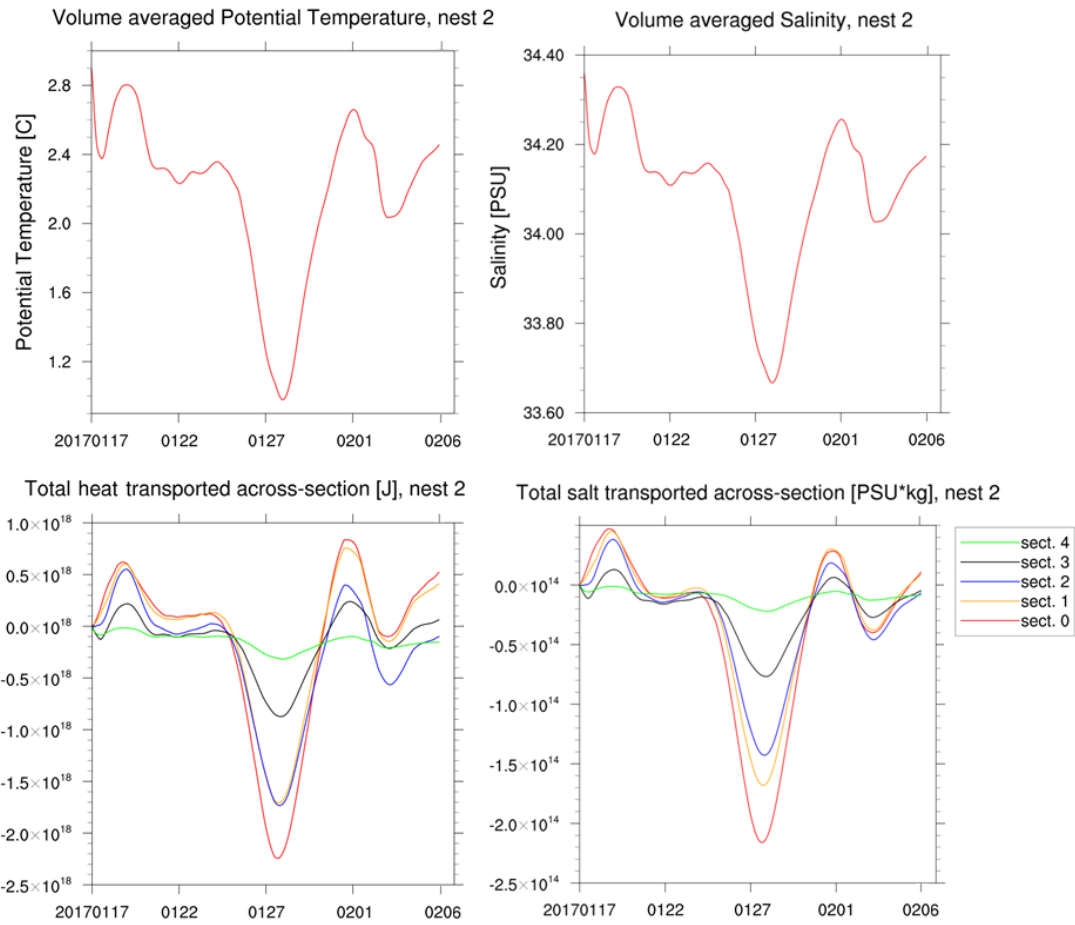
Figure 4.11: Comparison between the cumulative time integrals of the heat and salt transports in figure 4.9 (bottom panel) and the volume averages of potential temperature and salinity in the fjord volume highlighted in light-blue in figure 4.8 (top panel), EXP B - NEST 2.

The resulting correlations are very strong for both heat and salt, correctly peaking at a lag of few hours (necessary for the perturbation to travel along the fjord). The strong relation between water properties near the glacier and cumulative heat/salt transports is also evident in figure 4.11.

This means that the fluctuations in water properties near the glacier are almost

completely driven by the changes in heat and salt transports at the mouth[6]. Moreover, we have seen in figure 4.9 that the observed variations in these transports follow the intermediary circulation reversals. We can therefore conclude that intermediary circulation is able to determine significant changes in water temperature and salinity in a region of the fjord that is usually covered by the mélange, being thus in direct contact with Helheim glacier. These changes, indeed, can be up to 1.5°C and 0.6 PSU from a surface inflow episode to the immediately successive pycnocline rebound, as shown in figure 4.11.

This conclusion answers to the question whether intermediary circulation fluxes are able to influence the fjord head or not, supporting the hypotheses of Jackson et al. (2014)[7] and disproving the arguments of Cowton et al. (2016), who claimed that intermediary circulation has a limited impact on Helheim glacier as a consequence of its distance from the mouth and of the multiple recycling of the same water between fjord and shelf (see section 1.5.6).

In reality, as hypothesized by Jackson et al. (2018), the waters that enter the fjord during successive downwelling events are likely renewed at each entrance (i.e. there is no return flow of exported fjord waters), thanks to the presence of the strong coastal current that probably sweeps away the water exiting the fjord. However, to prove this, a more accurate analysis of the model results, in particular of the role of the coastal current, is required.

While we are able to completely and realistically reproduce shelf circulation outside the fjord (through downscaling), the model used by Cowton et al. directly simulates only a shelf extension similar to the one present in the second nested domain, manually applying an intermediary circulation-like forcing through the imposition of uniform pycnocline fluctuations in the open boundary conditions, and constraining the velocity field to relax to 0 at the boundary. These settings lead them to simulate intermediary circulation in a non-realistic way, since they completely eliminate the coastal current[8] and the three dimensional aspects of the circulation (given by a Kelvin wave behaviour of the perturbation, that must be allowed to both enter and exit the fjord (Jackson et al., 2018), i.e. the outcoming wave must not have imposed open boundaries

---

[6]If surface fluxes play a role in the heat balance, they play a minor role; otherwise the trends of the cumulative integrals of transports and of the volume averages in figure 4.11 would show significant differences and the correlations in figure 4.10 would be smaller.

[7]From the temperature fluctuations observed with moorings at mid-fjord, assuming these fluctuations to be representative of properties changes near the glacier, Jackson et al. calculated that the non-summer submarine melt rate in Sermilik fjord should vary by $\pm 20 - 50\%$ of its mean value on synoptic time scales (see section 1.5.5).

[8]At least, they assign a passive *shelf tracer* to all the waters exiting the fjord, thus considering the lower limit of no return flow of exported fjord waters.

conditions as in Cowton model). This setup may have led them to underestimate the effects of this circulation mode on the near-glacier waters.

Furthermore, Cowton et al. state that the intermittent nature of intermediary flows reduces their influence on the waters near to the glacier: according to Cowton, during the second of two successive downwelling events, imported shelf waters tend to be exported back to the shelf rather than transported further up-fjord. However, from our results, it is clear that the amplitude of water properties fluctuations at the fjord head is mostly related to the strength of the shelf forcing and not to the previous happening of other events. While Cowton et al. study the rate at which waters within the fjord are renewed by waters from the shelf, we analyse the tracers changes in the water volume near the glacier and we attribute them to intermediary circulation, with a more direct approach if the impact of intermediary flows on the glaciers is to be evaluated[9]. The Cowton's approach does not account (or at least not directly) for the fact that the properties of waters near the glacier depend much more on the relative thickness of the PW and AW layers than on the source of the water, being the vertical gradients much more pronounced than the horizontal[10]. Even if the shelf water is exported before reaching the head, what is important is not that shelf water arrives up to the glacier but that the pycnocline depth perturbations do[11].

Regarding the ability of shelf-driven pycnocline depth perturbations to arrive at the fjord head, our model clearly demonstrates that, despite the slowdown of the currents velocity, the pycnocline fluctuations amplify towards the fjord head and so do the mean water properties fluctuations: figure 4.12 shows that volume averaged salinity and temperature near the glacier fluctuate with amplitudes greater than the ones of the entire fjord waters. The complex fjord geometry and bathymetry, thus, are not an obstacle for the propagation of these perturbations.

Our model is the first able to simultaneously reproduce realistic fjord bathymetry, geometry and shelf conditions: here lays the importance of our results.

---

[9] Recall that submarine melt rate scales linearly or quadratically with ambient water temperature (see section 1.5.5)

[10] For example, see density in figure 4.7 within the fjord, at various distances from the mouth; moreover, surveys of Sermilik fjord show a weak or non-existent horizontal density gradient also between the fjord and the shelf (Sutherland et al., 2014).

[11] We are interested in the heat and salt supply to the glacier that is induced by intermediary circulation; finding, instead, the influence of this circulation mode on the time necessary for a change in shelf water properties (within a single layer) to reach the fjord head is a whole other ball game.
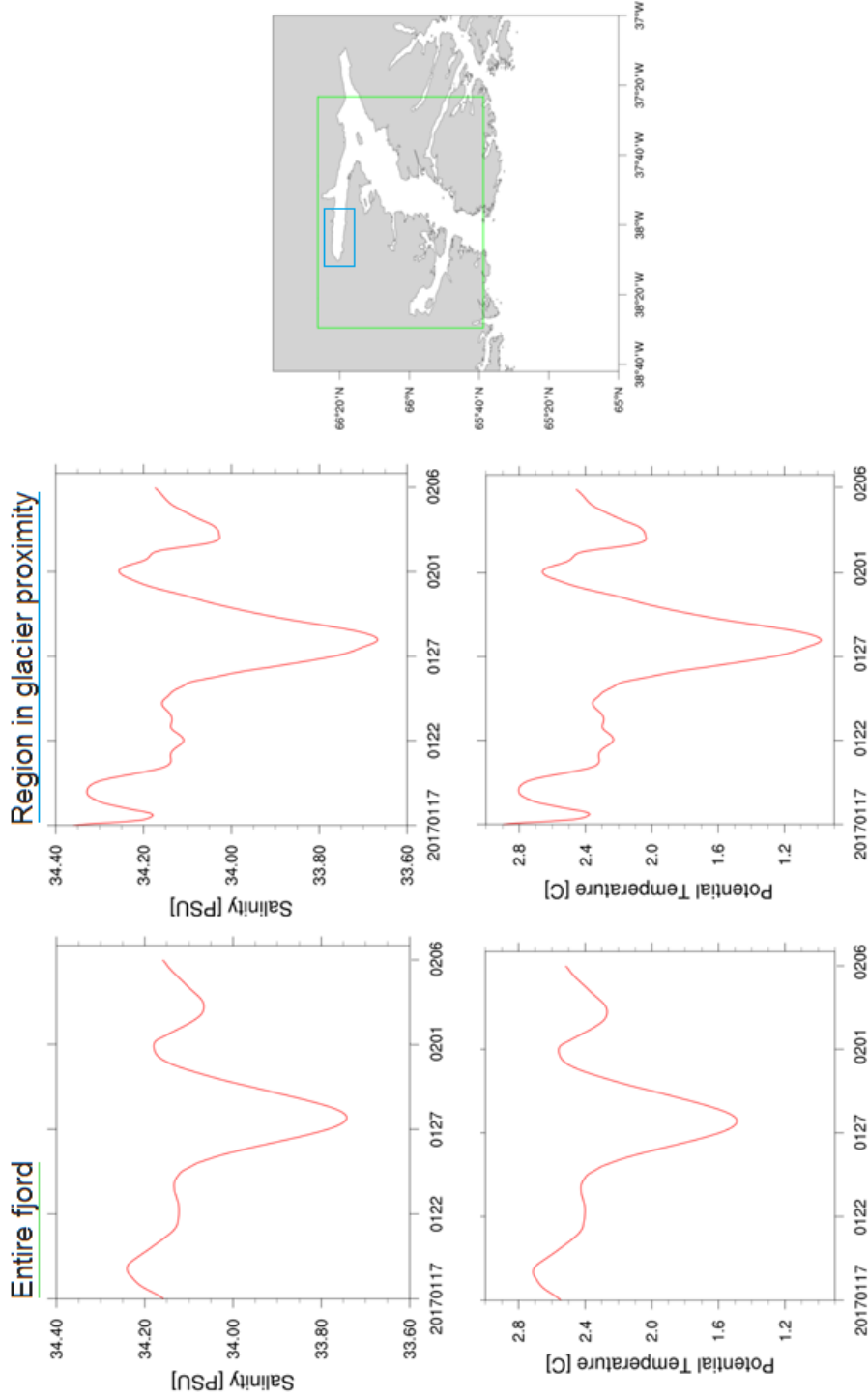
Figure 4.12: Comparison between the volume averages of potential temperature and salinity over the fjord volume framed in green (on the left) and over the volume framed in light-blue (volume V in figure 4.8, on the right), EXP B - NEST 2.

Propagation speed of pycnocline perturbations

The computation of the lagged correlations between the transports through each of the sections 0, 1, 2 and 3 and the transport through section 4 should provide us with some information about the time necessary for pycnocline perturbations to reach the fjord head. Figure 4.13 represents these correlations with a maximum lag of 14 hours, where a lag of +1 hour indicates that the correlation is computed relating the transport through section 0, 1, 2 or 3 at time t_0 to the transport through section 4 at time $t_0 + 1$ *hour*.
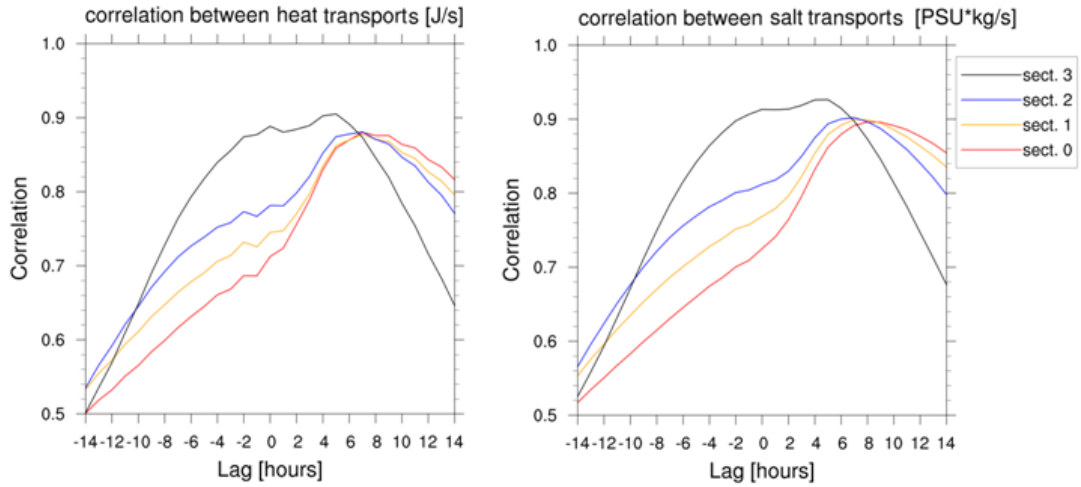

Figure 4.13: Lagged correlations between the heat or salt transports through each of the sections 0, 1, 2 and 3 and the transports through section 4 (the transports are represented in figure 4.9), EXP B - NEST 2.

The lags at which the correlations peak are correctly positive and increasing from section 3 to section 0. The propagation velocity diminishes approaching the fjord head being the peaks at 4.5 hours lag for section 3, 6.5 hours for section 2, 7.5 for section 1, 8.5 for section 0: if we interpret the lag as the time necessary for the perturbation to reach section 4 starting from the considered section, we have that it travels from section 0 to 1 (26 km) in 1 hour, from section 1 to 2 (21 km) in 1 hour, from 2 to 3 (24 km) in 2 hours, from 3 to 4 (19 or 26 km depending on the side of the island travelled) in 4.5 hours. It covers all the fjord length (approximately 90 km from section 0 to section 4) in 8.5 hours: this means that its average propagation velocity is $\sim 2.9 \ \frac{m}{s}$.

According to Jackson et al. (2018), intermediary circulation in Sermilik fjord can be largely explained with internal Kelvin wave dynamics. The speed of a reduced gravity Kelvin wave is given by $\sqrt{\frac{g\Delta\rho}{\rho}H}$, where $g = 9.81 \ \frac{m}{s^2}$ is the gravitational acceleration, $\Delta\rho$ the density difference between the PW and

AW layers $\sim 1.4 \; \frac{kg}{m^3}$, ρ a reference density, say $1027 \; \frac{kg}{m^3}$, H the water depth. The average depth is ~ 700 m, so that the resulting Kelvin wave mean speed is $\sim 3.06 \; \frac{m}{s}$, which is compatible with the $\sim 2.9 \; \frac{m}{s}$ found correlating the transports[12]. This can be considered an additional proof of the dynamical nature of shelf-forced flows.

The diminishing of the propagation speed towards the fjord head is consistent with the decrease of water depth; however, it must be noted that the wave speed reduction derived from the correlations is greater than the one that would be induced by water depth decrease. Thus, further analysis is required.

Comparison between the transports from NEST 1 and NEST 2

All the previous analysis is conducted using the results of the second nested model: this is because the first nested model does not have enough resolution to correctly represent the northern part of the fjord.

This is clear from the comparison of the transports obtained from the two nested models (figure 4.14): NEST 1 transports through sections 3 and 4 have a trend that's completely different from the one of sections 0, 1 and 2 and of all the sections of NEST 2. Therefore, the study of shelf-driven circulation impact on Helheim glacier requires a resolution greater than $1/48°$.
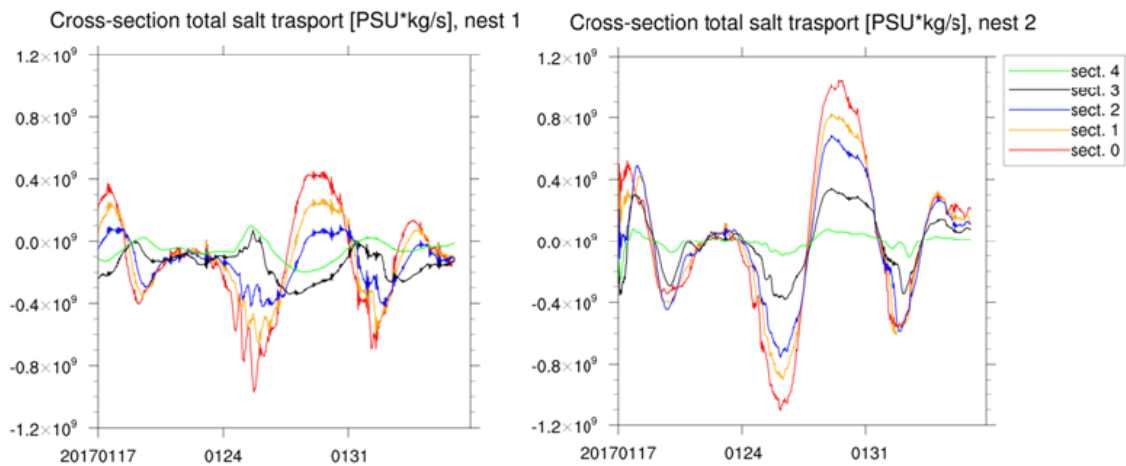

Figure 4.14: Salt transports through the sections represented in figure 4.8 obtained from EXP B - NEST 1 (left graph) and from EXP B - NEST 2 (right graph).

---

[12]given the huge approximations made identifying the lags at which the correlations peak and identifying the mean depth to insert in the propagation speed formula.

4.2   Summer intermediary circulation

EXP C - NEST 1 simulates fjord circulation with daily open boundaries conditions in July. Figure 4.15 shows meridional velocity and potential density obtained at point B (in map 2.8) from this experiment: the currents reverse also in summer, alternating inflowing velocity in a surface layer and outflow in a deeper layer to outflow at the surface and inflow in the deep layer. The two current patterns coincide respectively with the deepening or raising of the pycnocline. Again, this conforms to intermediary circulation description; thus, in our model, also summer fjord circulation shows great influence from shelf circulation.
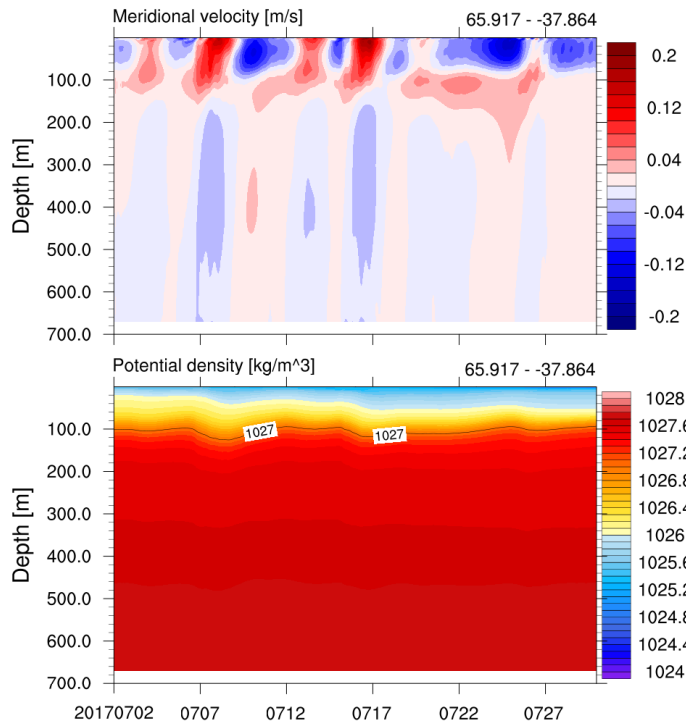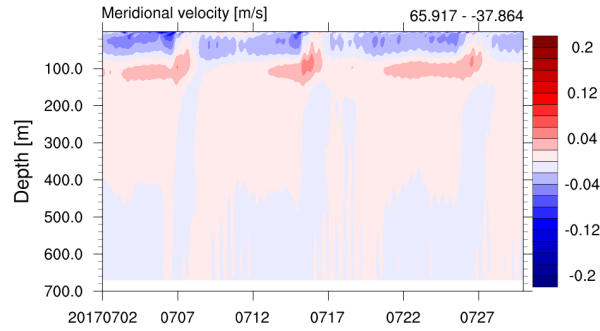

Figure 4.15: Meridional velocity and potential density obtained at point B in figure 2.8 from EXP C - NEST 1 in table 2.10. Meridional velocity is positive northward. The black line superimposed on the potential density graph indicates the pycnocline depth, where the pycnocline is identified with the 1027 kg/m^3 isopycnal following Jackson et al. (2016).

We have chosen to simulate this summer month, July, in order to not only analyse the summer daily forced circulation, but also to contrast it with the EXP A - NEST 1 circulation arising from the monthly mean boundary forcing, in particular regarding the three weak current reversals, divided by periods of approximately 10 days (figure 4.16(a)), that are present in July in EXP A. These reversals are also reproduced by EXP C, but with greater current in-

tensity and with a shifting of the peak inflow velocity from a depth of ~ 100 m to the surface (at least for two of the three reversals, see figure 4.16(b)). In addition to this, EXP C adds some other reversals between the previous, reducing their average frequency to ~ 4 days.

(a)
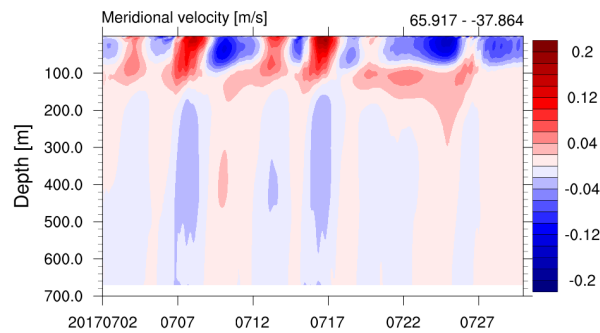
(b)
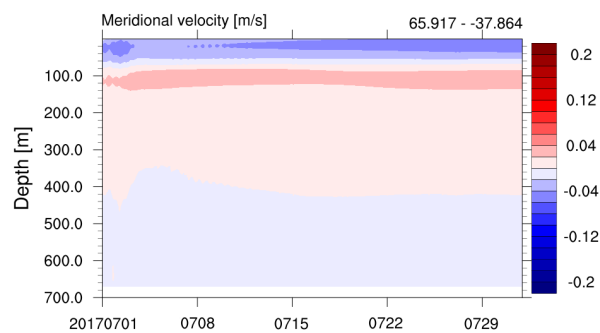
(c)

Figure 4.16: Meridional velocity obtained at point B in figure 2.8 from EXP A (4.16(a)), EXP C - NEST 1 (4.16(b)) and EXP AWJUL (4.16(c)) in table 2.10. Meridional velocity is positive northward.

It must be remarked that the three July reversals in EXP A do not sample the reversals frequency of this simulation, both in summer and non-summer peri-

ods: examining the Hovmöller diagram of EXP A meridional velocity (figure 4.17), it is easy to verify that, during all the ten months of simulation, only happen 6 or 7 reversals, of which three are in July, one or two in March and two in April. The July ones are therefore the only reversals that happen in summer. The presence of these few events in EXP A, thus, does not invalidate the conclusions at the beginning of section 4.1.
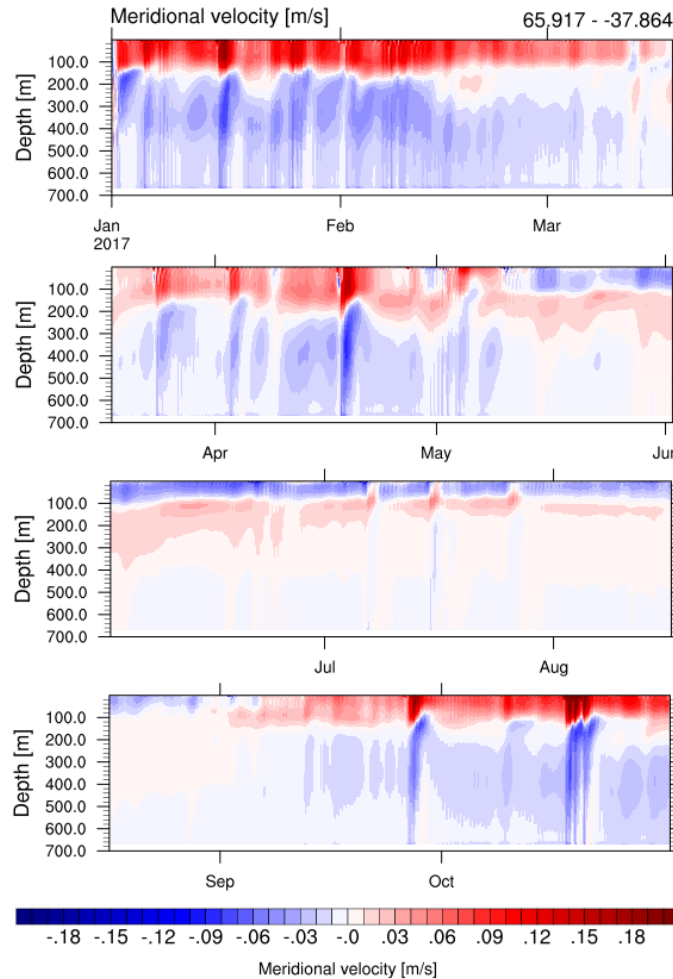
Figure 4.17: Meridional velocity obtained at point B in figure 2.8 from EXP A in table 2.10. Meridional velocity is positive northward.

The reversals produced by both EXP A and EXP C may be driven partially by periodic intensifications of the coastal current entering from the open boundaries (since they gain strength in EXP C with respect to EXP A) and partially by a forcing not linked with the open boundaries conditions frequency (being simulated by both EXP A and EXP C). EXP AWJUL was run with the same settings of EXP A but without the wind stress: the considered reversals are

clearly not reproduced in this simulation (figure 4.16(c)), proving that in EXP A they are due to the local wind. This explains why they're present in EXP A and why they're strengthened in EXP C, where both the local wind stress and the sub-monthly variations of the coastal current entering the eastern boundary are present.

Figure 4.18 shows the shelf currents at 20 m depth on 7 July (outputs average from 8:00 to 12:00) from EXP C - NEST 1, in correspondence with one of the reversals simulated by both EXP C and EXP A; figure 4.19, instead, represents the shelf currents during the estuarine fjord response to this surface inflow event (on 9 July, from 8:00 to 12:00). The coastal current entering the boundary weakens and detaches from the coast on 9 July with respect to 7 July, confirming the concurrence of the coastal current intensification in determining the reversal. The surface outflowing current joins with an anticyclonic recirculation current on the shelf during the estuarine fjord response.
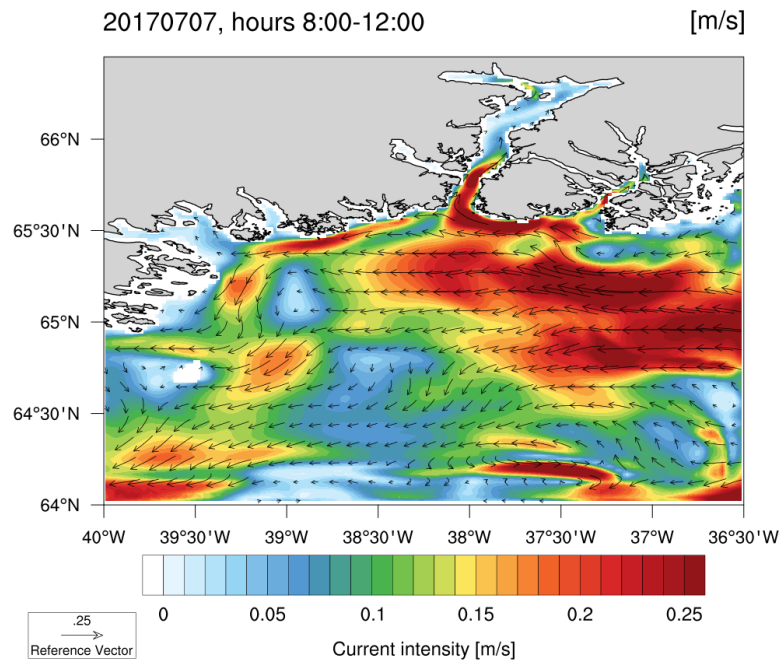
Figure 4.18: Shelf currents at 20 m depth, 7 July 2017, time average from 8:00 to 12:00, EXP C - NEST 1. The arrows components are given by the time averages of the hourly zonal ($\overline{u}$) and meridional ($\overline{v}$) velocity outputs at each point, while the colours indicate current intensity computed as the time average of the hourly outputs intensity at each point: $\overline{(u^2 + v^2)^{\frac{1}{2}}}$, where the overline indicates the time average.

Figure 4.20 shows, instead, the shelf currents at 20 m depth during one of the reversals that are present in EXP C but not in EXP A (12 July 12:00-16:00): the coastal current that drives this surface inflow is much weaker than the one

Figure 4.19: Shelf currents at 20 m depth as in figure 4.18, 9 July 2017, time average from 8:00 to 12:00, EXP C - NEST 1.

associated to the previously analysed reversal.
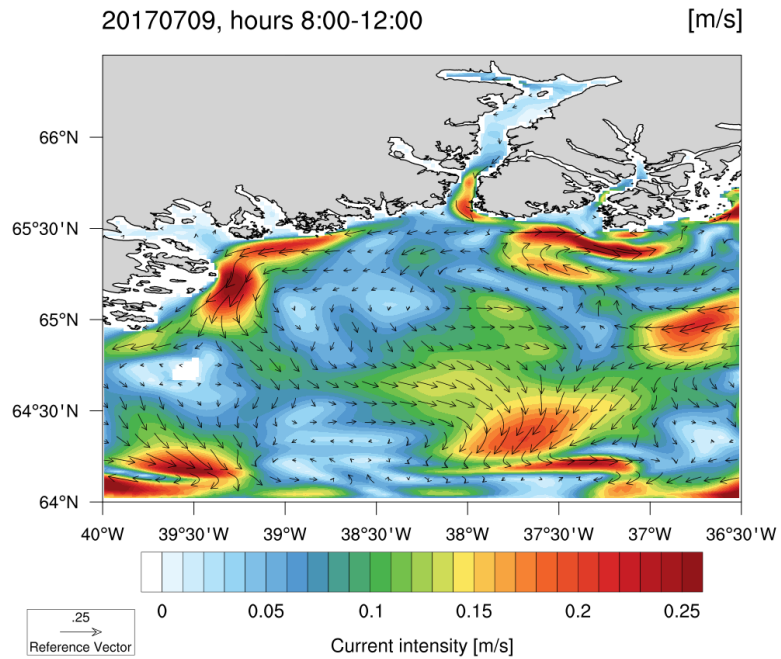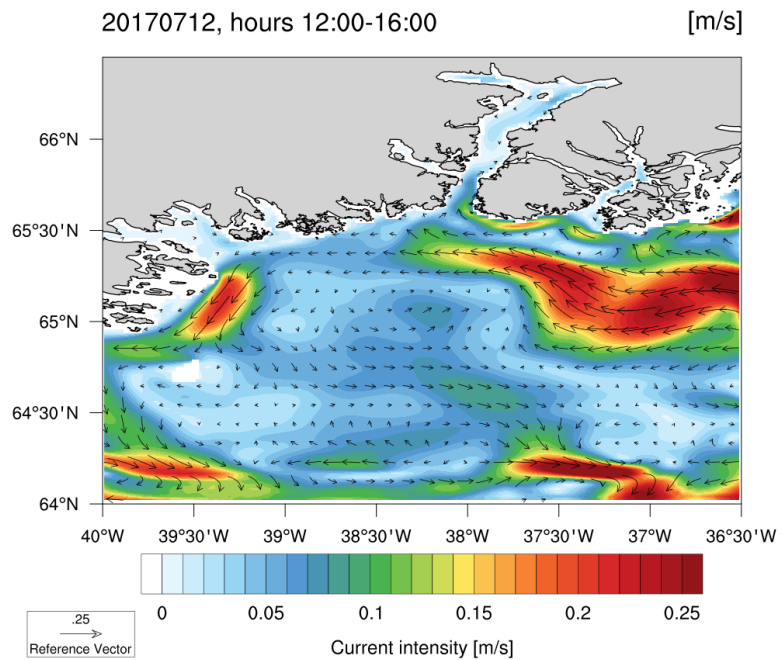

Figure 4.20: Shelf currents at 20 m depth as in figure 4.18, 12 July 2017, time average from 12:00 to 16:00, EXP C - NEST 1.

Particularly interesting is the shelf currents behaviour in correspondence of the strong surface outflow on 23 July: an anticyclonic eddy facilitates the surface outflow, stabilizing at the fjord mouth for approximately a week till the end of the simulation (figure 4.21).

The presence of this eddy and of the anticyclonic region near the coast in figure 4.19 confirms the characteristics of the summer shelf circulation that were also present in the monthly forced simulation (EXP A, see chapter 3): with respect to the winter case, summer circulation is clearly more variable, the shelf-near coastal circulation is eddy intensified, and both local wind and coastal current intensifications contribute to the intermediary circulation.
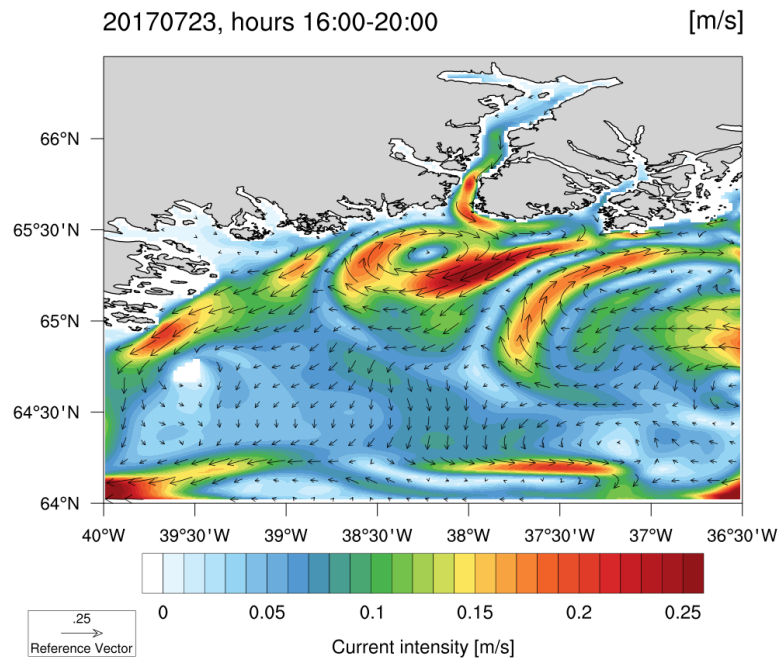
Figure 4.21: Shelf currents at 20 m depth as in figure 4.18, 23 July 2017, time average from 16:00 to 20:00, EXP C - NEST 1.

EXP C - NEST 2 shows a strengthening of the currents with respect to NEST 1, as happens to EXP B in winter (see section 4.1), but also the disappearance of one of the reversals that are added by EXP C - NEST 1 to the ones of EXP A and a reduction of the intensity of another one of these under ~ 30 m depth (see figure 4.22). The structure of the reversals, however, is much better defined in EXP C - NEST 2 with respect to NEST 1; in particular, the sub-surface inflows and outflows are stronger and better defined.

As with the winter simulation, we can analyse current intensity and pycnocline fluctuations amplitude at increasing distance from the fjord head: figure
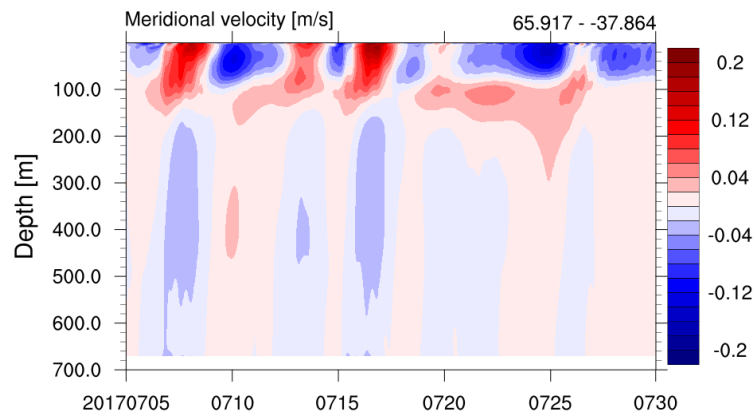
(a)
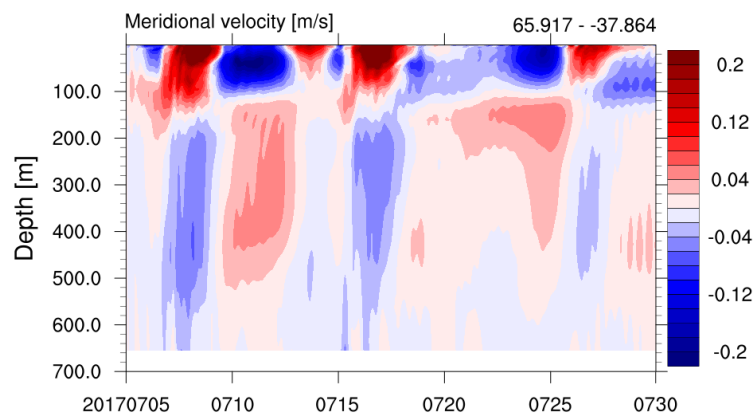
(b)

Figure 4.22: Meridional velocity obtained at point B in figure 2.8 from EXP C - NEST 1 (4.22(a)) and from EXP C - NEST 2 (4.22(b)). Meridional velocity is positive northward.

4.23 represents meridional velocity (or the opposite of zonal velocity when it's a better approximation of along-fjord velocity) and potential density at points A and C in map 2.8. Approaching the fjord head, current intensity diminishes
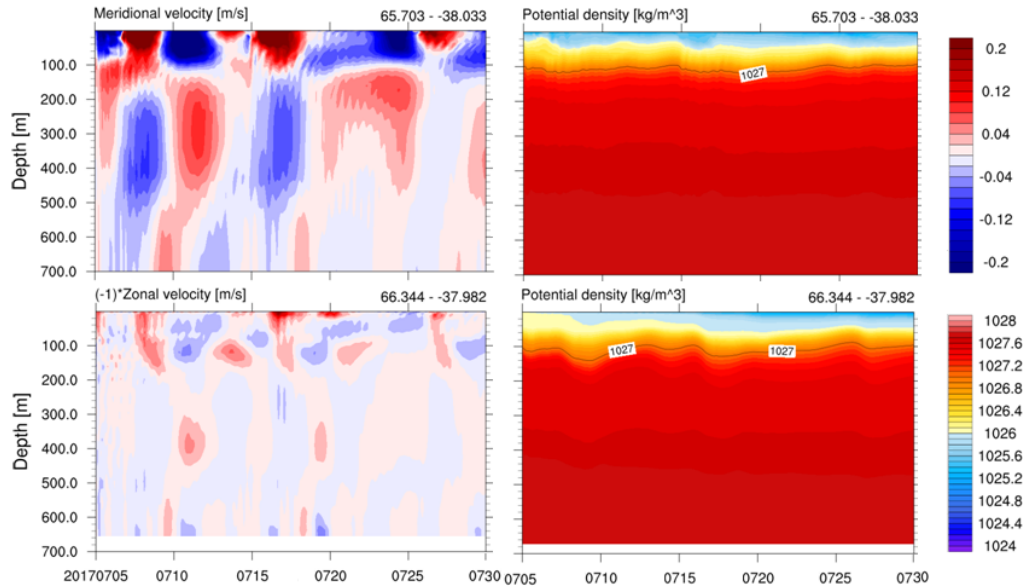
Figure 4.23: Meridional velocity (or the opposite of zonal velocity when it's a better approximation of along-fjord velocity) and potential density from EXP C - NEST 2 at points A (top panel) and C (bottom panel) in figure 2.8. The black line superimposed on the potential density graphs indicates the pycnocline depth, where the pycnocline is identified with the 1027 kg/m^3 isopycnal following Jackson et al. (2016).

while the amplitude of pycnocline fluctuations grows, as happens in winter. The reduction or growth are progressive, as shown by some Hovmöller plots at locations in between points A and C. This is consistent with what has been measured by Jackson et al. (2016) and to the simulations results of Jackson et al. (2018).

4.2.1   Heat and salt transports

Are the intermediary circulation reversals affecting water properties near Helheim glacier also in summer?

We have already shown that pycnocline fluctuations are amplified toward the fjord head (figure 4.23), but these amplitudes are far smaller than the ones observed in winter (see section 4.3); therefore one may ask what is the extent of the water properties fluctuations that current reversals may induce in the northern part of the fjord in this season.

In order to answer these questions, we compute again the heat ($H_t(t)$) and salt

($S_t(t)$) transports through sections 0, 1, 2, 3 and 4 in figure 4.8 from the EXP C - NEST 2 outputs, exactly as done in section 4.1.1. Figure 4.24 represents these transports and compares them with the meridional velocity Hovmöller plot at point A (in map 2.8). As in winter, there's good correspondence between
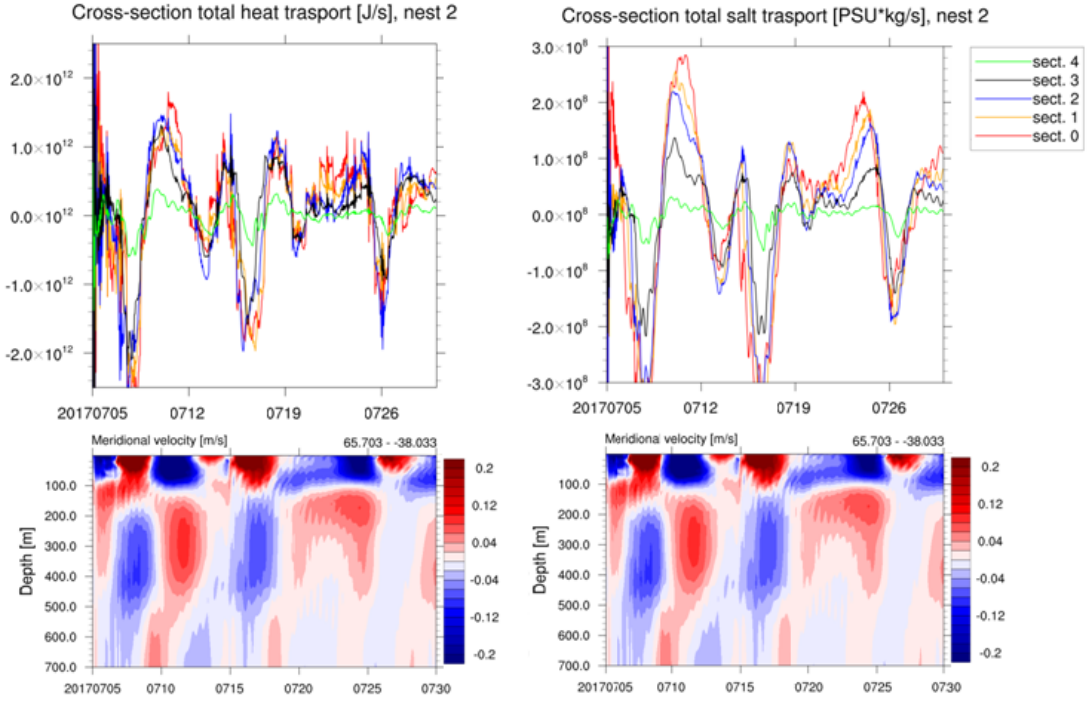
Figure 4.24: Heat and salt transports through the sections in figure 4.8 obtained from EXP C - NEST 2. They are compared with the meridional velocity Hovmöller plot at point A in figure 2.8 from the same simulation. Meridional velocity is positive northward; transports are positive towards the fjord head.

the transports sign and the current directions distribution: positive transports match with surface outflow and deep inflow, while negative transports occur with surface inflow and deep outflow. Transports fluctuations, therefore, are again driven by intermediary circulation.

In figure 4.25, the cumulative time integrals of the transports ($\int_0^t H_t(t')dt'$ and $\int_0^t S_t(t')dt'$) are compared to the averages of potential temperature and salinity over the volume V (highlighted in light-blue in figure 4.8). Considering sections 0, 1 and 2 from the 14th to the 25th of July, the integrated salt transports appear to be more correlated to the volume averaged salinity than the integrated heat transports are to the average temperature. Moreover, while the volume averaged temperature shows a mean warming trend, the integrated heat transports are mostly negative at least until the 23rd of July (excluding
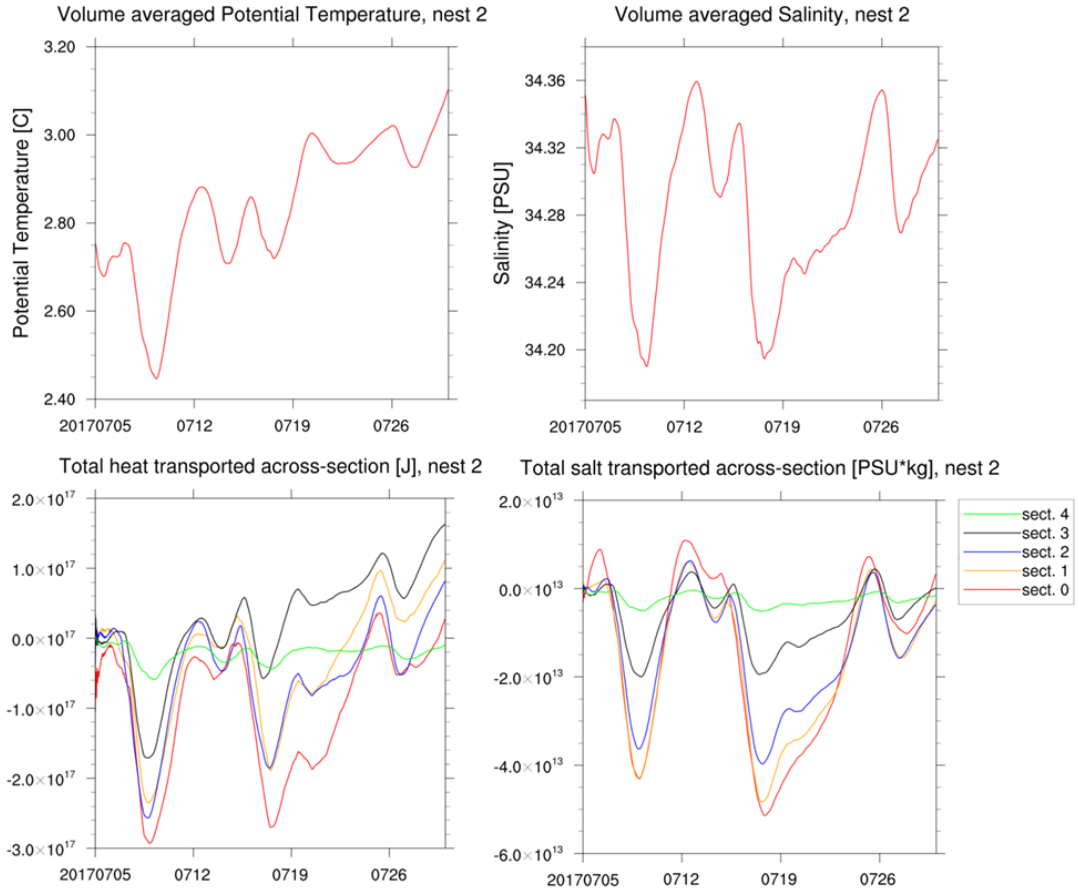
Figure 4.25: Comparison between the cumulative time integrals of the heat and salt transports in figure 4.24 (bottom panel) and the volume averages of potential temperature and salinity in the fjord volume highlighted in light-blue in figure 4.8 (top panel), EXP C - NEST 2.

section 3). A negative integrated transport means that, from the beginning of the simulation till the considered time, there has been a net advective removal of heat from the volume delimited by the considered section. Section 4 integrated heat transport being always negative implies that, in case of absence of other heat sources, the average temperature in V should not be increasing with time, but it should remain smaller than the initial value during all the simulation.

These discrepancies are also reflected in the values of the lagged correlations between the cumulative time integrals of the heat transports, $\int_0^t H_{t-section\ x}(t')dt'$, and the total heat storage in volume V, $H_s(t)$ (figure 4.26): the correlation is greatest for section 3 (that coherently shows the most positive integrated transport) and it is less than 0.68 for sections 0 and 4. Furthermore, these correlations do not peak at increasing lags from section 4 to section 0, as one
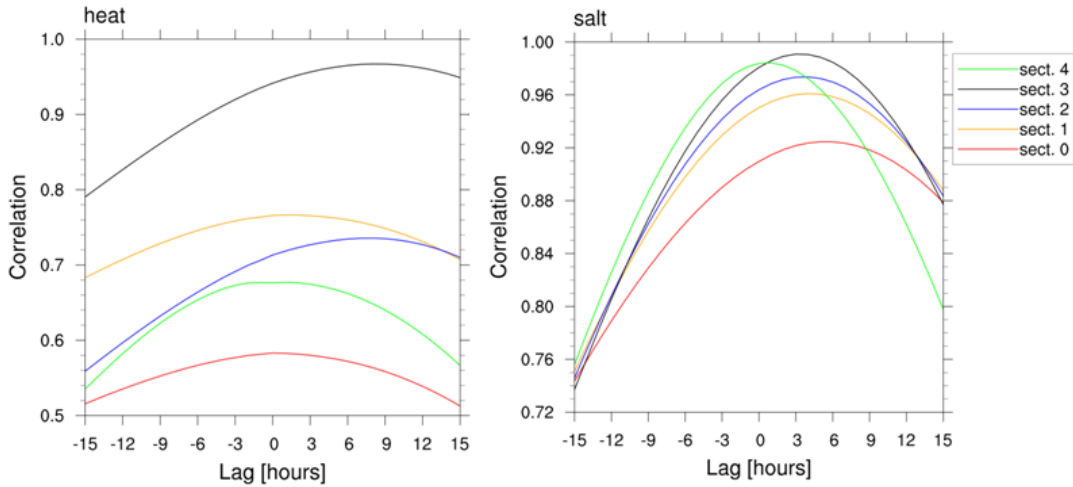
Figure 4.26: Lagged correlations between the cumulative time integrals of the heat (salt) transports in figure 4.24 and the total heat (salt) storage in the fjord volume highlighted in light-blue in figure 4.8, EXP C - NEST 2.

would expect if the mean temperature trend in V was only driven by the advective heat fluxes from the shelf (as happens, instead, in the non-summer case). We can therefore conclude that, near the glacier, water temperature shows some fluctuations clearly linked with nearly simultaneous fluctuations in the integrated heat transport through section 0 (which justify a correlation greater than 0.5, see figure 4.25), but these are superimposed on a mean warming trend that should be attributed to another heat source. This source has to be searched in surface fluxes, since they are also present in the heat balance equation for volume V (equation 4.3): figure 4.27 shows, indeed, a progressive heating of a thin surface layer at point C (thus inside the considered volume), which justifies the observed underlying warming trend. The greatest warming happens at the same time as the mayor discrepancy between section 0 integrated heat transport and volume averaged temperature (between 15 July and 21 July).

Despite of this mean warming trend, we can take as lower limits of the temperature fluctuations provoked by intermediary circulation the changes toward smaller temperature values in figure 4.25. The greatest one of these changes is associated with the first surface inflow simulated by the second nested model (7 and 8 July) and it is of 0.3°C.

As far as salinity is concerned, the correlations in figure 4.26 are nearly as high as the ones obtained with EXP B, as one would expect since surface fluxes do not appear in the salt conservation equation for volume V (equation 2.5). Thus, the volume averaged salinity fluctuations in figure 4.25 are almost com-
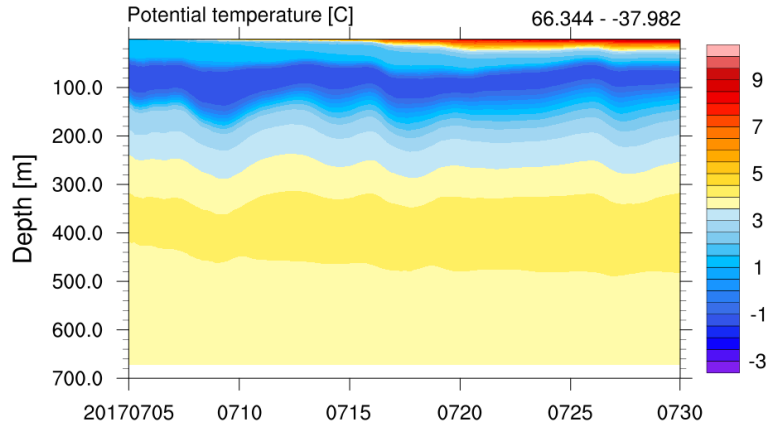
Figure 4.27: Potential temperature Hovmöller diagram at point C in figure 2.8, EXP C - NEST 2.

pletely driven by the advective salt transport through the fjord mouth. Being the transport given by the intermediary circulation reversing currents (figure 4.24), also the salinity fluctuations are driven by intermediary circulation and they are up to ~ 0.16 PSU.

In conclusion, intermediary circulation is capable of inducing temperature and salinity fluctuations in the waters near Helheim glacier also in summer. These are of order 0.1°C and 0.1 PSU, being smaller than the winter ones, as one would expect from the reduced intensity of summer intermediary flows (further analysis in section 4.3).

Unfortunately, we can't compare the effects of this circulation to the ones of glacier-driven circulation, lacking in our nested models the presence of ice.

4.3 Winter and summer comparison

From the comparison of the meridional velocity Hovmöller plots at point A from EXP B - NEST 2 and EXP C - NEST 2, clearly emerges that current intensity is much greater in winter than in summer. The inflowing intensity peaks are nearly equivalent, but, in summer, they are confined at depths shallower than ~ 30 m. Moreover, in our simulations, the summer greatest outflowing intensity does not reach the winter peak outflowing intensity and, while in winter the deeper layer intensities nearly equal the surface intensities, in summer the deeper layer shows a considerable intensity reduction (even of an order of magnitude with respect to surface and to winter deep flows). This confirms the reduction in Sermilik fjord summer intermediary circulation intensity that was already found by Jackson et al. (2016) with moored observations (see fig.1.9).
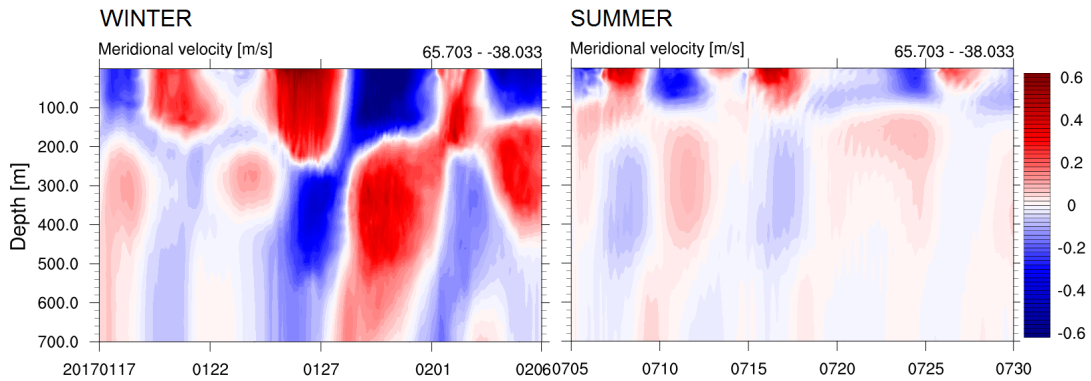
Figure 4.28: Meridional velocity obtained at point A in figure 2.8 from EXP B - NEST 2 (on the left) and EXP C - NEST 2 (on the right). Meridional velocity is positive northward.

The frequency of the principal surface inflow events (not the 13 July one that is clearly a minor event: compare figure 4.18 and figure 4.20) appears to be slightly reduced in summer with respect to winter, as also observed by Jackson et al. (2016).
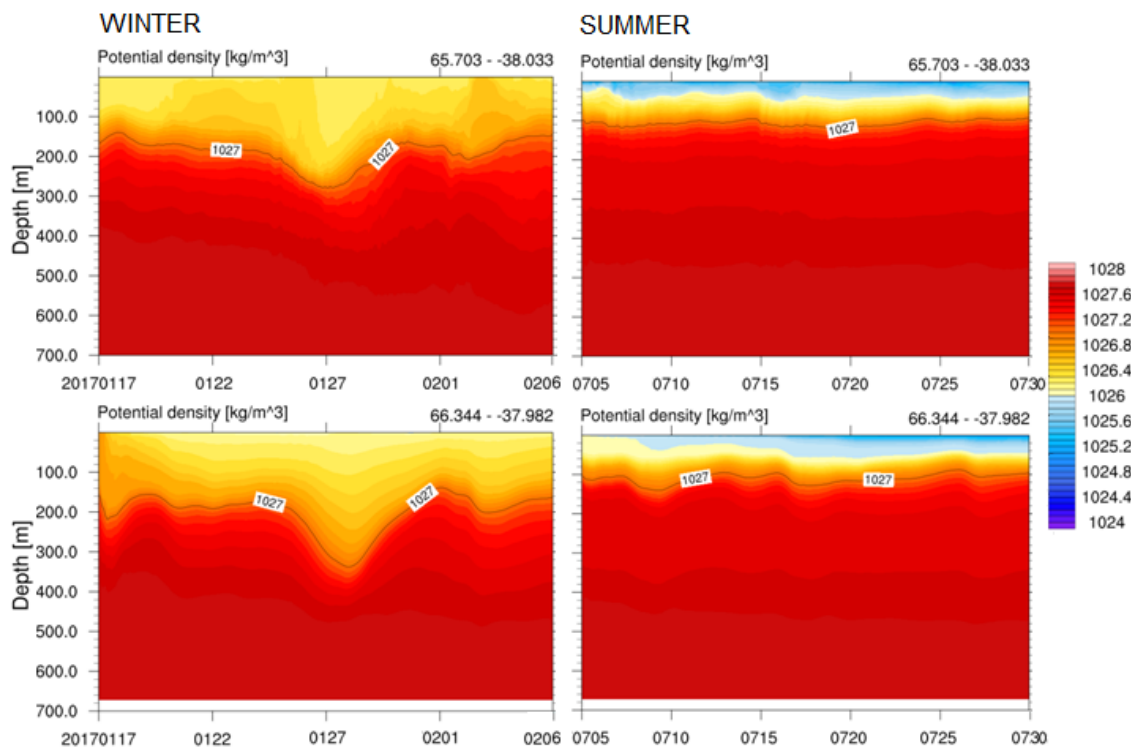
Figure 4.29: Potential density obtained at point A (top panel) and at point C (bottom panel) in figure 2.8 from EXP B - NEST 2 (on the left) and from EXP C - NEST 2 (on the right).

In summer the depth of the reversals is ~ 100 m; in winter, instead, when the strongest events happen, the surface inflow extends beyond 200 m depth.

WINTER   SUMMER

Cross-section total heat trasport [J/s], nest 2

Cross-section total salt trasport [PSU*kg/s], nest 2

Volume averaged Potential Temperature, nest 2

Volume averaged Salinity, nest 2
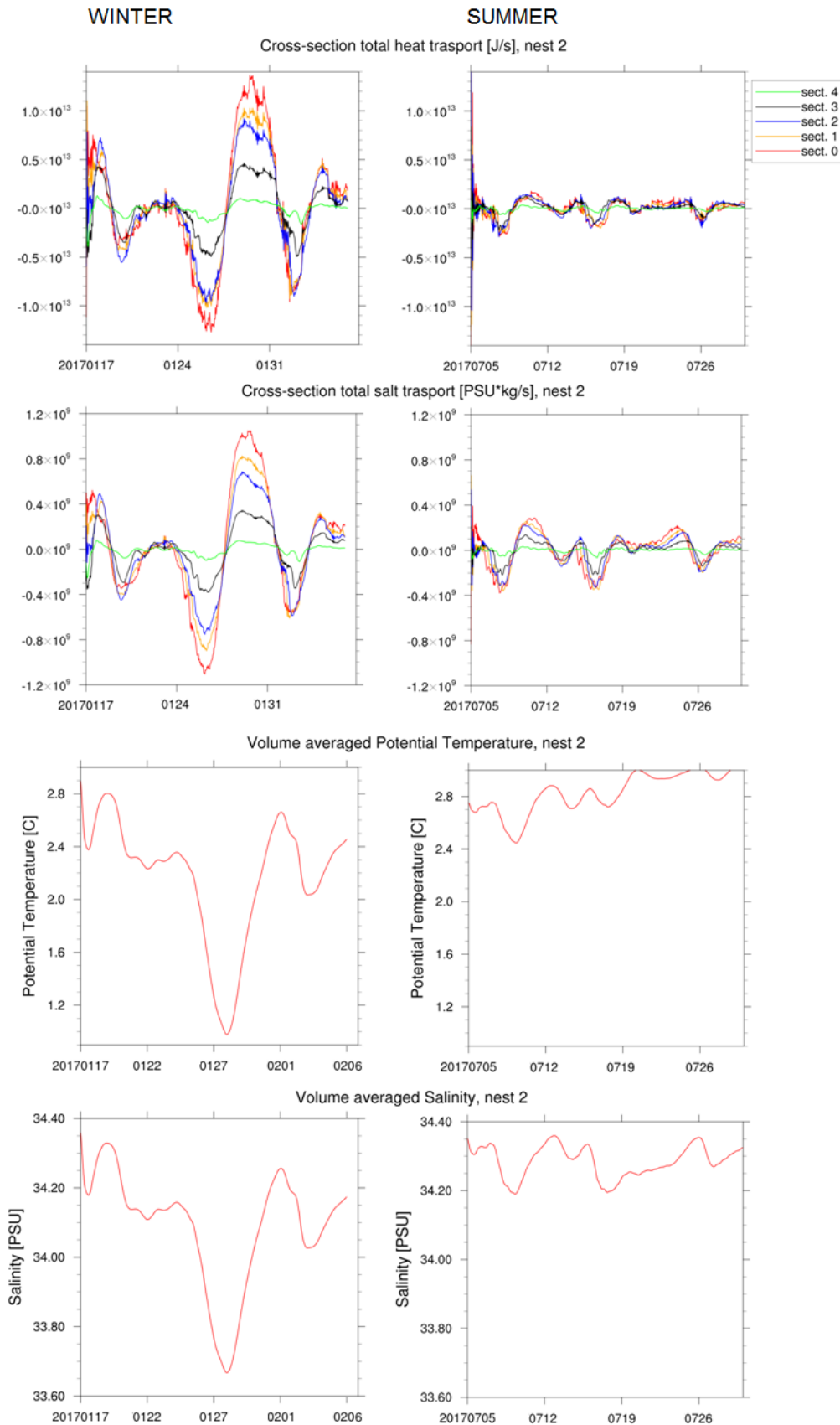
Figure 4.30: Heat and salt transports through the sections represented in figure 4.8, positive towards the fjord head, and volume averages of potential temperature and salinity over the fjord volume highlighted in light-blue in figure 4.8, EXP B - NEST 2 (on the left) and EXP C - NEST 2 (on the right).

The reversals depth coincides with the pycnocline depth in both the seasons, as shown in figure 4.29, where the pycnocline clearly appears to be much deeper in winter than in summer, probably as a consequence of different mixing regimes. Furthermore, winter pycnocline fluctuations are much more accentuated than summer ones, up to ten times greater, as expected from the huge differences already found in current intensities.

As in summer current intensity and pycnocline fluctuations amplitude diminish, also does the magnitude of heat and salt transports (figure 4.30).
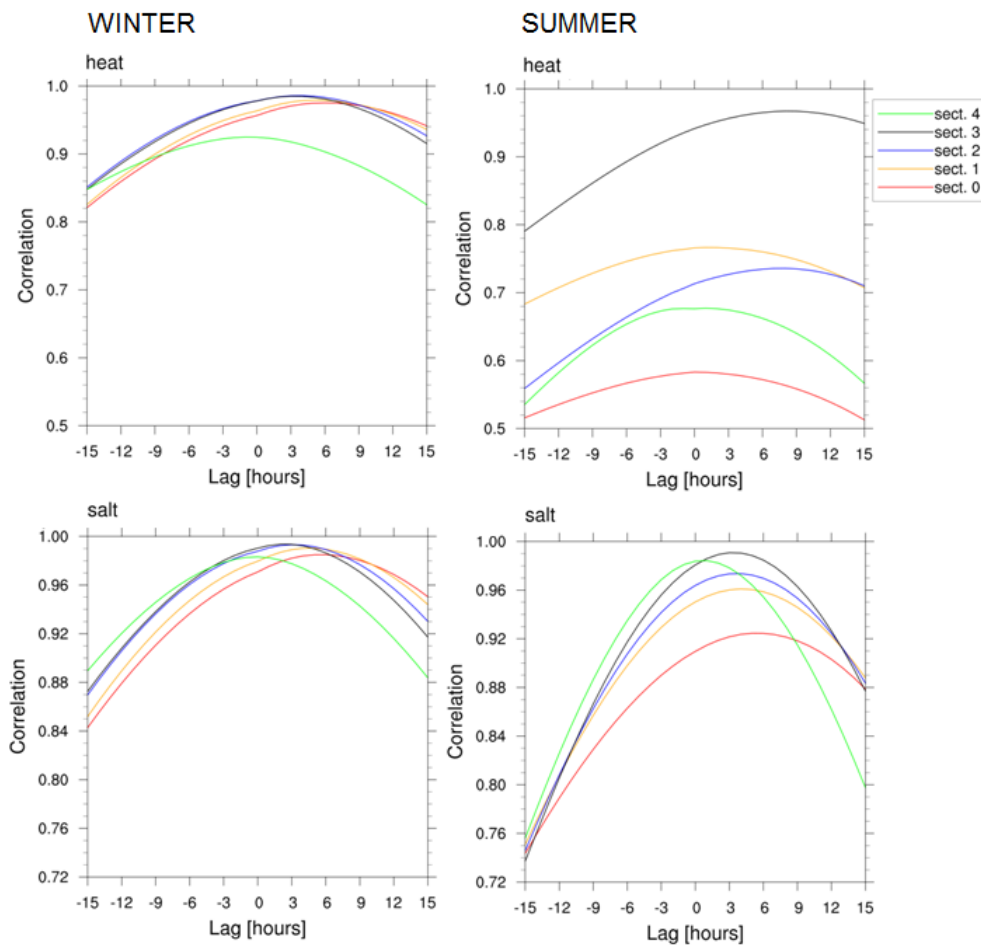
Figure 4.31: Lagged correlation between the cumulative time integrals of the heat (salt) transports in figure 4.30 and the total heat (salt) storage in the fjord volume highlighted in light-blue in figure 4.8, EXP B - NEST 2 (on the left) and EXP C - NEST 2 (on the right).

The heat and salt transports reduction suppresses the extent of the changes in the mean water properties near the fjord head: while the smallest winter fluctuations of temperature and salinity averaged over the fjord volume near Helheim glacier are approximately comparable with the greatest of summer sea-

son, the winter largest fluctuation is $\sim 3 - 4$ times the summer largest (figure 4.30). Unfortunately we have simulated only one of these particularly energetic events happening in winter, being thus not able to assess their frequency.

The much greater effectiveness of intermediary circulation in changing fjord water properties in winter is also reflected in the reduction from winter to summer of the correlations between the cumulative time integrals of the transports and the total heat or salt storage in V (figure 4.31). This reduction is particularly evident as far as heat is concerned, since the heat balance in summer is strongly affected not only by the advective transports from the shelf, but also by surface fluxes, as pointed out in section 4.2.1.

4.4 Cross-fjord variations
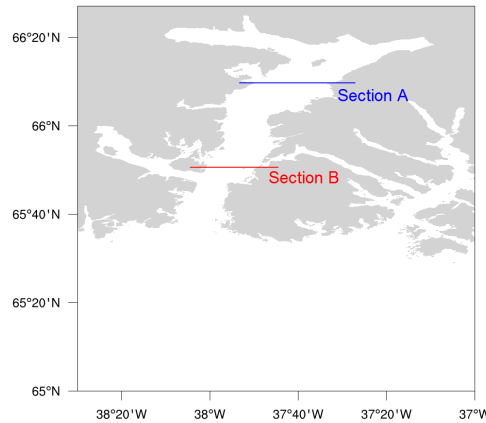
Figure 4.32: Sections used to study cross-fjord variations of water properties and current direction.

The high resolution of the second nested model allows to study the three dimensional characteristics of intermediary circulation: while NEST 1 represents this circulation as a two-layer flow with little cross-fjord gradients, NEST 2 shows non-negligible cross-fjord variations in currents patterns and pycnocline depth (see figures 4.33 and 4.34 representing meridional velocity from EXP B - NEST 1 and EXP B - NEST 2 on sections A and B in figure 4.32).

Generally, in the second nested simulations, EXP B - NEST 2 and EXP C - NEST 2, the fjord shows a two layer current structure, characterised by an interface depth linearly varying over the fjord width: the surface inflow slightly approaches the eastern side of the fjord, generating lateral shear, and the pycnocline deepens on this side with respect to the other. Conversely, the surface outflow gets closer to the western side of the fjord, with an opposite tilt of the

Figure 4.33: Daily averaged meridional velocity and potential density from EXP B - NEST 1 and EXP B - NEST 2 on section B in figure 4.32. A surface inflow event and an estuarine fjord response are represented.

pycnocline (figure 4.33). The direction of the cross-fjord pycnocline tilt is in agreement with the one that would be associated to the observed vertical velocity shear in the thermal wind equation (here the horizontal density gradient is given by the salinity difference between the two layers); the surface currents leave the coast to their right, as expected from a coastal baroclinic flow (see figure 3.19). These changes in the cross-fjord slope of the pycnocline (deepening towards the eastern or western side of the fjord) are superimposed on the cross-fjord uniform vertical heaving (shown e.g. by the Hovmöller plot in figure 4.1, since point B is roughly on the fjord central axis, thus experiencing a pycnocline vertical displacement that's approximately an average over the

fjord width[13]).

The cross-fjord variation of pycnocline depth is of the order of the one estimated by Jackson et al. (2016) assuming the along-fjord velocity to be in geostrophic balance and considering a velocity shear of $\sim 0.3 \frac{m}{s}$[14]: 30 m. Actually, our strongest intermediary circulation event (whose estuarine part is represented in figure 4.33 - 29 January), with a vertical shear $> 0.6 \frac{m}{s}$ (see figure 4.6(b)), correctly shows a cross-fjord pycnocline depth variation between 50 and 100 m (at section B in figure 4.32, see potential density on 29 January in figure 4.33). Thus, near the fjord mouth, where the vertical shear is greater and the amplitude of pycnocline heaving is smaller, the cross-fjord pycnocline tilt is not negligible with respect to the mean vertical displacement on which it is superimposed.

From the analysis of the currents at 20 or 120 m depth (figures 4.34 and 4.35), clearly emerges that in the broader parts of the fjord the current structure is definitely three dimensional: sometimes the flow completely reverses across the fjord width, with surface velocity directed northward on the eastern side of the fjord and southward on the western, leaving the coast always to the right. These occasional cross-fjord reversals happen at times of weak velocity, exactly as in the simulation performed by Jackson et al. (2018). In correspondence with the narrowest parts of the fjord, instead, the current maintains a uniform direction throughout all the fjord width, with a prevalence of a two-dimensional (along-fjord direction and depth) current pattern. This is true for both the summer and winter seasons, confirming the results of Jackson et al. (2018), who placed Sermilik fjord on a borderline between fjord geometries which adapt to a standing wave two dimensional description of the intermediary flows dynamics and ones that need a three dimensional internal Kelvin wave dynamics modelling (see figure 4.36), depending on the ratio of the fjord width to the internal radius of deformation.

---

[13]since the pycnocline depth varies approximately linearly over the fjord width.
The increase of the amplitude of pycnocline depth fluctuations approaching the fjord head shown in figures 4.7 and 4.23 is not due to the slight displacement off-centre of point C, since in this part of the fjord the cross-fjord pycnocline tilt is actually absent, as a consequence of the reduction of the fjord width and of the vertical velocity gradient.

[14]Using the thermal wind balance for a two layer system (Margules relation) to retrieve the interface slope associated to the given vertical shear: $f\frac{v_1-v_2}{g'} = \frac{\partial h}{\partial x}$, where $g' = -g\frac{\rho_1-\rho_2}{\rho_2}$ ($= 9.5 \cdot 10^{-3} \frac{m}{s^2}$ for Jackson et al.), 1 indicates the upper layer, 2 the deeper layer, v meridional velocity, ρ density, h the pycnocline depth (positive), x longitude, f the Coriolis parameter and g the gravitational acceleration. Assuming the pycnocline depth to vary linearly across the fjord, the cross-fjord pycnocline depth variation is given by $\frac{\partial h}{\partial x}$ multiplied by the fjord width (~ 7 km).
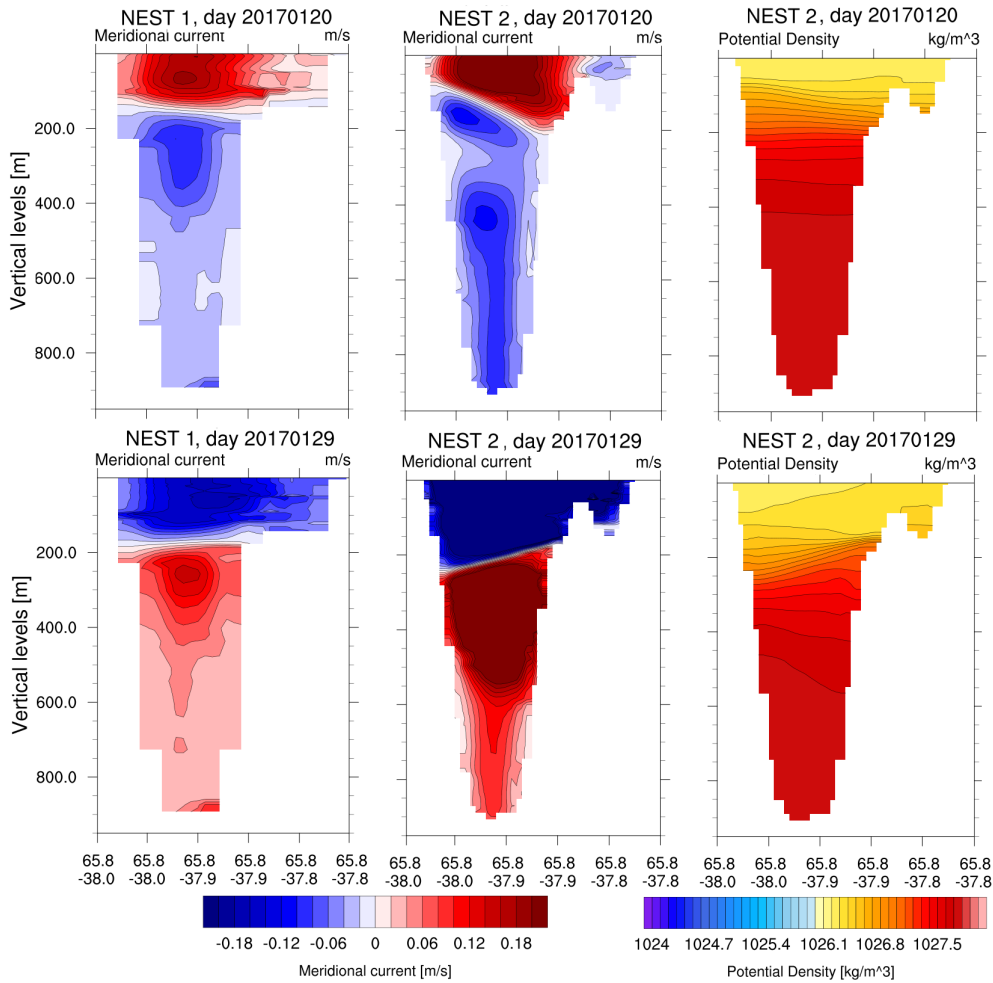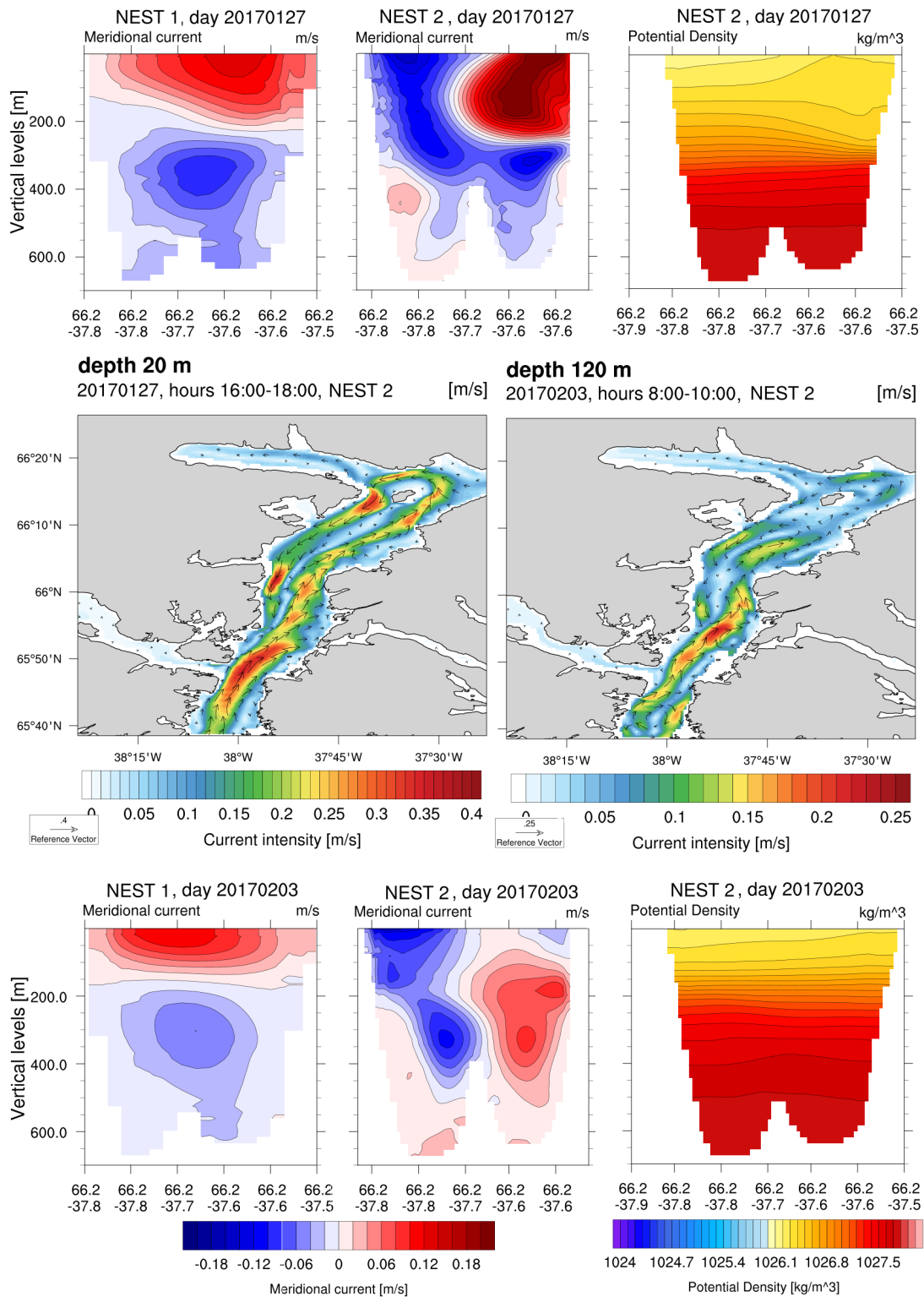
Figure 4.34: Daily averaged meridional velocity and potential density from EXP B - NEST 1 and EXP B - NEST 2 on section A in figure 4.32; two-hour averaged currents at 20 and 120 m depths from EXP B - NEST 2, computed as in figure 4.4. Two winter episodes of cross-fjord reversal are represented.
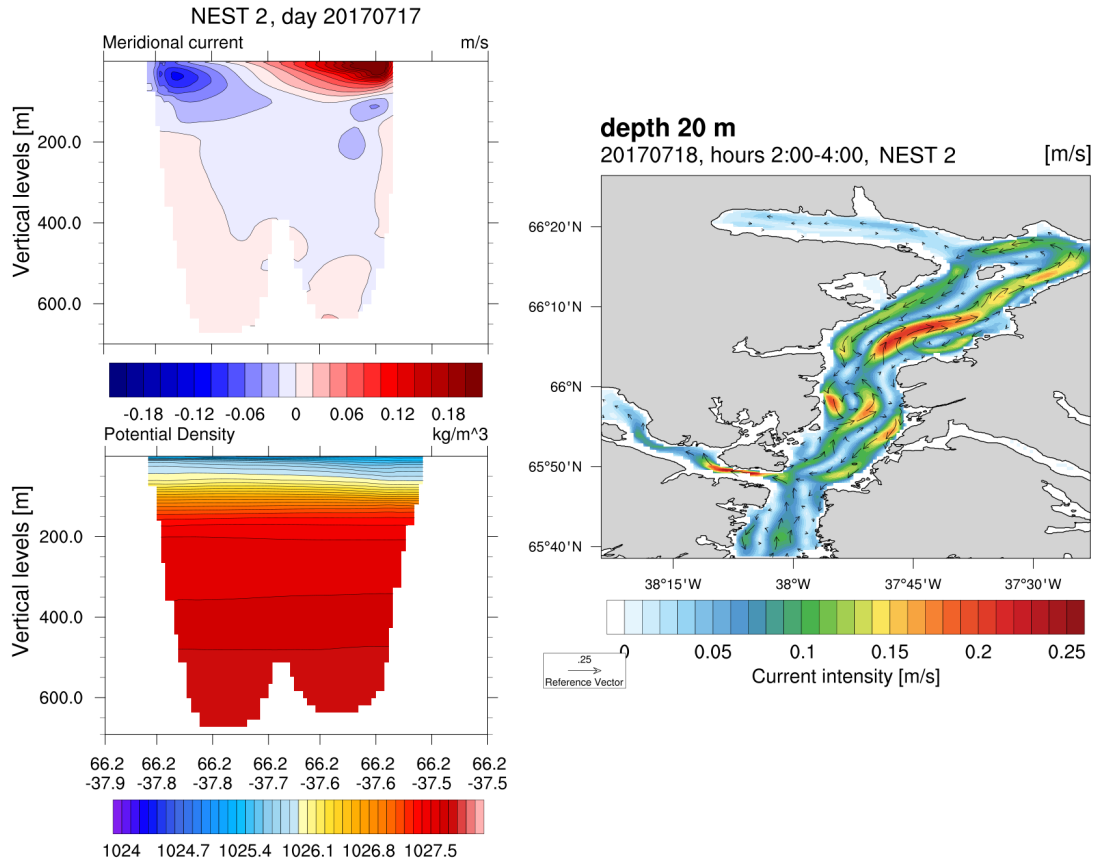
Figure 4.35: Daily averaged meridional velocity and potential density from EXP C - NEST 2 on section A in figure 4.32; two-hour averaged currents at 20 m depth from EXP C - NEST 2, computed as in figure 4.4. A summer episode of cross-fjord reversal is represented.

During the times of weak current intensity, the circulation is rather complex, showing the presence of numerous eddies (see the currents at fixed depths in figures 4.34, 4.35 and 4.37). Moreover, at times, both in winter and summer, the current pattern appears to be extremely variegated, with surface velocity directions opposed to the ones described in the previous paragraph, that are instead restored at major depth (see figure 4.37). These dynamical structures are obviously of higher order than the ones described in Jackson et al. (2018): their presence in our model demonstrates the power of the downscaling technique in reproducing extremely fine dynamics, thanks to the progressive increase of spatial and temporal resolution.
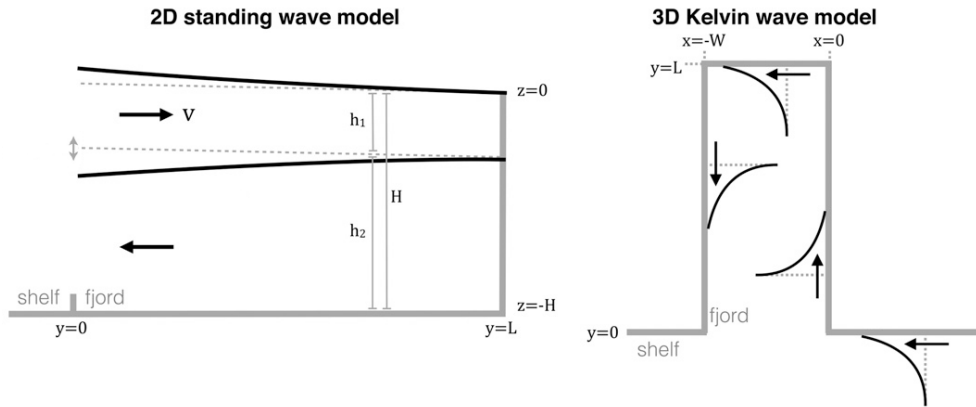
Figure 4.36: On the left, schematic of the 2D standing wave model described by Jackson et al. (2018), showing depth vs along-fjord direction. On the right, schematic of the 3D Kelvin wave model, showing plan view of fjord and shelf. The amplitude of the interface displacement is projected onto the along-shore direction, illustrating the cross-shore decay of the Kelvin wave structure. Reproduced from Jackson et al. (2018).
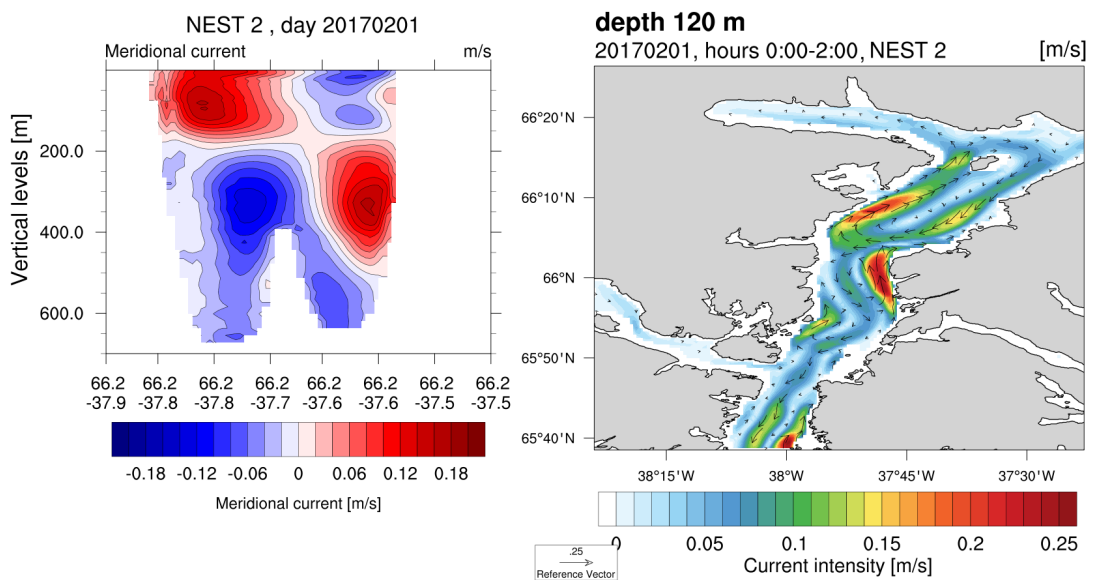
Figure 4.37: Daily averaged meridional velocity from EXP B - NEST 2 on section A in figure 4.32; two-hour averaged currents at 120 m depth from EXP B - NEST 2, computed as in figure 4.4. A winter episode of double cross-fjord reversal is represented.

CHAPTER 5

Conclusion

In this thesis, a high resolution nested ocean model has been used to simulate Sermilik fjord dynamics on daily and seasonal temporal scales.

First of all, the thesis developed a nudging layer parametrization for the lateral open boundary conditions that was never used before. This allows to nest limited area regions of the world ocean into coarser global models preventing instabilities to grow at the boundaries. The SURF modelling platform was never used before to simulate for longer than few weeks and now the simulation was stable at least for ten months.

An extensive post-processing analysis was then performed on the model outputs, including the analysis of the correlations to assess the salt and heat transport processes occurring in the fjord.

From a ten-month Sermilik fjord dynamics simulation the presence of a seasonal mode of fjord circulation has emerged that has never been documented before, likely as a consequence of the presence of larger amplitudes circulation modes in the observational data. This seasonal circulation mode consists of a two-layer flow: water enters the fjord in a surface layer and exits it in a deeper one from the end of September to the beginning of May, i.e. the winter circulation is anti-estuarine; on the contrary, the summer current directions are reversed, with a surface outflow and a deeper inflow i.e. an estuarine circulation. This seasonal reversal is a consequence of the seasonal circulation changes on the shelf, which are probably due to the seasonal variations of the wind stress curl intensity on the SPNA, affecting the strength of the East Greenland Coastal Current (EGCC). This link with the basin-scale circulation should be further demonstrated in a future study, through the analysis of the global model (GOFS16) outputs and of the wind forcing seasonal variations. Moreover, our model proves that the EGCC effectively influences Sermilik fjord water, being in huge proximity to the coast, making the fjord and the first few tens of kilometres from the coast extremely similar to a ROFI region, with the fresher water carried by the coastal current.

Through Sermilik ford circulation analysis on a daily time-scale, we demon-

strated that intermediary circulation has a non-local forcing, being driven by the shelf circulation synoptic temporal variability and at least mesoscale spatial variability. This poses some constraints on the spatial domain that must be included in ocean models aimed at simulating intermediary circulation in Sermilik fjord and, also, on the temporal frequency of the outputs of coarse resolution climate models that ought to be used to downscale future climate scenarios. To reproduce intermediary circulation, a shelf area greater than our first nested model domain (80 km to the east of the fjord mouth - upstream the coastal current) must be simulated directly or through downscaling (as in our case); to explore the intermediary circulation and its long-term changes effects on the GrIS through nested limited area models on a climatic time-scale, the coarse resolution climate models must produce daily outputs. Up-to-date climate models monthly storage of the outputs must be improved to a daily storage.

Thanks to the high resolution obtained from the limited area modelling, the influence of intermediary circulation on temperature and salinity of the fjord waters in proximity to Helheim glacier terminus has been studied: in winter intermediary circulation can force temperature fluctuations of 1.5°C and salinity changes of 0.6 PSU on average over a fjord volume near to the glacier. This demonstrates that the shelf-forced flows are able to exert a strong influence on the glacier, despite of the complex geometry and bathymetry of the fjord, actually with an amplification of the water properties fluctuations towards the fjord head. Our model is the first one that conjugates a realistic representation of the shelf circulation variability, necessary to fully reproduce intermediary circulation dynamics, with a high resolution bathymetry and fjord geometry: this is achieved through downscaling, which allows to simultaneously represent a wide range of scales (from the few hundred meters at the fjord head, to the thousands of kms of the SPNA) without having to build large-scale models with computationally unfeasible high resolutions.

The changes of intermediary circulation characteristics from winter to summer were also investigated: in summer the shelf-forced flows weaken, with slower current velocities and smaller amplitudes of the associated PW-AW pycnocline depth fluctuations. The consequent fluctuations of water properties at the fjord head are also reduced to an order 0.1°C and 0.1 PSU.

Thanks to the realistic representation of fjord geometry, we have proven that, in the narrowest parts of the fjord, intermediary flows are configured as a nearly-2D two-layer dynamics, while in the broader parts they show a 3D structure, which can be regarded as internal Kelvin wave dynamics, with occasional cross-

fjord reversals of currents direction.

Unfortunately, our simulations of intermediary circulation only cover brief periods of time (less than a month), thus representing just 4-5 reversals each. Therefore, it will be necessary to set up longer simulations (with GOFS16 daily outputs as open boundaries conditions, depending on the availability of GOFS16 analyses, currently one year), in order to obtain a broader statistic of reversals, so as to assess their average properties. This could be particularly useful for finding a climate downscaling strategy to the fjord from up-to-date coarse resolution climate models: being the intermediary circulation forcing absent from the monthly outputs of these models[1], intermediary circulation could be generated in a nested limited area model by superposing to the monthly open boundaries conditions (from the climate model outputs) a signal retaining the essential characteristics of the forcing wanted, since, in observational data (see e.g. Jackson et al. (2014)), intermediary circulation shows great regularity and reproducibility in time. The availability of a longer simulation would allow us to further demonstrate this regularity and to identify the right characteristics to assign to this imposed intermediary circulation forcing (e.g. an appropriate time frequency). Nonetheless, it should be noted that this approach could not account for any external influence or feedback governing the frequency of the forcing on a climatic time-scale: for example, since the number of cyclones happening along Greenland's coast is strongly affected by the NAO phase (see e.g. Li and Bromwich), a long-term trend of change of this pressure pattern could lead to a variation of the intermediary circulation time-scale and thus, maybe, to a modification of its effects on the glaciers retreat. In this case, setting up the appropriate sub-monthly variations in the open boundaries conditions would be way more challenging.

Our nested models don't include the glaciers terminating in Sermilik fjord, as well as sea-ice: inserting an ice model in SURF is a necessary future development. This would allow us to study glacier-driven circulation: we could quantify its ability to carry heat to the glacier and compare its heat-delivery efficiency to the intermediary circulation efficiency. We could analyse these two circulation modes separately from one another, removing the ice from the model in one simulation and applying monthly averaged open boundary conditions in another, or together, so as to study their interaction.

A one year simulation at 1/144° resolution would allow us to study how and how quickly the shelf water seasonal changes reach the fjord head, so as to estimate their impact on glaciers. This could be done considering only inter-

---

[1]Since it is characterised by a weekly time-scale.

mediary circulation (removing the ice from the model) or also glacier-driven circulation and adopting an approach similar to the Cowton et al. (2016) one: assigning a passive tracer to shelf waters and quantifying the time necessary for these waters to renew the water in a fjord volume near to the glacier. This could be analogously applied to the study of the time necessary for long-term changes in shelf water properties to reach the fjord head.

Bibliography

Aarseth I., Nesje A. and Fredin O. *West Norwegian fjords.* Geological Society of Norway (NGF), Trondheim, 2014. 2

Amundson J. M., Fahnestock M., Truffer M., Brown J., Luthi M. P. and Motyka R. J. Ice melange dynamics and implications for terminus stability, Jakobshavn Isbræ, Greenland. *J. Geophys. Res.*, 115: F01005, 2010. 10, 25

Andres M., Silvano A., Straneo F. and Watts D. R. Icebergs and sea ice detected with inverted echo sounders. *J. Atmos. Oceanic Technol.*, 32: 1042–1057, 2015. 23

Andresen C. S., Straneo F., Ribergaard M. H., Bjørk A. A., Andersen T. J. et al. Rapid response of Helheim Glacier in Greenland to climate variability over the past century. *Nature Geosci.*, 5: 37–41, 2012. 7, 22, 23

Arakawa A. and Lamb V. R. Computational design of the basic dynamical processes of the UCLA general circulation model. *Meth. Comp. Phys., New York: Academic Press*, 17: 173–265, 1977 35

Bamber J., van den Broeke M., Ettema J., Lenaerts J. and Rignot E. Recent large increases in freshwater fluxes from Greenland into the North Atlantic. *Geophys. Res. Lett.*, 39, L19501, 2012. 4, 12

Bellafiore D. and Umgiesser G. Hydrodynamic coastal processes in the north adriatic investigated with a 3D finite element model. *Ocean Dyn.*, 60: 255–273, 2010. 39

Bersch M., Yashayaev I. and Koltermann K. P. Recent changes of the thermohaline circulation in the subpolar North Atlantic. *Ocean Dyn.*, 57: 223–235, 2007. 5

Blayo E. and Debreu L. Nesting Ocean Models, in Ocean Weather Forecasting: An Integrated View of Oceanography. *Springer Netherlands, Chassignet E. P. and Verron J.*, ISBN 978-1-4020-4028-3, 127–146, 2006. 43, 44

Booij N., Ris R. C. and Holthuijsen L. H. A third generation wave model for coastal regions, part 1: model description and validation. *J. Geophys. Res.*, 104 (C4): 7649–7666, 1999. 39

Box J. E., Yang L., Bromwich D. H. and Bai L.S. Greenland ice sheet surface air temperature variability: 1840–2007. *J. Clim.*, 22: 4029–4049, 2009. 5

Breivik O., Mogensen K., Bidlot J. R., Balmaseda M. A. and Janssen P. A. Surface wave effects in the NEMO ocean model: forced and coupled experiments. *J. Geophys. Res. Oceans*, 120: 2973–2992, 2015. 39

Bromwich D. H. and Kurtz D. D. Katabatic wind forcing of the Terra Nova Bay polynya. *J. Geophys. Res.*, 89 (C3): 3561–3572, 1984. 25

Chen X., Zhang X., Church J. A., Watson C. S., King M. A., Monselesan D., Legresy B. and Harig C. The increasing rate of global mean sea–level rise during 1993-2014. *Nature Climate Change*, 7, 492–495, 2017. i, iii, 3

Chelton D., DeSzoeke R., Schlax M., El Naggar K. and Siwertz N. Geographical variability of the first baroclinic Rossby radius of deformation. *J. Phys. Oceanogr.*, 28, 433–460, 1998. 32

Chylek P., Folland C. K., Lesins G., Dubey M. K. and Wang M. Arctic air temperature change amplification and the Atlantic multidecadal oscillation. *Geophys. Res. Lett.*, 36, L14801, 2009. 7

Chu V. W. Greenland Ice Sheet hydrology: a review. *J. Prog. Phys. Geogr.*, 38: 19–54, 2014. 10

Chu V. W., Smith L. C., Rennermalm A. K., Forster R. R., Box J. E. and Reehy N. Sediment plume response to surface melting and supraglacial lake drainages on the Greenland ice sheet. *J. Glaciol.*, 55: 1072–1082, 2009. 10

Christoffersen P., Mugford R. I., Heywood K. J., Joughin I., Dowdeswell J. A. et al. Warming of waters in an East Greenland fjord prior to glacier retreat: mechanisms and connection to large–scale atmospheric conditions. *Cryosphere*, 5: 701–714, 2011. 8

Church J. A., White N. J., Konikow L. F., Domingues C. M., Cogley J. G., et al. Revisiting the Earth's sea-level and energy budgets from 1961 to 2008. *Geophys. Res. Lett.*, 38, 2011. 3

Cowton T., Slater D., Sole A., Goldberg D. and Nienow P. Modeling the impact of glacial runoff on fjord circulation and submarine melt rate using a new subgrid-scale parameterization for glacial plumes. *Geophys. Res. Oceans*, 120: 796–812, 2015. 11, 12, 16, 17, 26

Cowton T., Sole A., Nienow P., Slater D., Wilton D. and Hanna E. Controls on the transport of oceanic heat to Kangerdlugssuaq Glacier, East Greenland. *Journal of Glaciology*, 62(236): 1167–1180, 2016. 17, 20, 21, 101, 102, 130

Das S. B., Joughin I., Behn M. D., Howat I. M., King M. A. et al. Fracture propagation to the base of the Greenland Ice Sheet during supraglacial lake drainage. *Science*, 320: 984–986, 2008. 10

De Dominicis M. et al. A relocatable ocean model in support of environmental emergencies. *Ocean Dyn.*, 64(5): 667–688, 2014. 41

Enderlin E. M., Howat I. M., Jeong S., Noh M-J., van Angelen J. H. and van den Broeke M. R. An improved mass budget for the Greenland ice sheet. *Geophys. Res. Lett.*, 41: 866–872, 2014. 3, 12, 24

Enderlin E. and Hamilton G. Estimates of iceberg submarine melting from high–resolution digital elevation models: application to Sermilik Fjord, East Greenland. *Journal of Glaciology*, 60(224): 1084–1092, 2014. 13

Enfield D. B., Mestas–Nunez A. M. and Trimble P. J. The Atlantic multidecadal oscillation and its relationship to rainfall and river flows in the continental U.S. *Geophys. Res. Lett.*, 28: 2077–2080, 2001. 7

Farmer David M. and Freeland Howard J. The Physical Oceanography of Fjords. *Pros. Oceanog.*, 12: 147–220, 1983. 2

Fichefet T. and Morales Maqueda. Sensitivity of a global sea ice model to the treatment of ice thermodynamics and dynamics. *J. Geophys. Res.*, 102: 12609–12646, 1997. 32

Foga S., Stearns L. A. and Van der Veen C. J. Application of satellite remote sensing techniques to quantify terminus and ice mélange behavior at Helheim Glacier, East Greenland. *Mar. Technol. Soc. J.*, 48: 81–91, 2014. doi:10.4031/MTSJ.48.5.3. 23

Freiwald A., Fosså J. H., Grehan A., Koslow T. and Roberts J. M. Cold–water Coral Reefs. *UNEP–WCMC, Cambridge, UK.*, 2004. 7

Fretwell P. et al. Bedmap2: improved ice bed, surface and thickness datasets for Antarctica. *The Cryosphere*, 7: 375–393, 2013. 52

Gelderloos R., Katsman C. A. and Drijfhout S. S. Assessing the roles of three eddy types in restratifying the Labrador Sea after deep convection. *Journal of physical oceanography*, 41: 2102–2119, 2011. 4, 47

Gladish C. V., Holland D. M., Rosing–Asvid A., Behrens J. W. and Boje J. Oceanic boundary conditions for Jakobshavn Glacier. Part I: Variability and renewal of Ilulissat Icefjord waters, 2001–14. *J. Phys. Oceanogr.*, 45: 3–32, 2015 18, 22

Griffies S. M. Fundamentals of Ocean Climate Models. *Princeton University Press, Princeton, NJ*, p. 494, 2004 40

Hakkinen S. and Rhines P. B. Decline of subpolar North Atlantic circulation during the 1990s. *Science*, 304: 555–559, 2004. 6

Hakkinen S., Rhines P. B., Worthen D. L. Atmospheric blocking and Atlantic multidecadal ocean variability. *Science*, 334: 655–659, 2011. 6

Hakkinen S., Rhines P. B. and Worthen D. L. Northern North Atlantic sea surface height and ocean heat content variability. *J. Geophys. Res. Oceans*, 118: 3670–3678, 2013. 7

Hall D. K. et al. Variability in the surface temperature and melt extent of the Greenland ice sheet from MODIS. *Geophys. Res. Lett.*, 40, 2114–2120, 2013. 5

Hallberg R. Using a resolution function to regulate parameterizations of oceanic mesoscale eddy effects. *Ocean Modelling*, 72, 92–103, 2013.

Hanna E. et al. Greenland ice sheet surface mass balance 1870 to 2010 based on Twentieth century reanalysis, and links with global climate forcing. *J. Geophys. Res.*, 116, D24121, 2011. 3

Hanna E. et al. The influence of North Atlantic atmospheric and oceanic forcing effects on 1900-2010 Greenland summer climate and ice melt runoff. *Int. J. Climatol.*, 33: 862–880, 2013. 5

Harden B. E., Renfrew I. A. and Petersen G. N. A climatology of wintertime barrier winds off southeast Greenland. *J. Climate*, 24: 4701–4717, 2011. doi:10.1175/2011JCLI4113.1. 24

Harden B., Straneo F. and Sutherland D. Moored observations of synoptic and seasonal variability of the East Greenland Coastal Current. *Geophys. Res. Oceans*, 119: 8838-8857, 2014 doi: 10.1002/2014JC010134 23

Hátún H., Sandø A. B., Drange H., Hansen B. and Valdimarsson H. Influence of the Atlantic subpolar gyre on the thermohaline circulation. *J. Science*, 309: 1841–1844, 2005. 6

Holland D. M. and Jenkins A. Modeling thermodynamic ice-ocean interactions at the base of an ice shelf. *J. Phys. Oceanogr.*, 29: 1787–1780, 1999. 14

Holland D. M., Thomas R. H., de Young B., Ribergaard M. H. and Lyberth B. Acceleration of Jakobshavn Isbræ triggered by warm subsurface ocean waters. *Nature Geosci.*, 1: 659–664 , 2008. 6, 8

Holland P. R., Jenkins A. and Holland D. M. The Response of ice shelf basal melting to variations in ocean temperature. *J. Clim.*, 21: 2558–2572 , 2008. 20

Howat I. M., Joughin I. and Scambos T. A.. Rapid changes in ice discharge from Greenland outlet glaciers. *Science*, 315: 1559–1561, 2007. doi:10.1126/science.1138478. 3

Howat I. M., Box J. E., Ahn Y., Herrington A. and McFadden E. M. Seasonal variability in the dynamics of marine–terminating outlet glaciers in Greenland. *J. Glaciol.*, 56: 601–613, 2010. 25

Hurrell J. W. Decadal trends in the North Atlantic oscillation: regional temperatures and precipitation. *Science*, 269: 676–679, 1995.

Inall M. E. et al. Oceanic heat delivery via Kangerdlugssuaq Fjord to the south–east Greenland ice sheet. *J. Geophys. Res.*, 119: 631–645, 2014. 11, 18

IOC, IHO and BODC: Centenary Edition of the GEBCO Digital Atlas, published on CD-ROM on behalf of the Intergovernmental Oceanographic Commission and the International Hydrographic Organization as part of the General Bathymetric Chart of the Oceans. *British Oceanographic Data Centre, Liverpool, UK*, 2003. 52

Iovino D., Masina S., Storto A., Cipollone A. and Stepanov V. N. A 1/16° eddying simulation of the global NEMO sea–ice–ocean system. *Geosci. Model Dev.*, 9: 2665–2684, 2016. 32, 52

Iovino D., Ciliberti S., Cipollone A., Masina S., Coppini G., Lecci R., Montagna F., Trotta F. and Pinardi N. GOFS16: a Global Ocean Forecast System at eddying resolution. *Geophysical Research Abstracts, EGU General Assembly 2018.*, 20: EGU2018–18965, 2018. 32, 33, 39

Jackett D. R. and Mcdougall T. J. Minimal adjustment of hydrographic profiles to achieve static stability. *J. Atmos. Oceanic Technol.*, 12(2): 381–389, 2014. 35, 55, 97, 99

Jackson R. H., Straneo F. and Sutherland D. A. Externally forced fluctuations in ocean temperature at Greenland glaciers in non–summer months. *Nat. Geosci.*, 7: 503–508, 2014. 18, 20, 22, 24, 26, 27, 92, 101, 129

Jackson Rebecca H. and Straneo Fiammetta. Heat, Salt, and Freshwater Budgets for a Glacial Fjord in Greenland. *Journal of physical oceanography*, 46: 2735–2768, 2016. 11, 12, 13, 18, 19, 23, 24, 25, 26, 27, 28, 55, 59, 60, 62, 64, 66, 67, 88, 92, 94, 98, 106, 113, 117, 118, 123

Jackson Rebecca H., Lents Steven J. and Straneo Fiammetta. The Dynamics of Shelf Forcing in Greenlandic Fjords. *Journal of physical oceanography*, 48: 2799–2827, 2018. 23, 25, 27, 92, 101, 104, 113, 123, 125, 126

Jenkins A. Convection-driven melting near the grounding lines of ice shelves and tidewater glaciers. *Phys. Oceanogr.*, 41: 2279–2294, 2011. 11, 20

Jenkins A., Nicholls K. W., Corr H. F. J. Observation and parameterization of ablation at the base of Ronne Ice Shelf, Antarctica. *Phys. Oceanogr.*, 40: 2298–2312, 2010. 14

Johnson H. L., Munchow A., Falkner K. K. and Melling H. Ocean circulation and properties in Petermann Fjord, Greenland. *J. Geophys. Res.*, 116:C01003, 2011. 16, 22

Joughin I., Smith B. E., Shean D. E. and Floricioiu D. Brief communication: further summer speedup of Jakobshavn Isbræ. *Cryosphere*, 8: 209–214, 2014. 10

Jungclaus J. H., Haak H., Latif M. and Mikolajewicz U. Arctic-North Atlantic interactions and multidecadal variability of the meridional overturning circulation. *J. Climate*, 18: 4013–4031, 2005. 25

Kader B. A. and Yaglom A. M. Heat and mass transfer laws for fully turbulent wall flows. *Int. J. Heat Mass Transfer* , 15: 2329–2351, 1972. 15

Kara A. B., Wallcraft A. J. and Hurlburt H. A correction for land contamination of atmospheric variables near land–sea boundaries. *J. Phys. Oceanogr.*, 37(4): 803–818, 2007. 41

Katavouta A. and Thompson K. R. Downscaling ocean conditions with application to the Gulf of Maine, Scotian Shelf and adjacent deep ocean. *Ocean Modelling*, 104: 57–72, 2016. 38, 43

Richard K. Carbon cycle: Hoard of fjord carbon. *Nature Geoscience*, 8: 426–427, 2015. 7

Khan S. A., Wahr J., Bevis M., Velicogna I. and Kendrick E. Spread of ice mass loss into northwest Greenland observed by GRACE and GPS. *Geophys. Res. Lett.*, 37, L06501, 2010. 3

Klinck J. M., OBrien J. J., Svendsen H. A simple model of fjord and coastal circulation interaction. *J. Phys. Oceanogr.*, 11: 1612–1626, 1981. 18

Levitus S. et al. World ocean heat content and thermosteric sea level change (0-2000 m), 1955-2010. *Geophys. Res. Lett.*, 39, L10603, 2012. 6, 7

Li Lin and Bromwich D. H. Polar Meteorology Group, Byrd Polar Research Center The Ohio State University, Columbus, Ohio. Cyclone activity around the Greenland ice sheet for last 50 years.
Url: https://ams.confex.com/ams/pdfpapers/20479.pdf 129

Lohmann K., Drange H. and Bentsen M. A possible mechanism for the strong weakening of the North Atlantic subpolar gyre in the mid–1990s. *Geophys. Res. Lett.*, 36, L15602, 2009. 6

Madec and the NEMO team. NEMO ocean engine, version 3.6 – manual. *Note du Pole de modélisation de l'Institut Pierre–Simon Laplace No 27.*, ISSN N. 1288–1619, 2016. 33, 36, 39, 40

Manabe S. and Stouffer R. J. Sensitivity of a global climate model to an increase of CO2 concentration in the atmosphere. *J. Geophys. Res.*, 85: 5529–5554, 1980. 7

McWilliams J. C., Restrepo J. M. and Lane E. M. An asymptotic theory for the interaction of waves and currents in coastal waters. *J. Fluid Mech.*, 511: 135–178, 2004. 39

Mernild S. H. et al. Freshwater flux to Sermilik Fjord, SE Greenland. *Cryosphere*, 4: 453–465, 2010.

Morlighem M. et al. BedMachine v3: Complete bed topography and ocean bathymetry mapping of Greenland from multi–beam echo sounding combined with mass conservation. *Geophysical Research Letters*, 44: 2017.
Url: https://doi.org/10.1002/2017GL074954 52, 54

Morrow R. and Le Traon P. Y. Recent advances in observing mesoscale ocean dynamics with satellite altimetry. *Adv. Space Res.*, 50: 1062–1076, 2012. 32

Mortensen J., Lennert K., Bendtsen J. and Rysgaard S. Heat sources for glacial melt in a sub–Arctic fjord in contact with the Greenland Ice Sheet. *J. Geophys. Res.*, 116: C01013, 2011. 17

Mortensen J., Bendtsen J., Motyka R. J., Lennert K., Truffer M. et al. On the seasonal freshwater stratification in the proximity of fast–flowing tidewater outlet glaciers in a sub–Arctic sill fjord. *J. Geophys. Res.*, 118: 1382–1395, 2013.

Mortensen J., Bendtsen J., Lennert K. and Rysgaard S. Seasonal variability of the circulation system in a west Greenland tidewater outlet glacier fjord, Godthåbsfjord (64N). *J. Geophys. Res. Earth Surf.*, 119: 2591–2603, 2014. doi:10.1002/2014JF003267 18

Motyka R., Hunter L., Echelmeyer K. and Connor C. Submarine melting at the terminus of a temperate tidewater glacier, LeConte Glacier, Alaska, USA. *Ann. Glaciol.*, 36: 57–65, 2003. doi:10.3189/172756403781816374 26

Motyka R., Dryer W. P., Amundson J., Truffer M. and Fahnestock M. Rapid submarine melting driven by subglacial discharge, LeConte Glacier, Alaska. *Geophys. Res. Lett.*, 40: 5153–5158, 2013. doi:10.1002/grl.51011 26

Munchow A., Padman L. and Fricker H. A. Interannual changes of the floating ice shelf of Petermann Gletscher, North Greenland, from 2000 to 2012. *J. Glaciol.*, 60: 489–499, 2014. 10

Murton Julian B., Peterson R. and Ozouf J.–C. Bedrock Fracture by Ice Segregation in Cold Regions. *Science*, 314(5802): 1127–1129, 2006. 2

Myers P. G., Kulan N. and Ribergaard M. H. Irminger water variability in the west Greenland current. *Geophys. Res. Lett.*, 34, L17601, 2007. 6, 8

Myers P. G. and Ribergaard M. H. Warming of the Polar Water in Disko Bay and potential impact on Jakobshavn Isbrae. *Journal of physical oceanography*, http://dx.doi.org/10.1175/JPO–D–12–051.1, 2013. 6

National Centers for Environmental Prediction/National Weather Service/NOAA/U.S. Department of Commerce. NCEP GFS 0.25 Degree Global Forecast Grids Historical Archive. Research Data Archive at the National Center for Atmospheric Research, Computational and Information Systems Laboratory, 2015.
Url: https://doi.org/10.5065/D65D8PWK 33, 54

Nesje A. and Whillans I. M. Erosion of Sognefjord, Norway. *Geomorphology*, 9(1): 33–45, 1994. 2

Nycander J. and Doos K. Open boundary conditions for barotropic waves. *J.Geophys. Res.*, 108(C5): 3168–3187, 2003. 46

Nurser A. J. G. and Bacon S. The Rossby radius in the Arctic Ocean. *Ocean Sci.*, 10: 967–975, 2014. 32

Oddo P. and Pinardi N. Lateral open boundary conditions for nested limited area models: a scale selective approach. *Ocean Modelling*, 20: 134–156, 2008. 38, 43, 44

Oliger J. and Sundstrom A. Theoretical and practical aspects of some initial boundary value problems in fluid mechanics. *SIAM J. Appl. Math.*, 35: 419–446, 1978. 43

Oltmanns M., Straneo F., Moore G. W. K. and Mernild S. H. Strong downslope wind events in Ammassalik, Southeast Greenland. *Journal of Climate*, 27: 977–993, 2014. 24, 25

Pacanowski R. C. and Philander S. G. H. Parameterisation of vertical mixing in numerical models of tropical oceans. *J. Phys. Oceanogr.*, 11(11): 1443–1451, 1981. 35, 41

Palma E. D. and Matano R. P. On the implementation of passive open boundary conditions for a general circulation model: the barotropic mode. *J. Geophys. Res.*, 103: 1319–1341, 1998. 46

Pickart R. S., Spall M. A., Ribergaard M. H., Moore G. W. K. and Milliff R. F. Deep convection in the Irminger Sea forced by the Greenland tip jet. *Nature*, 424: 152–156, 2003. 25

Polyakov I. V. et al. Multidecadal variability of North Atlantic temperature and salinity during the twentieth century. *J. Clim.*, 18: 4562–4581, 2005. 7

Pritchard H. D., Arthern R. J., Vaughan D. G. and Edwards L. A. Extensive dynamic thinning on the margins of the Greenland and Antarctic ice sheets. *Nature*, 461: 971–975, 2009. 8

Rignot E., Koppes M. C. and Velicogna I. Rapid submarine melting of the calving faces of West Greenland glaciers. *Nat. Geosci.*, 3: 187–91, 2010. 8, 11, 26

Rignot E. and Kanagaratnam P. Changes in the velocity structure of the Greenland ice sheet. *Science*, 315: 1559–1561, 2006. 3

Roed L. P. and Cooper C. A study of various open boundary conditions for wind–forced barotropic numerical ocean models. *Three–dimensional models of marine and estuarine dynamics, edited by J. C. J. Nihoul and B. N. Jamart, Elsevier*, pp. 305–333, 1987 46

Schaffer J. et al. A global, high–resolution data set of ice sheet topography, cavity geometry, and ocean bathymetry. *Earth Syst. Sci. Data*, 8(2): 543–557, 2016. 54

Schjøth F. et al. Campaign to map the bathymetry of a major Greenland fjord. *EOS Trans. Am. Geophys. Union*, 93: 141–142, 2012. 18

Schlesinger M. E. and Ramanjutty N. An oscillation in the global climate system of period 65-70 years. *Nature*, 367: 723–726, 1994. 7

Sciascia R., Straneo F., Cenedese C. and Heimbach P. Seasonal variability of submarine melt rate and circulation in an East Greenland fjord. *J. Geophys. Res.*, 118: 2492–2506, 2013. 6, 11, 15, 20

Shepherd A., Ivins E. R., Geruo A., Barletta V. R., Bentley M. J. et al. A reconciled estimate of ice–sheet mass balance. *Science*, 338: 1183–1189, 2012. 3

Simoncelli S., Pinardi N., Oddo P., Mariano A. J., Montanari G., Rinaldi A. and Deserti M. Coastal rapid environmental assessment in the Northern Adriatic Sea. *Dyn. Atmos. Oceans*, 52(1–2): 250–283, 2011. 46

Simpson J. H. Physical processes in the ROFI regime. *Journal of Marine Systems*, 12: 3–15, 1997. 82

Smith R. D., Maltrud M. E., Bryan F. and Hecht M. W. Numerical simulation of the North Atlantic Ocean at 1/10°. *J.Phys. Oceanogr.*, 30: 1532–1561, 2000. 32

Smith R. W., Bianchi T. S., Allison M., Savage C. and Galy V. High rates of organic carbon burial in fjord sediments globally. *Nature Geoscience*, 8: 450–453, 2015. 8

Sole A., Payne T., Bamber J., Nienow P. and Krabill W. Testing hypotheses of the cause of peripheral thinning of the Greenland ice sheet: is land–

terminating ice thinning at anomalously high rates? *Cryosphere*, 2: 205–218, 2008. 3

Stigebrandt A. and Aure J. The importance of external driving forces for the water exchange in the fjords from Skagerrak to Finnmark. *Inst. Mar. Res., Bergen, Nor*, FO9003, 1990. 18, 20

Stigebrandt A. Hydrodynamic and circulations of fjords. *Encyclopedia of Lakes and Reservoirs, ed. L. Bengtsson, R. W. Herschy, R. W. Fairbridge, Dordrecht, Neth.: Springer*, pp. 327–344, 2012. 21

Storto A., Masina S. and Navarra A. Evaluation of the CMCC eddy–permitting global ocean physical reanalysis system (C–GLORS, 1982–2012) and its assimilation components. *Q. J. R. Meteorolog. Soc.*, 142 (695): 738–758, 2015. 32

Stouffer R. J. et al. Investigating the causes of the response of the thermohaline circulation to past and future climate changes. *J. Climate*, 19: 1365–1387, 2006. 25

Straneo F., Hamilton G. S., Sutherland D. A., Stearns L. A., Davidson F. et al. Rapid circulation of warm subtropical waters in a major glacial fjord in East Greenland. *Nat. Geosci.*, 3: 182–186, 2010. 8, 16, 20

Straneo F., Curry R. G., Sutherland D. A., Hamilton G. S., Cenedese C. et al. Impact of fjord dynamics and glacial runoff on the circulation near Helheim Glacier. *Nat. Geosci.*, 4: 322–327, 2011. 17, 23, 28

Straneo F. et al. Characteristics of ocean waters reaching Greenlands glaciers. *Ann. Glaciol.*, 53: 202–210, 2012. 8, 9, 11

Straneo Fiammetta and Heimbach Patrick. North Atlantic warming and the retreat of Greenlands outlet glaciers. *Nature*, 504: 36–43, 2013. 4, 5, 6, 7, 8, 9, 14, 23, 47

Straneo Fiamma and Cenedese Claudia. The Dynamics of Greenlands Glacial Fjords and Their Role in Climate. *Annu. Rev. Mar. Sci.*, 7: 89–112, 2015. 2, 4, 5, 10, 11, 12, 13, 14, 15, 16, 17, 18, 22, 23

Sutherland D. A. and Pickart R. S. The East Greenland Coastal Current: structure, variability, and forcing. *Prog. Oceanogr.*, 78: 58–77, 2008. 8, 9, 23

Sutherland D. A. and Straneo F. Estimating ocean heat transports and submarine melt rates in Sermilik Fjord,Greenland, using lowered acoustic Doppler

current profiler (LADCP) velocity profiles. *Ann. Glaciol.*, 53: 50–58, 2012. 11

Sutherland D. A. et al. Atlantic water variability on the SE Greenland continental shelf and its relationship to SST and bathymetry. *J. Geophys. Res.*, 118: 847–855, 2012. 18, 25

Sutherland D. A., Straneo F. and Pickart R. S. Characteristics and dynamics of two major Greenland glacial fjords. *J. Geophys. Res.*, 119: 3767–3791, 2014. 13, 16, 17, 18, 23, 25, 102

Svendsen H. Exchange processes above sill level between fjords and coastal water. *Fjord Oceanography, ed. H. J. Freeland, D. M. Farmer, C. D. Levings*, 355–362, 1980. 18

Ting M., Kushnir Y., Seager R. and Li C. Forced and Internal Twentieth–Century SST Trends in the North Atlantic. *Journal of Climate*, 22(6): 1469-1481, 2009. 7

Trotta F., Fenu E., Pinardi N., Bruciaferri D., Giacomelli L., Federico I. and Coppini G. A Structured and Unstructured grid Relocatable ocean platform for Forecasting (SURF). *Deep–Sea Research II*, 133: 54–75, 2016. 38, 39, 42, 46

Trotta F., Pinardi N., Fenu E., Grandi A. and Lyubartsev V. Multi–nest high–resolution model of submesoscale circulation features in the Gulf of Taranto. *Ocean Dynamics*, 67: 1609–1625, 2017. 38, 52

Umgiesser G., Melaku Canu D., Cucco A. and Solidoro C. A finite element model for the Venice Lagoon. Development, set up, calibration and validation. *J. Marine Syst.*, 51(51): 123–145, 2004. 39

U.S. Department of Commerce. 2-minute Gridded Global Relief Data (ETOPO2v2). *National Oceanic and Atmospheric Administration, National Geophysical Data center*, doi:10.7289/V5J1012Q, 2006. 52

Vage K. Circulation and convection in the Irminger Sea. Ph.D. dissertation, Massachusetts Institute of Technology/Woods Hole Oceanographic Institute, pp. 149 25

Vage K. The Irminger Gyre: Circulation, convection, and interannual variability. *Deep Sea Res. Part I*, 58: 590-614, 2011. 9

Van den Broeke M., Bamber J., Ettema J., Rignot E., Schrama E., et al.
Partitioning recent Greenland mass loss. *Science*, 326: 984-86, 2009. 3

Wallcraft A. J., Kara A. B. and Hurlburt H. E. Convergence of Laplacian
diffusion versus resolution of an ocean model. *Geophys. Res. Lett.*, 32, 2005.
doi:10.1029/2005GL022514 51, 52

Walter J. I., Jason E., Tulaczyk S., Brodsky E. E., Howat I. M., Yushin A.
H. N. and Brown A. Oceanic mechanical forcing of a marine–terminating
Greenland glacier. *Ann. Glaciol.*, 53: 181–192, 2012. 25

Wessel P. and Smith W. H. F. A global, self–consistent, hierarchical, high–
resolution shoreline database. *J. Geophys. Res.*, 101(B4): 8741–8743, 1996.
54

Williams R. G., Roussenov V., Smith D. and Lozier S. Decadal evolution of
ocean thermal anomalies in the North Atlantic: the effect of Ekman, over-
turning and horizontal transport. *J. Clim.*, http://dx.doi.org/10.1175/JCLI–
D–12–00234.1, 2013. 6

Woollings T. and Hoskins B. Simultaneous Atlantic-Pacific blocking and the
Northern annular mode. *Q. J. R. Meteorol. Soc.*, 134: 1635–1646, 2008. 6

Xu Y., Rignot E., Fenty I., Menemenlis D. and Flexas M. M. Subaqueous melt-
ing of Store Glacier, west Greenland from three–dimensional, high–resolution
numerical modeling and ocean observations. *Geophys. Res. Lett.*, 40: 4648–
4653, 2013. 11, 26

Yashayaev I. Hydrographic changes in the Labrador Sea. 1960–2005. *Prog.
Oceanogr.*, 73: 242–276, 2007. 5, 9

Figure representing fjord formation process, Wikimedia Commons, by Ulamm
[CC BY–SA 3.0]
`https://en.wikipedia.org/wiki/Fjord#/media/File:Fjord_genesis.`
`png` 3

ICESat and IceBridge/Annual Elevation of the Greenland Ice Sheet from 2003
through 2012. NASA's Goddard Space Flight Center Scientific Visualization
Studio.
Url: `http://svs.gsfc.nasa.gov/4022` 3, 4

Definition of vector invariant form of momentum equations,
Url: `http://mitgcm.org/pelican/online_documents/node60.html` 34

Definition of well-posedness of a problem, MIT OpenCourseWare, 18.336 Numerical Methods for Partial Differential Equations, 2009
Url: http://ocw.mit.edu 43

Acknowledgments

I would like to thank my advisor Prof. Nadia Pinardi for sharing her knowledge and guiding my work, but also for giving me advice on the choices that are there awaiting me and for the great patience needed to follow my contorted reasoning and to face my stubbornness. Thank you for being a guide and a model not only for my thesis but also on a work-life perspective.

I'm grateful to my co-advisor Francesco, for always promptly answering my numerous and insistent questions and for his invaluable help in solving all the technical issues and in getting me accustomed to new programming languages. Thank you to Prof. Fiamma Straneo for her precious hints and for sharing her unique view of the contents of this thesis. Without her work on advancing the knowledge of Greenland's fjords and, thus, without her articles, the entire thesis wouldn't have been possible.

I'd also like to thank Luca Giacomelli for his help in case of technical emergency and all the guys at SiNCEM laboratory for always making me feel part of a dynamic and harmonious group.

A huge thank you to my mother, always there to support and reassure me in the arduous moments, but also to congratulate me in the many more beautiful ones. A special thought to my boyfriend Ruggero, always able to encourage me and to infuse me with his strength and faith in the future. Your words are always the right ones, able to awaken me from my fearful over-thinking.

Thank you to my uncle Achille and my grandmother Teresa for their treasured and meaningful advice; to my father and to my friend Adina, for their willingness to listen when I needed.

I dedicate my thesis to my beloved grandmother Rosangela, who really gave value to my studies and my efforts. She was always very proud of me and she would have been especially in this day, as if this were her own degree. She has been one of the strongest reasons to carry on in the difficult moments. I am sure this would have been one of the best days of her life.